Universität Basel

Immobilization of polymeric nano-assemblies for antibacterial applications

INAUGURALDISSERTATION

Zur Erlangung der Würde
eines Doktors der Philosophie vorgelegt der
Philosophisch-Naturwissenschaftlichen
Fakultät der Universität Basel

von
Serena Rigo
aus Lausen, BL

2020

Genehmigt von der Philosophisch-Naturwissenschaftlichen Fakultät auf Antrag von

Prof. Dr. Cornelia G. Palivan (Universität Basel)
Dissertationsleiterin

Prof. Dr. Marcus Textor (ETH Zürich)
Korreferent

Basel, den 21. April 2020

Prof. Dr. Martin Spiess
Dekan

Abstract

With conventional antibiotic therapies being increasingly ineffective, bacterial infections with subsequent biofilm formation represent a global threat to human health and therefore, new strategies to fight bacteria colonization need to be found. Coimmobilization of functional, nanosized assemblies broadens the possibility to engineer dually functionalized active surfaces with a nanostructured texture. Surfaces decorated with different nanoassemblies, such as micelles, polymersomes, or nanoparticles are in high demand for various applications ranging from catalysis, biosensing up to antimicrobial surfaces. In this thesis, I present a combination of bio-orthogonal and catalyst-free strain-promoted azide-alkyne click (SPAAC) and thiol-ene reactions to simultaneously coimmobilize various nanoassemblies; polymersome-polymersome and polymersome-micelle assemblies were selected. For the first time, the immobilization method using SPAAC reaction was studied in detail to attach soft, polymeric assemblies on a solid support. Together, the SPAAC and thiol-ene reactions successfully coimmobilized two unique self-assembled structures on the surfaces. Additionally, poly-(dimethylsiloxane) (PDMS)-based polymersomes were used as "ink" for direct immobilization from a PDMS-based microstamp onto a surface creating locally defined patterns. Furthermore, an active and a passive strategy based on polymeric micelles were combined to fight bacterial growth. The passive strategy involved covalent immobilization of polymeric micelles through Michael addition between maleimide exposed micelles and thiol functionalized surfaces. Compared to the bare surface, micelle-decorated surfaces showed reduced adherence and survival of bacteria. To extend this passive defense against bacteria with an active strategy, the immobilized micelles were equipped with the antimicrobial peptide KYE28 (KYEITTIHNLFRKLTHRLFRRNFGYTLR). The peptide interacted nonspecifically with the immobilized micelles where it retained its antimicrobial property. The successful surface decoration with KYE28 was demonstrated by a combination of X-ray photoelectron spectroscopy and quartz crystal microbalance with dissipation monitoring. The initial antimicrobial activity of the nanostructured surfaces against *Escherichia coli (E. coli)* was found to be increased by the presence of KYE28.

Combining immobilization reactions has the advantage to attach any kind of nanoassembly pairs, resulting in surfaces with "desired" interfacial properties. Different nanoassemblies that encapsulate multiple active compounds coimmobilized on a surface will pave the way for the development of multifunctional surfaces with controlled properties and efficiency. Additionally, the combination of our active and a passive strategy represents a straightforward modular approach that can easily be adapted, for example, by exchanging the antimicrobial peptide to optimize potency against challenging bacterial strains, and/or to simultaneously achieve antimicrobial and anti-infection properties.

Contents

Chapter 1

Introduction

This chapter is tightly based on the following review articles and book chapter I participated in writing: 'Nanoscience-Based Strategies to Engineer Antimicrobial Surfaces',[1] 'Enzymatic reactions in polymeric compartments: nanotechnology meets nature',[2] and 'Battling bacteria with free and surface-immobilized polymeric nanostructures'.[3]

1.1 Device associated infections

Bacteria play an important role in our health. The microbes of the skin are fundamental to skin physiology and prevent pathogens from entering the body.[4,5] Another well-known example is the 500–1,000 unique bacterial strains in the human colon.[6] This personal community of bacterial strains is referred to as the gut microbiota and is vital for many aspects of health, including physiology,[7] resistance to disease and digestion,[8] among others. In addition, there is a tight link between the human gut microbiota and the host central nervous system. The microbiome or genetic content of these bacteria changes in individuals with disease, such as irritable bowel syndrome,[7] obesity or diabetes[8] when compared to unaffected individuals. Advances in sequencing technology enabled the exploration of the role of the gut microbiota in a broad range of neurological and psychiatric disorders and diseases including Alzheimer's disease[9] and depression.[10] In addition, evidence to a causal role for the microbiota in disease acquisition is increasing.

Besides probiotics, there are numerous pathogenic bacteria which, when they proliferate uncontrolled in or on our body, cause a lot of distress, harm and in the worst case death. With the discovery of the first antibiotics, some of these deadly infections could finally be treated.[11] Following their inital discovery, numerous different classes of antibiotics were developed with different mechanisms of action. However, the antibiotic era was soon marred by the emergence of antibiotic-resistance. The world health organisation (WHO) in 2018 has highlighted antibiotic resistance as a serious global problem concerning everyone.[12] Besides improving the discovery models for new antimicrobial agents that are successful in the combat of antibiotic resistance, the need for developing new strategies such as the design of more effective preventive measures is urgent.

In today's life, medical devices play an important role in extending and/or improving life quality. Bone fractures can be repaired using metal screws, pins, and plates, hip and knee joints can be replaced, pacemakers can control the heartbeat, implants help reconstructing breasts after mastectomy, and different catheters are used in diagnosis

and treatment. Despite all medical progress, there is always the risk of infection following surgery. Pathogenic bacteria may spread within the body and proliferate on the implanted device, possibly leading to device associated infections (DAI) which account for a quarter of all health care associated infections in the USA.[13] Of particular concern is the threat of bacterial biofilm development, since these infections are difficult to diagnose and effective treatments are lacking.[14] Moreover, biofilm formation not only occurs on the implant, but also affects adjacent soft tissues and bone.[15] In order to keep the infection risk during surgery on an absolut minimum, preventive antibacterial treatment is essential to reduce possible bacteria contamination in the wound.[16] With the dramatic increase in the emergence of antibiotic resistant bacterial strains, there is an urgent need for more efficient antibiotic treatments to reduce DAI. Antimicrobial surfaces which actively or passively prevent bacteria colonialization by reducing the bacteria's ability to adhere and grow into a biofilm on implants, is an important research field in the fight against DAI.[1]

1.1.1 Biofilm

Bacterial species can cause DAI if they colonize on the device and grow into biofilms.[13] Biofilm formation is a dynamic and multifaceted process where cell to cell communication between the bacteria within the biofilm allow products essential for its development and survival to be actively shared and exchanged.[17–21] It is referred to as quorum sensing and relies on autoinducers, extracellular signalling molecules produced and detected by the bacteria.[22] Communication through electrical signals between bacteria is also possible.[23] The microorganisms within a biofilm are embedded into and protected by the biofilm matrix, which usually accounts for more than 90% of the dry mass of a biofilm.[24] The matrix consists of self-produced extracellular polymeric substances (EPS) which contain polysaccharides, proteins, glycoproteins, and other natural polymers.[25,26] The EPS of the matrix create a microenvironment with local heterogeneity. To protect the bacteria from dessication the matrix contains a lot of water due to which biofilms become slimy and are therefore often referred to as slime. Nevertheless, the mechanical stability is important and mostly provided by polysaccharides embedded in the matrix.[23,24]

Biofilms develop in many different environments and on many different surfaces always following the same sequence of events (**Figure 1.1**). On a surface in aqueous solution where organic molecules are present (e.g. seawater, blood, or urine) a conditioning film will form immediately by the adsorption of proteins and other organic molecules. First planktonic bacteria adhere reversibly to the surface and eventually attach irreversibly becoming sessile bacteria. These bacteria then start to divide and grow into microcolonies on the surface, where they produce EPS for the extracellular matrix, which anchors them further to the surface. The biofilm grows by cell division and by further attracting still freely suspended planktonic bacteria. Single bacteria can disperse actively and change back to a planktonic lifestyle when they decide that living within the biofilm community is no more beneficial for them (e.g. upon environmental changes). Bacteria aggregates can also detach passively by shear stress or mechanical forces.[25,27–29]

Treating DAI is not simple since the bacteria in a biofilm are not easily accessable, and the efficacy of antibiotic treatments is low due to their higher resistance to antibiotics compared to the same planktonic bacteria. Deep within the biofilm, so called dormant variants or persister cells, are living. These bacteria are not growing and antibiotics are ineffective as most antibiotics are only effective against growing bacteria. Therefore, such

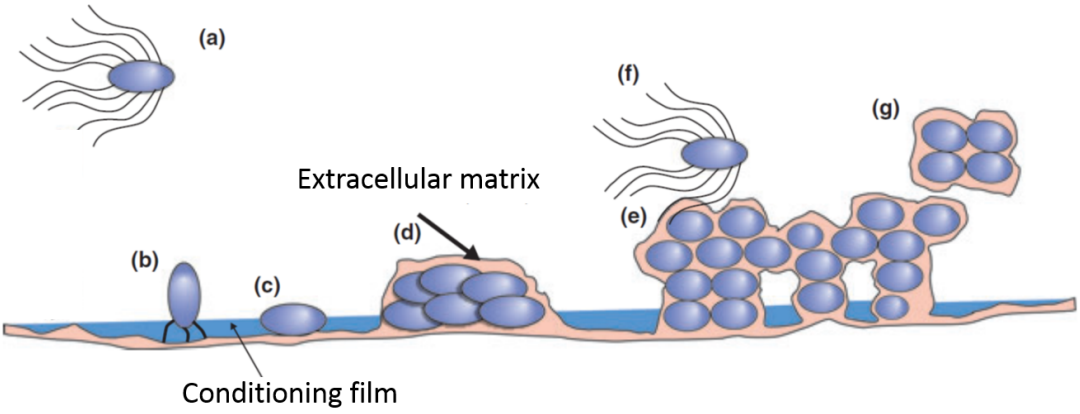

Figure 1.1: Schematic representation of biofilm formation. a) free swimming planktonic bacteria. b) reversible and c) irriversible attachment to the surface. d) microcolony with extracellular matrix formation. e) mature three dimensional biofilm. Detachment of f) single bacteria and g) bacteria aggregates.[27]

persister cells are able to survive antibiotic treatment and cause further relapse infections possibly leading to chronic infections.[13,23,30,31] The minimal biofilm eradication concentration (MBEC) is significantly higher than the minimal inhibition concentration (MIC) of the planktonic counterpart. Up to 1000 times the concentration of antibiotics has to be used to kill biofilm forming bacteria than planktonic ones.[17,31,32] Therefore, conventional treatments of DAI with antibiotics have several limitations, such as support of biofilm formation when the concentration of the antibiotic is lower than the MIC,[33,34] or ineffective treatment against non-multidrug resistant bacteria strains.[21] An effective way to prevent DAI would be the prevention of biofilm formation, hence the bacterial attachment to the surface as a first step of biofilm formation.

1.1.2 Bacteria attachment

Surface roughness and micro structures play an important role in deterring bacterial attachment. By directly mimicking the topography of biointerfaces and exploring the factors that are responsible for the antibiofouling properties, researchers have been guided towards the necessity to find relationships between surface microstructure and bacteria colonization.[35–38] Improving the understanding of the interactions between bacteria and micro-/nanostructures will help the development of more effective antibacterial surface designs. Several mechanisms, such as the contact area reduction (attachment point theory),[39] showing that species with few attachment points to a surface envisage reduced adhesion forces compared to species with enlarged contact area to the surface,[39,40] has been proposed as being responsible for controlling interactions between bacteria and hosts. In order to gain a better understanding, the physical properties of microstructured surfaces have been further divided into sub-groups, such as size, shape, spacing distance, or organization of the microstructures,[41] and different levels of interactions between surface patterns and bacteria have been identified. A surface possesses a universal bactericidal effect when patterns are smaller than the bacteria, probably because of mechanical deformation stresses leading to the rupture of the bacteria on the structured surface.[40] When surface patterns and cell size are similar, attachment of individual bacteria is hampered by

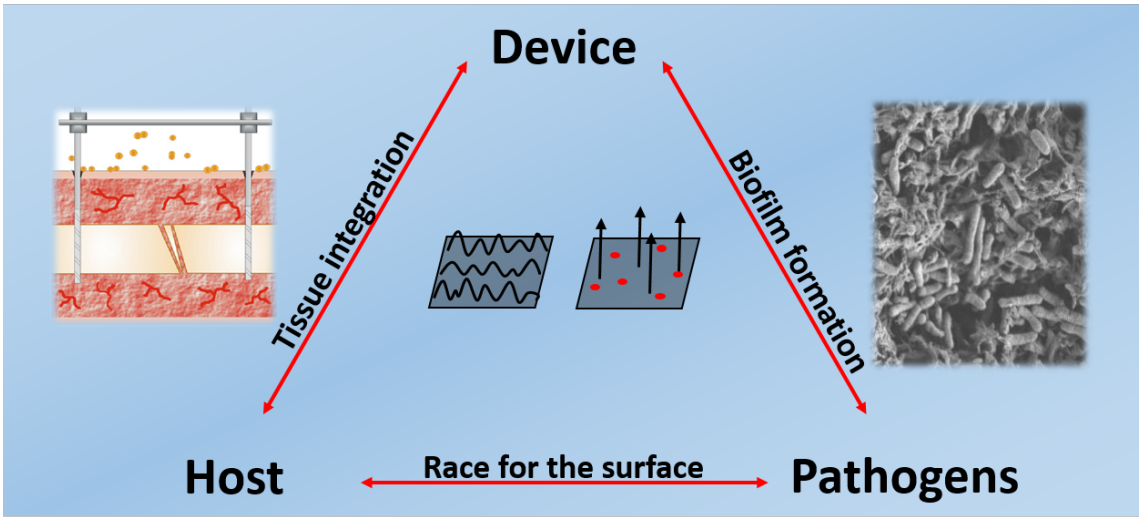

Figure 1.2: Interactions between device,[14] host, and pathogens[44] are the deciding factors for successful insertion of the device. Tissue integration should be promoted while preventing biofilm formation.[1]

the limited number of attachment points. However, it is inappropriate to attempt to identify a single physical factor that determines the effect of surface topography on bacterial attachment,[41] because other factors, such as surface chemistry, charge state,[42] and wettability, as well as the individual morphology of the bacteria[40] influence bacteria-surface interactions. Such complications might also be the explanation for some of the controversial conclusions that have been published. Therefore, all of these ideas and findings must be taken into consideration in order to create novel surfaces that combat bacterial growth.

1.1.3 Race for the surface

Interactions between the device, the host, and the bacteria are important for successful implantation and implant survival (**Figure 1.2**). They influence the ease with which an implant integrates into the biological environment of the host's body and the ability to prevent bacterial growth. To this end, there are various parameters that need to be considered; i) the surface and material properties of the device, ii) the type of pathogen, and iii) the strength of the host's immune system, which is decreased around synthetic material due to frustrated phagocytosis.[43] These interactions are critical factors in choosing the appropriate device-surface for a specific treatment. Competition between bacteria and cells for the implant surface is crucial, and the risk of DAI decreases dramatically as soon as the implant is completely colonized by the host's cells, since then there is no free surface remaining for the attachment and proliferation of bacteria.

Studies to test viability and metabolism of host cells separately from the capability of bacteria to form biofilms on implant surfaces represent a good first step for predicting weather host cells or bacteria will be able to first colonize the implant surface. To this end, silver-releasing hydroxyapatite coatings with fibronectin on titanium alloy (Ti-6Al-4V) surfaces have shown a high bacteria killing property likely due to the silver. On the other hand this surface was nontoxic to host cells probably assisted by the fibronectin.

These two separate findings indicate that the tested fibroblasts could win the race for the surface over *Staphylococcus aureus (S. aureus).*[19] However, biofilms were able to grow on surfaces of titanium, titanium-zirconium alloy, and zirconium-oxides with comparable roughness/smoothness,[45] and although the roughness or hydrophobicity did not have a decisive influence, the lowest biofilm formation was observed on the roughest titanium surface. To better understand this effect, co-culture studies are needed to reliably predict the chances of host cells winning the race for the surface. Such studies with human-gingival-fibroblasts (HGF) revealed that bacteria decreased the amount of HGF cells on all, but the smooth titanium surface, which supported the best soft tissue integration.[45] However, other works observed no significant differences between rough and smooth surfaces for implant survival,[46] and even significantly higher survival rates for rough surfaces.[47] A co-culture study compared the antimicrobial behavior of untreated titanium surface (Un-Ti) with sulfuric acid treated surface (SA-Ti) leading to a higher surface roughness, and sulfuric acid treated titanium surfaces with immobilized chitosan (SA-CS-Ti), whereas chitosan is known to decrease bacteria attachment. SA-CS-Ti surfaces showed the lowest bacteria adhesion both after 30 min and 4 hours (when *S. aureus* were incubated together with osteoblasts). This could be a consequence of the increased roughness due to the sulfuric acid treatment enhancing the attachment of cells and bacteria, while chitosan only minimized bacterial attachment, or at least minimized bacteria attachment stronger than osteoblast attachment. However, from 30 min to 4 h the amount of osteoblasts only increased on Un-Ti surfaces.[48] Such co-culture studies[49,50] provide important data for predicting the chances of successful osseo- or soft tissue integration. The combination of surface treatment and release of bactericidal agents seems to be the most promising strategy to prevent DAI, although studies over longer periods of time are still needed.

1.2 Antimicrobials

Antimicrobials are substances that act against microbes (e.g. bacteria, fungi, virus, parasite) either by killing them or stopping their growth. Antibiotics are active against bacteria, fungicide against fungi, antiviral drugs against virus, and antiparasitics against parasites. However, a drug of one of these classes of drugs is not active against the whole class of the specific microbes. Cephalexin, an antibiotic for instance, is not active against all bacteria.

1.2.1 Different classes of antibiotics

Bacteria can be divided into two groups regarding their cell wall composition. The cell wall of both groups is composed of an inner, cytoplasmic membrane containing proteins followed by a peptidoglycan layer, which is thick for the gram-postive bacteria and thin for the gram-negative ones. Additionally, the gram-negative bacteria possess an outer membrane. Gram-negative and gram-positive bacteria can be distinguished by the gram test from which they obtained the name. The gram positive bacteria retain the violet dye in the thick peptidoglycan layer and are stained violet. The gram negative bacteria do not retain the dye and get stained pink by the counter dye (**Figure 1.3**).

This difference in cell type affects the way that antibiotics effect the bacteria. Gram negative bacteria with the outer membrane, providing them further protection, are more resistant to antibodies and antibiotics than Gram positive bacteria which are lacking the

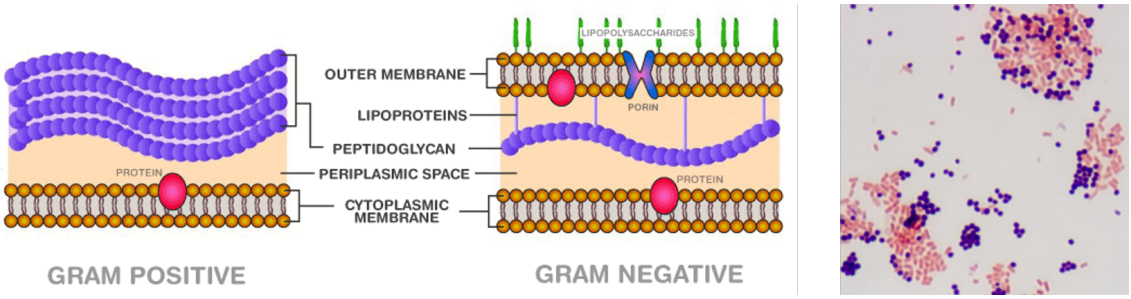

Figure 1.3: Schematic representation of gram-negative and gram-positive cell walls. Gram positive bacteria are stained purple while gram-negative ones pink by the gram test.[51,52]

outer membrane. Antibiotics act by either killing bacteria (bactericidal antibiotics), or by preventing bacteria from growing and reproducing (bacteriostatic antibiotics). To achieve the best treatment outcome, it is important to know the bacteria causing the infection in order to choose a suitable antibiotic out of the vast numbers of antibiotics on the market.

Penicillin, discovered by Alexander Fleming in 1928, started the antibiotic era. It is a β-lactam antibiotic and contains a β-lactam ring like all β-lactam antibiotics. Cephalosporins such as cephalexin, belong to them as well. β-lactam antibiotics are bactericidal and inhibit cell wall biosynthesis, precisely the formation of the peptidoglycan layer, which is important in bacteria, especially in gram-positive bacteria being the outermost layer of the membrane. Bacteria can develop resistances by producing enzymes (e.g. β-lactamase) which break down the β-lactam ring.

Tetracyclines, first discovered in the mid 1940's, contain four six-membared rings fused linearly together and are broad– spectrum antibiotics active against several gram-negative and gram-positve bacteria. However, they are used less due to increasing resistance. They are bacteriostatic and inhibit the biosynthesis of proteins on bacterial ribosome.

Another bacteriostatic antibiotic discovered the same time as tetracyclines is Chloramphenicol. It inhibits bacterial growth and protein synthesis by preventing protein chain elongation. It is a braod-spectrum antibioitc but only used in cases where infections are life-threatening due to the possibility of serious toxic effects. In developing countries however, it is a much more common antibiotic due to its low cost and high availability.

Quinolones are broad-spectrum antibiotics widely used in hospital acquired infections where resistance to older classes of antibiotics is suspected. Quinolone antibiotics were introduced in the 1960s and have a core structure related to 4-quinolone with an attached carboxylic acid group. Many contain a fluorine atome due to which they are then referred to as fluoroquinolones. They are bactericidal and interfere with the deoxyribonucleic acid (DNA) replication and transcription. Unfortunately, resistances to quinolones can be particularly rapid in its development.

Lipopeptides were discovered in the late 1980s. This class of antibiotics contains a lipid bonded to a peptide. They are bactericidal and disrupt several aspects of the cell membrane function. This seems to be advantageous as resistance to these antibiotics are rare, although have been reported.

Several metals such as selenium,[53] zinc,[54,55] Gallium,[54] copper[55] or silver[55] are used in antimicrobial treatment strategies due to the intrinsic antimicrobial properties of the elements. These elements are applied in the form of salts, nanoparticles (NPs) or ions to fight and prevent antimicrobial infections. The use of silver ions in their most common oxidation state (Ag^+) is the predominant inorganic approach that has been developed.[20,56,57] AgNPs offer the advantage of reducing possible precipitation and therefore inactivation of free silver ions,[58] as well as inhibiting the toxic effect of free silver ions by storing them in the zero oxidation state (Ag^0).[20] It was demonstrated that AgNPs have slower *in vitro* antimicrobial activity (at the same total silver concentration) than free silver ions, because of the release kinetics of Ag^+ from the AgNPs.[59]

Gramicidins were the first antimicrobial peptides (AMPs) discovered in 1939 and later also commercially used as antibiotics. However, it lasted until the 1980s, with the descriptions of cecropins and magainins, for the research of AMPs to get popular. Since then a vast amount of new AMPs were discovered and characterized.[60] They are ubiquitous in multicellular organisms from plants, bacteria, insects, amphibians, birds, and mammalians.[60,61] AMPs exhibit excellent biocompatibility and are less prone to create resistance in bacteria due to their mechanism of attacking the cell membrane rather than specific targets.[62] They selectively rupture bacteria but not mammalian cells. No cytotoxicity was observed in mammalian cells for the release of short cationic AMPs when covalently attached,[63] embedded in polysaccharide films,[64] or physically adsorbed on titanium-oxide nanotubes.[65] Various modes of actions for AMPs were proposed, mostly aiming the bacterial plasma membrane in which pores are formed, the membrane is thinned, or completely lysed and assembled into micelles. The peptide membrane interactions are typically driven by electrostatic forces.[66,67] Some peptides also penetrate into the bacteria manipulating intracellular targets like inhibiting the synthesis of proteins, DNA, or ribonucleic acid (RNA).[66] With these characteristics, AMPs are a promising alternative to conventional antibiotics, because they possess broad antibiotic effects, but supposedly induce less resistance than conventional antibiotics.[62,68]

1.2.2 Resistance: strategies needed

Bacteria have developed many different resistance strategies to survive in antibiotic settings. The great genetic flexibility allows bacteria to adapt quickly and survive in changing environments. Genes are not only classically transferred from one bacteria generation to the next one but also horizontally, meaning from one bacteria to an already living one from the same or a different species. Genes responsible for certain resistance mechanisms can through this horizontal gene transfer spread quickly to different bacteria and environments globally.[69] Resistance against certain antibiotics were already identified shortly after the discovery or introduction to clinical use of the antibiotic itself. Resistance genes (R-genes) are also found in people living far from the modern civilisation without contact to antibiotics. R-genes are up to 600 million years old. Many Bacteria are producing antibiotic compounds them self. These bacteria developed resistance strategies to protect themselves from their own produced antibiotic. Resistance is inevitable but spread dramatically since the introduction of antibiotics to the market during the last century. The selection of resistant bacteria strains was accelerated due to the overload of antibiotics in the environment as a consequence of the over- and misuse of the antibiotics in the society. The production of antibiotics is cheap. Less than half of the antibiotics produced are used

for therapeutic applications in humans.[70] However, the same antibiotics are also used in animal breeding and in agriculture to optimize health and growth of animals and crops, leading to a high abundance of antibiotics in the environment. Therefore, the ecological equilibrium between antibiotic susceptible and resistant stains shifted towards resistant bacteria strains.[69] To slow down the emergence of new resistances or the spread of already established resistance mechanisms, it is important to regulate the use of antibiotics and only apply an appropriate one when needed against species susceptible to that specific antibiotic applied. The design and development of niche antibiotics instead of broad spectrum antibiotics is promising in the race between antibiotics and their resistance occurring.[71]

1.3 Synthetic assemblies

1.3.1 Amphiphilic block-copolymers

Amphiphilic molecules are composed of both hydrophilic and hydrophobic parts. A prominent example in nature are lipids with a hydrophilic head group and a hydrophobic tail which together with membrane proteins, make up the membrane boundary of natural vesicles which store, transport, produce, or protect molecules such as enzymes by generating compartmentalized reaction spaces. A large variety of biological vesicles with different functions exists such as extracellular vesicles for long and short distance communication between celles,[72,73] endosomes that encapsulate extracellular material and cell surface proteins and thereby transport them within the cell for recycling or degradation,[74] or lysosomes that enclose many degradative enzymes.[75]

The high specificity and complexity of biological membranes limits their industrial and technological application. Therefore, natural or synthetic lipids are used to design more simple systems that mimic biological membranes.[76] Due to their amphiphilic character, lipids are able to self-assemble into various structures, such as micelles or vesicles (liposomes) that are often applied as delivery systems in the cosmetic and pharmaceutical industries.[77,78] However, one major drawback of liposomes and other lipid-based structures is their instability in the body. Functionalizing lipids with polymers, for example by PEGylation[79] was found to improve liposome stability and stealthiness, meaning avoiding major biological reaction or interactions that would lead to degradation and removal of the structure from the blood. This prompted the development of membrane mimics composed purely of amphiphilic polymers[80,81] that contain at least one hydrophilic and one hydrophobic block. Depending on how many blocks are used, these amphiphilic polymers are referred to as di- or tri block copolymers; AB or ABA, respectively, with A being the hydrophilic and B the hydrophobic block.[82,83] Triblock copolymers with different hydrophilic blocks A and C on either side of the hydrophobic block B are designed to create asymmetric membranes with different properties.[84–86] Like lipids, amphiphilic polymers can self-assemble into structures allowing mimicking biological compartmentalization strategies;[2] however, block copolymers are much more versatile than lipids because they can be composed of a wide range of building blocks synthesized from chemically distinct monomers, and lend themselves to chemical modifications. In addition to the possibility of functionalization, which allows for tuning the surface properties, polymer-based nanocarriers are usually more stable than lipid-based systems.[83,87–91] These features are particularly

important for *in vivo* applications because they help to prolong circulation time in the body.[92] The robust polymer membrane also protects the cargo from adverse effects from the environment as exemplified by a poorly soluble and unstable antimalarial compound, which in a polymer formulation showed increased solubility while retaining activity.[93]

Amphiphilic bock-copolymers with specific molecular weight and dispersity (Đ) can be synthesized by different approaches such as (1) reversible addition–fragmentation chain transfer (RAFT) polymerization, (2) atom transfer radical polymerization (ATRP), (3) anionic living polymerization, or (4) ring-opening polymerizations (ROPs), each one having its own advantages and disadvantages also regarding their further application. In living polymerization, the reaction stops once the monomer in solution has been consumed and restarts upon addition of fresh monomer. Because it offers precision and control over molar mass and end-groups, living polymerization is a popular method for synthesizing a variety of distinct block copolymers (ABA, ABC, ABCA, etc.).[94]

(1) RAFT polymerization is a versatile polymerization technique where many different vinyl monomers and different solvents including water can be used and reaction conditions are moderate. Besides, it is effective for the synthesis of block and hyperbranched copolymers. For example, thermoresponsive poly[(glycerol monomethacrylate-*stat*-glycidylmethacrylate)]-*block*-poly(2-hydroxypropyl methacrylate) block copolymers were synthesized via RAFT.[95] It is a controlled polymerization, however, re-initiation is required once monomer is completely consumed. One major advantage of RAFT polymerization is its tolerance of functionality including introduced substituents that can be used in 'click' reactions.[96,97]

(2) ATRP is another method that can be applied to synthesize polymers from a wide selection of vinyl monomers. For example, the positively charged, photosensitive poly(2-dimethylaminoethyl methacrylate) (PDMAEMA) was synthesized by ATRP. Under UV irradiation, PDMAEMA changes to its neutral form, which as a constituent of a self-assembled nanocompartment enables the slow release of a compound from the compartment.[98] However, ATRP typically requires a transition metal catalyst, albeit metal-free catalyst are emerging.[99,100] The possible toxicity associated with the metal catalyst and its ligands makes careful purification necessary and limits the potential of polymers synthesized via ATRP in biomedical applications.[97]

(3) In anionic living polymerization, the variety of possible vinyl monomers for polymer synthesis is reduced as the negative charge needs to be stabilized and delocalized with the help of stabilizing substituents.

(4) ROP are other living polymerization techniques[94] with which biodegradable polymers can be synthesized.[97,101] ROPs are sensitive to impurities including water and oxygen. As the name suggests, cyclic monomers are used and react with the reactive polymer end by opening its ring system and turning itself into the reactive end. Depending on the nature of the propagation center they are referred to as radical-, anionic-, or cationic ROP. Anionic ROP can be used for the synthesis of polyesters, polyamides like nylon 6, polycarbonates, polyurethanes, and polyphosphates in a controlled fashion. Also polydimethylsiloxane (PDMS), which is the hydrophobic block of the block copolymer used for the research described in this thesis, can be synthesised by anionic ROP.[102,103] PDMS is biocompat-

ible and widely used in biomedical applications such as breast implants, contact lenses or pacemakers.[104] Cationic ROP is one of the techniques used for the synthesis of polyoxazolines like the poly(2-methyl-2-oxazoline) (PMOXA),[82,105] which is the hydrophilic block of the block copolymer used for the research described in this thesis. PMOXA is a biocompatible and bioinert polymer, which decreases blood clotting, protein adsorption, and bacteria colonization.[104,106] Furthermore, PMOXA is a peptidomimetic but is known to be more stable towards degradation.[106,107]

The polymerization techniques mentioned above result in a statistical distribution of different chain lengths. This variation is described by the dispersity Đ (**Equation 1.1**), defined by the ratio between the weight average molecular weight (M_w) (representing the molecular weight above and below which there is an equal mass of polymer chains) and the number average molecular weight (M_n) (representing the molecular weight above and below which there is an equal number of polymer chains) for the polymer. A narrow mass distribution of the polymer gives a low Đ, which is always greater than one because M_w is always bigger than M_n, as M_n is more sensitive to lower mass molecules. Thus, if all polymers have the same mass, Đ would equal 1.[99,108]

$$Đ = \frac{\bar{M}_w}{\bar{M}_n} \tag{1.1}$$

1.3.2 Polymer self-assembly

Amphiphilic block copolymers can self-assemble in aqueous diluted solution into various nano- or micrometer sized structures such as spherical micelles, cylindrical micelles, tubes, lamellar structures, or vesicles (polymersomes) (**Figure 1.4**).[83] There are different procedures to form such self-assembled structures: In the cosolvent,[86] solvent switch,[109] and the water addition/solvent evaporation[86] procedure, the amphiphilic block copolymer is dissolved in an organic solvent. During the solvent switch and water addition/solvent evaporation procedure the ultimately desired solvent system in which only the hydrophilic block is soluble, i.e., an aqueous buffer, is added to the polymer solution. Alternatively, the polymer solution is added dropwise to the aqueous solvent during the cosolvent method. Monodispersed vesicles mostly in the micrometer range with high encapsulation efficiencies can be obtained by double emulsions using microfluidics. Water droplets are kept within an oil layer surrounded by water. In this technique, the organic solvents together with the high complexity of the set up, are the main disadvantages. The evaporation of the organic solvent after vesicle formation is not yet efficient.[110,111] One disadvantage of all these mentioned methods is that traces of organic solvent might remain in the system which might be toxic for downstream applications. This is not the case in the film rehydration method,[86,112] where the polymer dissolved in the organic solvent is first completely dried to a thin film, whose subsequent rehydration with aqueous buffer results in self-assembly without residual organic solvents. A very similar method is the solid rehydration, where the polymer is directly rehydrated from a bulk powder instead of a thin film.[113]

The type of polymer, the solvent(s), and the method applied for self-assembly affect what structure will be obtained. The nature of the polymer, its molecular weight (Mw), its hydrophilic fraction f (**Equation 1.2**), and the packing parameter P (**Equation 1.3**) are crucial parameters that determine the structures resulting from self-assembly (**Figure 1.4**).

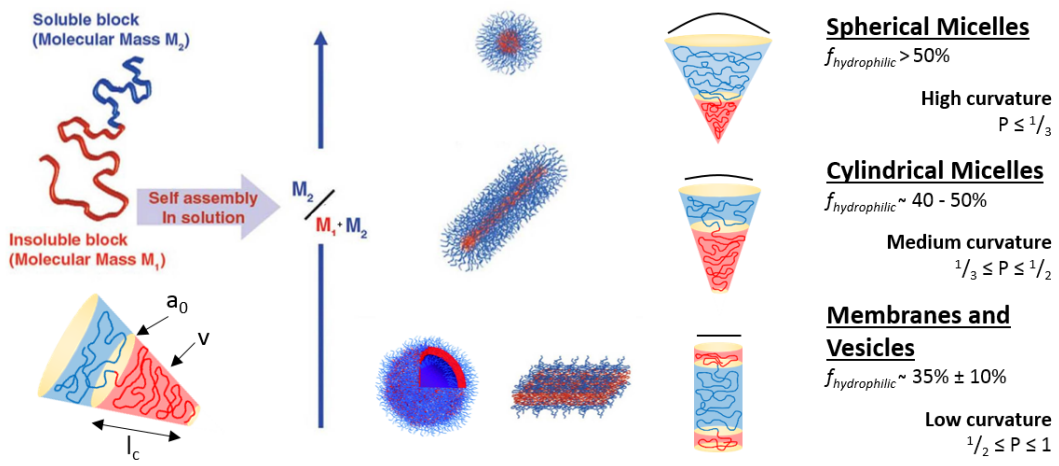

Figure 1.4: Different structures self-assemble from amphiphilic block cpoppolymers in dilute solutions. The hydrophilic fraction (soluble fraction) of amphiphilic block copolymers and their packing parameter influence the outcome of the self-assembly. [114, 115]

$$f_{hydrophylic}[\%] = \frac{M_{w\ hydrophilic}}{M_{w\ hydrophobic}} * 100 \tag{1.2}$$

$$P = \frac{v}{a_0 l_c} \tag{1.3}$$

v describes the volume occupied by the hydrophobic, water insoluble block, and l_c its length. a_0 is the optimum area between the volumes occupied by the soluble and insoluble blocks. All these parameters (v, l_c, and a_0) are defined in an equilibrated state where the interactions between the two blocks are balanced. The curvature which arises due to the relative size ratio of the two blocks is reflected in P, and is an important determinant for the ensuing structure.

Self-assembly is based on intramolecular and intermolecular interactions, mostly driven by non-covalent hydrophobic interactions. In order to initiate self-assembly, the dilute polymer concentration in solution needs to exceed the critical micelle concentration (CMC). In aqueous media, the hydrophobic blocks tend to align and are protected by the hydrophilic blocks, in order to minimize the total free energy. To obtain polymersomes, the hydrophilic, water-soluble, fraction of the block copolymer should be around 35% and $1/2 \leq P \leq 1$. Polymers with hydrophilic fraction of 40 – 50% and $1/3 \leq P \leq 1/2$ tend to self-assemble into rod-like aggregates. Theoretically, the most stable condition for self-assembled structures would be infinitely long cylinders and infinitely large membranes. However, in order to avoid contact between the insoluble fraction and the solvent, the cylinders bend and form cylindrical micelles while the membranes close to polymersomes. [81] Block copolymers with a hydrophilic fraction larger than 50% and $P \leq 1/3$ tend to form spherical micelles. Along with the polymer nature, the solvent properties (including pH, polarity, viscosity, osmolarity, temperature) and the concentration also have an impact on which structure is preferentially formed. [115] In concentrated polymer solutions, different

structures (i.e. hexagonally packed cylinders, cubes, inverse structures, or lamellae) can be formed. With increasing copolymer concentration spherical micelles transform into cubic phases, then hexagonally packed cylinders and finally lamellae while cylindrical micelles directly form hexagonally packed cylinders. Vesicles first form hexagonally packed vesicles, then bicontinuous phases and finally also lamellea, whereas at high concentration also inverse structures have been observed. Generally, with increasing concentration, spherical assemblies change into cylinders and eventually membrane like structures.[115]

An important parameter to characterize the self-assembled structures is the shape factor (ρ), which is the ratio of the radius of gyration (R_g) and the hydrodynamic radius (R_h) (**Equation 1.4**). R_g and R_h are obtained by static light scattering (SLS) and dynamic light scattering (DLS) measurements, respectively. For homogeneously spherical structures, like micelles, R_g is smaller than R_h and therefore, $\rho < 1$. For a hollow sphere, ρ equals 1, since there is no mass in the cavity. For extended structures such as worms, $\rho > 1$. The combination of SLS/DLS is very useful, because it gives precise information about the size and architecture of formed structures using a non-invasive method.

$$\rho = \frac{R_g}{R_h} \tag{1.4}$$

Micrographs obtained by transmission electron microscopy (TEM) also provide information on the morphology of self-assembled structures. However, the harsh conditions of sample preparation might interfere with structure preservation. In particular, depending on the stiffness of their membrane some polymersomes collapse and will appear as deflated balls in negatively stained TEM images.

1.3.3 Polymersomes and micelles

Hollow polymer self-assemblies where the aqueous cavity is surrounded by a polymer membrane are called polymersomes (**Figure 1.4**). They can host a wide range of hydrophilic molecules including some antibiotics in their cavity[116] and hydrophobic compounds in their membrane. Polymersomes are very robust and thus, protect the integrity and activity of encapsulated compounds.[89] Micelles on the other hand have no aqueous cavity. Their hydrophobic core consists of the hydrophobic block(s) and is surrounded and shielded from the aqueous media by the hydrophilic block(s) (**Figure 1.4**). Micelles can be loaded with hydrophobic compounds.[93]

Depending on the polymers used, these polymeric self-assembled structures are usually biocompatible and have low toxicity.[117,118] In addition, the diversity of polymer building blocks allows them to be chemically tuned to respond to various stimuli, either internal (i.e. pH, enzymes, oxidative stress, etc.) or external (i.e. temperature, magnetic field, light, ultrasound).[119]

Some polymeric self-assemblies exhibit antibacterial activity in the absence of antibiotic cargos. Such intrinsic antibacterial activity has been reported for polymersomes based on the thermoresponsive block copolymer Poly[2-(2-methoxyethoxy)ethyl methacrylate]-Poly[2-(tert-butylaminoethyl) methacrylate] (PMEO 2 MA-b-PTA).[120] The PTA amino groups bear a positive charge and thus can interact with Ca^{2+} and/or Mg^{2+} ions of the bacterial membrane and consequently damage it. These polymersomes were tested on both Gram-negative *E. coli* and Gram-positive *S. aureus* at neutral pH 7.4 When solutions of

polymersomes were added to bacterial cultures, counting of the resulting colonies led to the conclusion that bacterial growth was prevented by the presence of PMEO 2 MA-b-PTA polymersomes. In another study, the conjugation of a synthetic, biodegradable block copolymer poly(ϵ-caprolactone) (PCL) with the antibacterial block poly[phenylalanine-*stat*-lysine-*stat*-(lysine-folic acid)] (Phe$_{12}$-*stat*-Lys$_9$-*stat*-(Lys-FA)$_6$) resulted in a polymer able to form antibacterial polymersomes in aqueous solution.[121] Similar to what was reported for the PTA amino groups, lysine residues that become positively charged in water mediate attachment to the bacterial membrane, enabling membrane penetration by the phenylalanine residues and the subsequent death of *E. coli* and *S. aureus*.

1.3.4 Nanoreactors and membrane permeability

Polymersomes can function as compartments or carriers for antimicrobial agents. They are considered catalytic nanocompartments, so called nanoreacters, when they host encapsulated enzymes or catalysts for the *in situ* produciton of active agents and enable the exchange of educts and products across the polymer membrane (**Figure 1.5A**).[122] Compared to lipid membranes, polymeric membranes are composed of heavier amphiphiles and their membranes are thicker. Due too this increased thickness,[89,123] they benefit from greater stability but are also known to be less permeable (**Figure 1.5B**).[91] PMOXA-

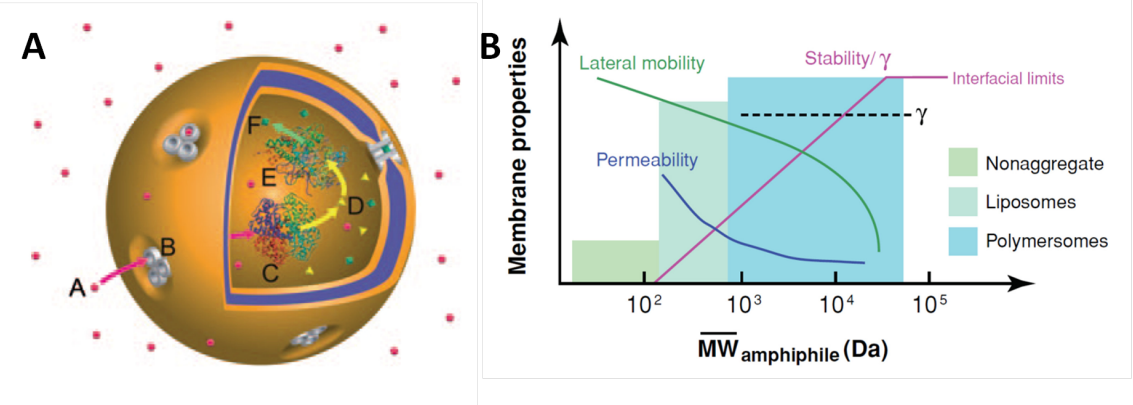

Figure 1.5: A) A schematic representation of a nanoreactor with two enzymes (C and E) encapsulated and able to conduct a cascade reaction from A to D and further to F. These substrates and products are able to pass through the membrane due to the insertion of protein channels (B).[124] B) Schematic plot of physical properties of vesicles versus the molecular weight of the corresponding amphiphiles.[91]

PDMS based block copolymer membranes, for example, are even impermeable to many ions and small molecules[125] except for dithiothreitol[126] or oxygen species, i.e. $O_2^{\bullet -}$.[127] However, in order for nanoreactors to be functional, the substrates, and products must be able to pass through the membrane, either into the cavity where the enzyme or catalyst resides or out of the cavity to keep concentration dependent inhibition of the enzyme from occurring. This can be achieved by several existing permeabilization techniques such as: (i) The use of block copolymers, which naturally form a porous membrane.[128] (ii) Chemical modification to create pores into the membrane.[129] (iii) Mixing polymerizable diblock copolymers, with nonpolymerizable phospholipids which can be removed from the membrane after self-assembly.[130]

(iv) The insertion of channel proteins, biopores, or ionophores[131–133] that allow the passage of specific reactants (e.g. divalent ions through ionomycin,[134] protons and monovalent cations through gramicidin,[135] electrons through the photosynthetic reaction center membrane protein,[136] or protons through proteorhodopsin[137]) or the passive diffusion of molecules up to a certain size through the membrane. The outer membrane pore F (OmpF, MWCO: 600Da)[138] is an example and the molecular weight cut-off (MWCO) can be reduced by using OmpF mutants (OmpF G119D, MWCO: 300Da).[139] Polymeric membranes are thicker than natural lipid membranes (**Figure 1.5B**) which then create for all natural biopores and membrane protein a hydrophobic mismatch between the hydrophobic domain of the synthetic membrane and the length of the biopore or membrane protein. However, due to the flexibility of the membrane, membrane pores and proteins can still be successfully reconstituted. Ionomycin for example could successfully transport Ca^{2+} across polymeric membranes which were up to 8.9 times thicker than the length of the pore.[140] Several factors (e.g. type of detergent and concentration, pH, membrane composition and membrane pore) and a combination thereof play a role in successful channel protein reconstitution. The design of experiment method, using a mathematical framework to keep the numbers of needed experiment low while still modeling results matching the experiments, has been successfully applied for the optimized insertion of proteorhodopsin, a light driven proton pump.[137] The channel proteins, biopores, or ionophores are inserted and reconstituted into the polymer membrane either already during the self-assembly process or by the external addition to the polymersome.

Furthermore, triggered passage across the membranes are possible such as by the insertion of modified OmpF rendering it pH responsive.[141] Similarly, responsive block-copolymers can be used for self-assembly to turn the membrane porous upon a certain trigger (pH, temperature, light, or enzyme degradation) by changing the hydrophobicity of one of the blocks to reversibly destabilize the membrane allowing the passage of small molecules or by degrading the whole membrane allowing the release of the encapsulated cargo.[116,119,142] To further improve the efficacy of such compartmentalized structures, membranes can be functionalized for targeting. This allows them to release their cargo close to the place or inside the cells needed.[143]

1.4 Nanoscience based delivery of Antibiotics

1.4.1 Polymersomes loaded with antimicrobial agents

An example of applying polymersomes to battle bacteria is the efficient treatment of *Porphyromonas gingivalis (P. gingivalis)* infected oral keratinocytes with drug-loaded polymersomes.[144] Specifically, metronidazole and doxycycline antibiotics have been encapsulated in poly[2-(methacryloyloxy) ethyl phosphorylcholine] (PMPC) - poly[2-(diisopropylamino) ethyl methacrylate] (PDPA) polymersomes. The PMPC block interacts with specific plasma membrane receptors that promotes endocytosis. The PDPA block is pH-responsive, which is very important and serves as a trigger for antibiotic release. Accordingly, polymersomes disintegrate at the acidic pH of the endosomal-lysosomal compartment (pH 6.5-4.5) releasing their cargo. The effect of antibiotic loaded PMPC-PDPA polymersomes was tested *in vitro*. H357 and TR146 human oral squamous cell, carcinoma-cells, and NOK cells (immortalized oral keratinocytes) were infected with *P. gingivalis* and then incubated with antibiotic loaded polymersomes. Apart from these three cell lines, a

tissue-engineered oral mucosa that more closely represents the physiological conditions of a living organism was used as a test model. Even though *P. gingivalis* were not completely eradicated from either of the test systems, the results strongly indicate that metronidazole and doxycycline loaded polymersomes were uptaken by the cells, disintegrate in the endosomal compartment and show antibacterial activity. Subsequently, pH responsive PMPC-PDPA polymersomes were loaded with a number of antimicrobial drugs including gentamicin, lysostaphin, vancomycin, rifampicin, and isoniazid.[145] Their potential to reduce intracellular pathogens was tested both *in vitro* and *in vivo*, in monocyte-derived macrophages (THP-1 cells) and embryos of zebrafish (Danio rerio), respectively. Both THP-1 cells and the zebra fish embryos were infected with either *S. aureus, Myobacterium bovis-attenuated Bacillus Calmette–Guérin (M. bovis-BCG), Myobacterium tuberculosis (M. tuberculosis)*, or *Myobacterium marinum (M. marinum)* bacteria. After screening all possible combinations of cargoes and infected model systems, antimicrobial loaded polymersomes were found to inhibit the bacterial growth both *in vitro* and *in vivo* in all the cases.

Moreover, copolymerisation of 2-hydroxyethyl methacrylate (HEMA) and poly(ethylene glycol) methyl ether methacrylate (O950) yielded a library of block copolymers. Selected copolymers were found to spontaneously form polymersomes and to be pH responsive.[146] Loaded with the hydrophilic antibiotic drug ceftazidime, these pH responsive polymersomes were incubated with RAW 264.7 murine macrophages previously infected with *Burkholderia thailandensis (B. thailandensis)*. In order to evaluate the impact of the ceftazidime containing polymersomes on the bacterial growth, treated RAW 264.7 cells were examined by fluorescence microscopy and colony forming units (CFUs) were counted. Similar to the findings described above for PMPC-PDPA polymersomes, ceftazidime was released when pH-responsive polymersomes had reached the endosomal compartment and inhibited bacterial growth to a noticeable extent.

A different approach is based on the co-assembly of polymersomes derived from poly(ϵ-caprolactone)-*block*-poly(lysine-*stat*-phenylalanine) PCL-*b*-P(Lys-*stat*-Phe) block copolymers and hydrogels made from dibenzaldehyde-functionalized PEG (DF-PEG) block copolymers that appear to show "quick" and "long-term" antibacterial function.[147] Here, both the polymersomes and the hydrogels contain the antibiotic penicillin G from Penicillium chrysogenum. The porous structure of the hydrogels allows for the release of penicillin G as well as the release of antibiotic containing polymersomes. The presence of penicillin G within the hydrogels allows for fast antibacterial action ("quick" release). However, the half time of penicillin G is rather short, up to 30 min. By incorporation into polymersomes, penicillin G is protected and its activity is extended through a long-term release. At the same time, these specific polymersomes exhibit intrinsic antimicrobial activity: the positively charge lysine residues of the surface-exposed P(Lys-*stat*-Phe) corona can bind to the negatively charged bacterial membranes and disrupt them. In addition, the interaction of the polymer membrane with the bacteria facilitates the release of the antibiotic cargo. The hydrogel-polymersome system was tested in *S. aureus* (Gram-positive) and *E. coli* (Gram negative) bacteria cultures and was shown to effectively reduce their viability. Furthermore, these studies revealed that the coexistence of hydrogels and polymersomes was critical to significantly extend the duration of penicillin G release.

1.4.2 Inorganic NP delivery

Inorganic NPs were introduced as promising antibacterial agents but they face the limitation of low specificity and high toxicity in eukaryotic cells.[148] Conceivably, these limitations can be overcome by encapsulating NPs in polymer-based assemblies such as polymersomes or micelles. Hence, the antibacterial activity of inorganic NPs is combined with the enhanced stability and biocompatibility of polymer nanostructures.

In a fundamental study, silver nanoparticles (AgNPs) were incorporated into the membrane of polymersomes and the resulting nanostructures were tested for antimicrobial activity *in vitro*.[149] Specifically, PEO-*b*-P(DMA-*stat*-tBA) block-copolymer was synthesized and was shown to self-assemble into polymersomes in aqueous solution. The polymersome solution was then mixed with an $AgNO_3$ solution and solid $NaBH_4$ was added under stirring. As a result, AgNPs formed within the polymersome membrane. The Ag-decorated polymersomes were evaluated for their antibacterial efficacy *in vitro*. When Gram-negative *E. coli* were exposed to the Ag-decorated polymersomes, MIC and Minimum Bactericidal Concentration (MBC) were low, and the inhibition of bacterial growth was rather high. In a next step, methoxypoly(ethelyne glycol)-poly(D)-(L)-lactic acid (mPEG-PDLLA), a biodegradable block copolymer, was used to produce polymersomes with AgNPs incorporated into the hydrophobic part of the membrane. Additionally, the hydrophilic cavities of the mPEG-PDLLA polymersomes were loaded with ampicillin. The potential antimicrobial activity of the AgNPs and antibiotic containing mPEG-PDLLA polymersomes was tested by monitoring the proliferation (CFU mL^{-1}) of a suspension of ampicillin-resistant *E. coli*.[150] The optical density at 600 nm (OD 600) was measured for 24 hours following their treatment with free ampicillin, Ag containing polymersomes without ampicillin, and ampicillin containing polymersomes without silver nanoparticles. From this study resulted that the combination of Ag and ampicillin in polymersomes was able to significantly inhibit the bacterial growth, whereas with the other treatments, the bacteria were able to proliferate.

Other examples of inorganic NPs on the membrane and antibiotic in the aqueous cavity include mPEG-*b*-PDLLA based polymersomes hosting the antibiotic methicillin in the hydrophilic core and hydrophobic superparamagnetic iron oxide nanoparticles (SPIONs) in the membrane bilayer.[151] These assemblies are called iron oxide-encapsulating polymersomes (IOPs). Biofilms formed by *Staphylococcus epidermidis (S. epidermidis)* grown on glass cover slips were incubated with IOPs. Taking advantage of the magnetic properties of SPIONs, a magnet placed underneath the coverslip was used to attract the IOPs and make them penetrate the biofilm. The unique combination of SPIONs and antibiotic within polymersomes exposed to a magnet resulted in a uniform penetration and subsequent eradication of the biofilm, making it a weapon of great potential against drug resistant bacteria.

1.4.3 Antimicrobial producing Nanoreactors

Nanoreactors assembled from the amphiphilic block copolymer poly(2-methyloxazoline)-*block*-poly(dimethylsiloxane-*block*-poly(2-methyloxazoline) (PMOXA-*b*-PDMS-*b*-PMOXA) that were loaded with the enzyme penicillin acylase (PA) were able to locally produce antibiotics.[152] To obtain these vesicular catalytic nanocompartments, the polymer was dried together with the bacterial porin OmpF to a thin film which was then rehydrated in a

buffer containing PA. This way, OmpF was inserted in the membrane of the resulting polymersomes, forming a protein gateway that allows the diffusion of molecules up to around 600 Da. In parallel, PA was encapsulated in the hydrophilic cavity of the nanoreactors. When the externally added substrates 7-aminodesacetoxycephalosporanic acid (7-ADCA) and phenylglycine methyl ester (PGME) diffused into these catalytic nanocompartments, an enzymatic reaction took place in the cavity and cephalexin was produced. Cephalexin is a well-known antibiotic disrupting the growth of the bacterial cell wall of *S. aureus, S. epidermidis, E. coli* and *Proteus mirabilis (P. mirabilis).*[153,154] To confirm the antibiotic activity of the produced cephalexin, the effects of PA-loaded nanoreactors on the growth of *E. coli* were monitored in the presence and absence of substrate. Notably, the growth of *E. coli* was inhibited by the presence of the antibiotic producing nanoreactors which remained active (i.e. they kept producing cephalexin) for seven days under physiological conditions.

Similarly, a light-sensitive, water-soluble tetraalkylpyridinium porphyrin (TpyCP) was encapsulated into PMOXA-*b*-PDMS-*b*-PMOXA polymersomes and evaluated for its antimicrobial activity against *E. coli.*[112] TpyCP is a photosensitizer, that upon irradiation (e.g., LED light of 660 nm wavelength) is able to induce reactive oxygen species (ROS) production and cause oxidative stress in target cells *in vitro*. The particular advantage of this system is that only the ROS produced in the aqueous cavity of the polymersomes diffuse across the polymer membrane and reach the bacteria of interest, whereas TpyCP remains encapsulated. This compartmentalization allows for a selective and controlled process. The antimicrobial activity of light-induced ROS was demonstrated by irradiating *E. coli* cultures that were incubated with porphyrin containing polymersomes. Counting CFUs and imaging of corresponding *E. coli* cultures by confocal laser scanning microscopy (CLSM) strongly indicated that TpyCP-polymersomes caused a significant decrease of the *E. coli* population only when irradiated (**Figure 1.6**).

1.4.4 AMP delivery

To target AMPs to specific sites and protect them from untimely degradation, they were combined with different nanocarriers.[155] A cationic AMP, for example, was mixed with an anionic block copolymer and based on electrostatic interaction self-assembled into negatively charged polyion complex micelles. After one day 50% of the peptide was released. Afterwards, the release slowed down and reached 80% of cumulative release after 3 days where it then stagnated. Compared to free AMP, the hemolytic toxicity could be reduced while the antimicrobial activity was preserved.[156] The loading and release of positively charged human model AMP LL-37 was influenced by the surface charge and surface area of silica NP carriers. Higher amounts can be loaded into negatively charged mesoporous silica NPs compared to positively charged mesoporous or non-porous silic NPs. Furthermore, the peptide was protected from degradation due to its preferred location within the mesopores of the mesoporous silica NPs.[157] The same peptide self-assembled with oleic acid into cylindrical micelles leading to pH responsive nanocarriers which were antimicrobial active at pH 5 and inactive at pH 7.[158] Furthermore, among other AMPs, this peptide was also loaded on anionic poly(ethyl acrylate-co-methacrylic acid) microgels, which protected these peptides from degradation. Under physiological salt concentration the loaded peptide was released and could efficiently act against several bacteria.[159,160] When formulated with PEGylated phospholipid micelles, the aggregation of an aurein derived peptide could be decreased as well as the cytotoxicity eased.[161] Importantly, molecular dinamics

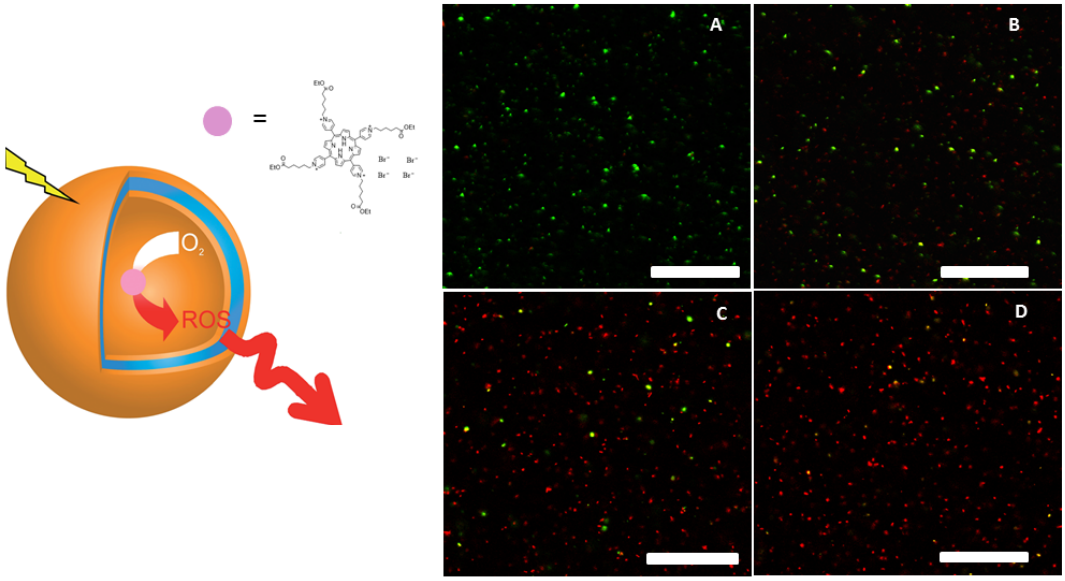

Figure 1.6: Left panel, schematic of porphyrin containing polymersomes. Right panel, *E. coli* bacteria incubated in presence of 200 μM TPyCP loaded polymersomes were stained with SYTO 9 (considered alive, green) and propidium iodide (considered dead, red) after 0 min (A) 30 min (B) 120 min (C) and 360 min (D) of illumination with red LED light (λmax = 660 nm).Scale bars: 10 μm.[112]

simulations of the AMP magainin2 indicated that the peptide preserved its secondary structure when encapsulation in PEG, PLGA, or copolymer micelles.[162]

1.5 Antimicrobial surface strategies

1.5.1 Passive Strategy - micro- and nanostructured surfaces

Whereas the production or release of specific chemicals provides mechanisms for active defense against bacteria and the formation of biofilms, surface micro-structures represent passive mechanisms, which are non-toxic since no biocides or inhibiting agents are released to the environment. In nature, various organisms use such passive defense strategies against bacterial colonization, and these have inspired the development of biomimetic antibacterial surfaces.[170–172] Models of surface textures from sea organisms, such as sharks,[165] pilot whales,[164] sea stars[166] and mussels,[167] have been investigated because these animals have few problems with fouling organisms. The skins of these different animals are patterned with special microstructures (**Figure 1.7a**),[163] and the spacing between them is regarded as a key property for inducing antifouling performance.[173] Studies on the relationship between feature size and antifouling property indicated that the lowest level of attachment was for structures of the order of 2 μm (similar to the feature size of the skin of pilot whales and smaller than zoospores).[168] The textures of pilot whale skin have been tested for their non-fouling properties, and nano- and micro-structure coatings that mimic whale skin have been fabricated by multilayers of spray-coated polyacrylic acid and

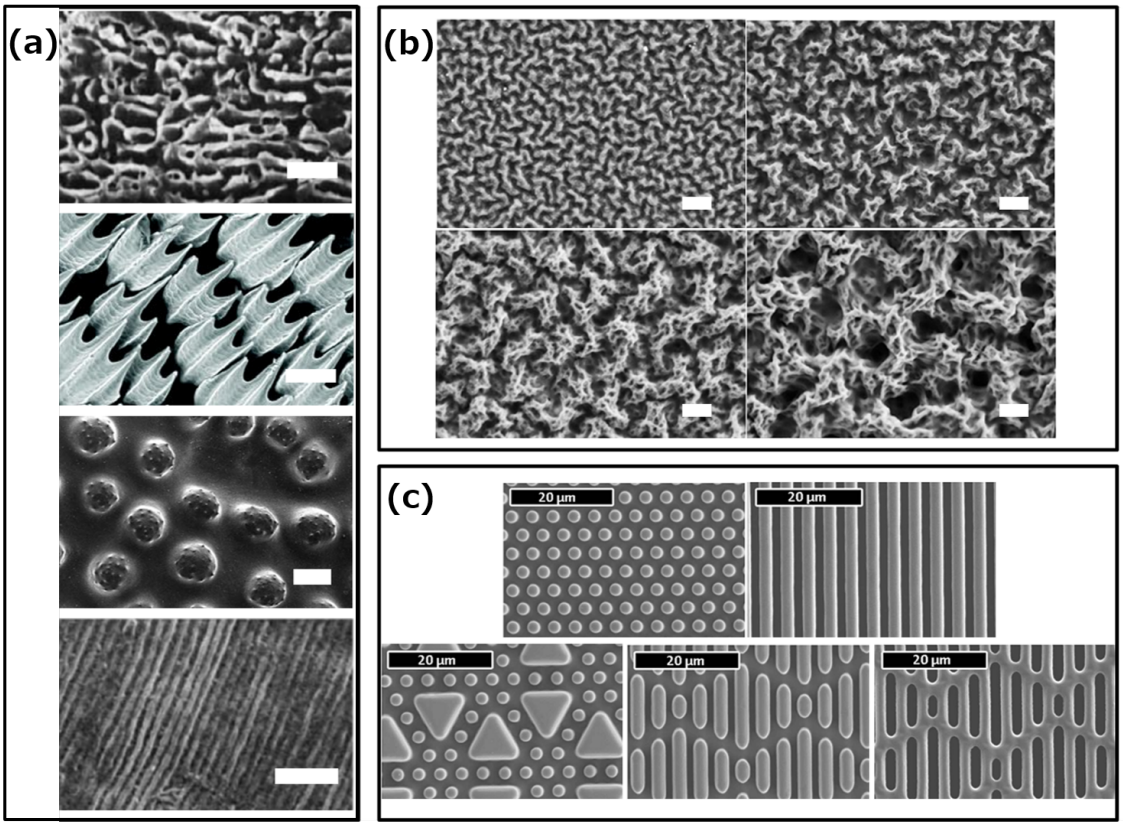

Figure 1.7: (a) Surface topography of various natural models that resist fouling:[163] pilot whale,[164] shark,[165] sea stars,[166] and mussels[167] (from top to bottom; the scale bars are 1 μm, 100 μm, 100 μm, and 10 μm, respectively). (b) SEM images of polyacrylic acid-polyethylene imine multilayers inspired from pilot whale skins. Scale bars: 1 μm.[168] (c) SEM images of shark skin inspired surfaces with engineered patterns on PDMS elastomers with a spacing of 2 μm.[169]

polyethyleneimine (**Figure 1.7b**).[168] The ridged platelet structures on shark skin,[165] are considered to be a key factor in the prevention of biofouling,[174] and hierarchically wrinkled surfaces remained free of fouling for more than a year in field tests.[175] Various patterns, such as pits, pillars, ribs, channels and ridges, that mimic natural surface structures have been produced using photolithography with a constant spacing of 2 - 20 μm between organized nanosized features (**Figure 1.7c**).[169,174] Attachment of Cobetia marina, a gram negative bacterium larger than these surface features, was two orders of magnitude lower on the structured surface than on smooth polydimethylsiloxane (PDMS).[169] Sharklet^{TM}, a product inspired by shark skin is already being marketed, and has been shown to reduce settled microorganism density by 86% compared to a smooth surface.[174]

An approach for preventing biofilm formation is the modification of surfaces with synthetic organic compounds, often biocompatible polymers (**Figure 1.8a**) which directly reduce bacteria adhesion to the device.[176] For example, polyamide reverse osmosis membranes are protected from the attachment of bacteria through a phosphorylcholine block copolymer coating.[176] This is sufficient to reduce bacterial growth by at least a factor of 10. Atifouling strategies, preventing protein adsorption being the first step in the forma-

tion of biofilms, have been developped with polymer brushes.[177,178]

Another example of bioinspired synthetic surface pattern was obtained by replicating the structure of macroalgae. A macroalgae mold in PDMS was filled with epoxy doped with furanone to obtain artificial microstructured surfaces, which showed 40% less biofouling than pure epoxy blanks, and thus demonstrated that both the chemistry and topography affect antifouling properties.[179] Using microwave plasma chemical vapour deposition on a silicon surface, diamond nanocones have been engineered to mimic the topography of cicada fly wings (**Figure 1.8b**). Although this structure did not inhibit the development of bacteria, it killed up to 18% of them at the surface.[180]

Nanostructured surfaces for instance can be created via direct addition of patterned nano-objects to kill bacteria once they reach the surface. High-aspect-ratio surfaces have been produced with silicon nano-pillars patterned by the deep reactive ion etching technique with SF_6 and O_2 gases in the etch cycle and C_4F_6 gas in the deposition cycle. These silicon nano-pillars, with random interspaces, increased the contact angle of a silicon surface from 75° to 154° and led to up to 86% death of bacteria on their surfaces.[181] This strategy modifies surface topography so that the attachment and growth of pathogens is avoided, but without mimicking natural surfaces.[182] By creating micro- or/and nano-structured roughness, such surfaces can decrease bacterial growth by being very hydrophobic.[183] The topography can be shaped with biocompatible polymers, such as PDMS, polystyrene, polycarbonate or polyethylene to obtain a desirable roughness and hydrophobicity with contact angles increasing from 60-90° before, to 150° after restructuring.[184] These structured surfaces massively decrease bacteria adherence to <0.1% of biofilm compared to unstructured surfaces. Surfaces have also been patterned with different microscale motifs (e.g., pillars, cross pillars, hexagonal pillars, and hexagonal pits) to inhibit bacterial growth to 11% of coverage compared to the control surface.[185] The topographical approach to preventing biofilm formation by i) controlling surface-roughness and -pattern to prevent bacteria adherence, or by ii) adding patterned nano-pillars to kill bacteria shows promising results in antifouling and bactericidal properties, and thus represents a solution with high potential for protecting medical devices from pathogen infections.

1.5.2 Active Strategy - surface releasing active agents

Most developed solutions for coatings against DAI are based on layers that entrap antimicrobial agents[44,186] to provide controlled release of drugs (**Figure 1.8c**). Antibiotics directly incorporated in polymer coatings resulted in a controlled and constant release of the drug during 7 days, and induced a decrease in DAI in animal models.[187]

Another possible active strategy is to load the surface with AMPs. They have been immobilized on metal-,[188,189] nanoparticle-,[190] polymer-,[191,192] polymer/ lipid-based-,[62] or microgel-surfaces,[193,194] by various physical or chemical methods.[195] For example, two AMPs have been coupled to polycarbolactone. 4 mol% of this AMP-Polymer mixed into a polymer film was enough to completely kill Methicillin-Sensitive *s. aureus* (MSSA).[191] Magainin II was covalently bound to stainless steel surfaces, decreasing bacteria attachment and showed biofilm resistant abilities.[189] A cationic AMP was electrostatically anchored on titanium nanostructured surfaces from where it was released over several hours to actively kill bacteria.[188] Another AMP, cecropin-melittin, was immobilized with high density on gold nanoparticle-coated surfaces. Conceivably, the high density of the AMP could be

achieved through the increase in surface area from the nanoparticles.[190] KYE28, another AMP was incorporated in surface immobilized microgel multilayers, thereby improving antimicrobial effects compared to untreated glass surfaces or peptide-loaded monolayers.[194] Peptides, immobilized on polydopamine coatings have been used to prevent bacteria adhesion,[196] or entrapped in polymer matrix coatings to increase the antimicrobial effect of free peptides and to keep them at the interface of devices with their biological environment for up to one month. This controlled their release without producing possible toxicity to mammalian cells.[197] Using compounds that are degraded by pathogens to release drugs to inactivate bacterial growth is a very interesting approach;[198] for example, the destruction of polysaccharide multilayer films with entrapped AMPs by secretions of bacteria and yeast led to peptide release and resulted in the destruction of the pathogens.[64] Since sterilization of surfaces, for example by autoclaving, is prerequisite for most biomedical applications, some of the immobilized peptides were tested for heat stability and the surfaces were shown to retain their bactericidal efficacy.[199]

Biofilm formation can also be prevented by directly using the properties of metallic elements incorporated in or grafted on the surface of medical devices (**Figure 1.8d**). AgNPs can be synthesized in an eco-friendly way[200] and are nowadays the main inorganic nanoscience-based surface modification of medical devices.[201,202] These NPs have the advantage of being a stable store of silver and thus having longer use than classical Ag^+.[20,203] AgNPs are usually functionalized with chemical agents to improve their aqueous stability and dispersion[20,26,59] before being linked to device surfaces that have been previously functionalized with polymers,[201] hydrogels,[20] or chitosan.[26] These strategies allow entrapment of AgNPs at the interface between the medical device and the biological environment, and the release of Ag^+, the active bactericide state of silver.[203] AgNPs have shown very high antimicrobial properties by decreasing bacteria present on chitosan gel[26] or polymer brushes[201] by $> 99.8\%$ 24 hours after exposure. Ag^+ release was demonstrated to be an important parameter in long-term antibiofilm activity, reducing bacteria adhesion and proliferation *in vitro*,[26] and even leading to an *in vivo* decrease of DAI in rats.[203] AgNPs have not shown yet any direct toxicity because of prior coating of the NPs with chemical agents or of the biocompatible surfaces onto which they were entrapped,[20,203,204] although a study has shown that AgNPs can cause hemolysis.[205]

A recent development has been the use of drug encapsulated vesicles,[144] or surface immobilized nanoreactors.[206] Micro- or nano-spheres of polylactic acid-polyvinyl alcohol were loaded with usnic acid, the release of which prevented biofilm formation by reducing the amount of bacteria by $>$ 10,000 times after 72 hours incubation with *S. aureus*.[207] Immobilized nanoreactors loaded with enzymes are able to produce antibiotics "on demand" (**Figure 1.8e**).[152,206] They act as self-defending surfaces which allow locally controlled drug production at a specific rate for long periods of time by adding the required amounts of substrate to the outer medium.

1.5.3 Techniques to immobilize self-assembled nanostructures

Various methods exist to immobilize nanostructures, including covalent and non-covalent strategies. In most cases, the nanostructures are equipped with surface modifications complementary to those of the surface onto which they are immobilized. Non-covalent interactions include the receptor ligand pair biotin-streptavidin, where different immobilization strategies are employed. For example, streptavidin is added to a biotinylated surface

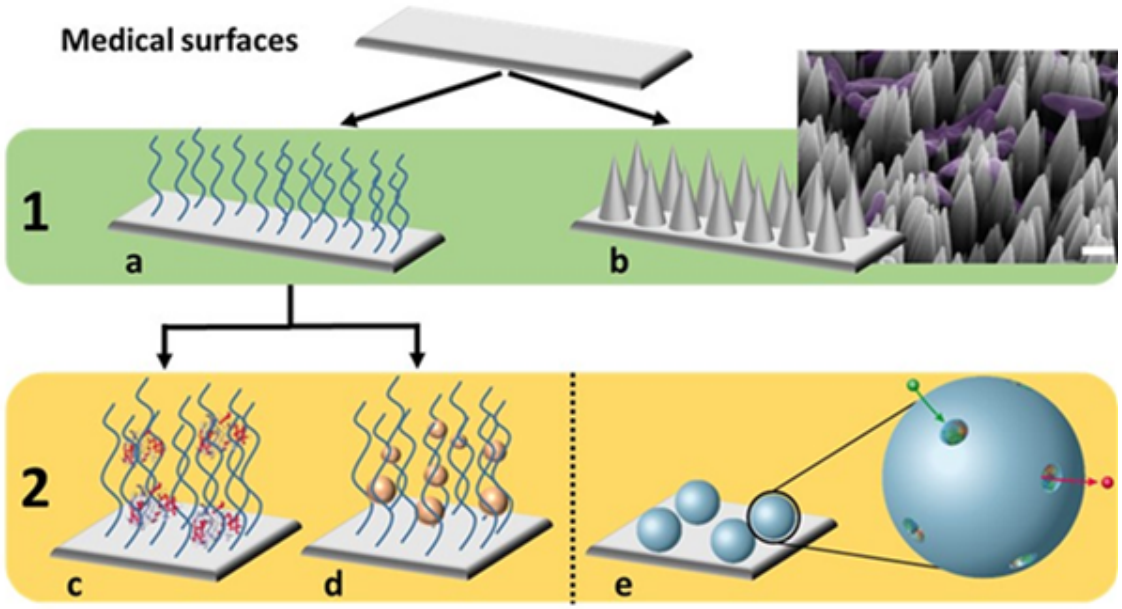

Figure 1.8: A summary of possible synthetic surface nano-functionalization approaches for preventing DAI. 1) Antifouling properties: surfaces can be (a) coated with organic compounds or (b) patterned (scale bar = 1 ρm)[180] to avoid growth of bacteria. 2) Antimicrobial properties are provided via (c) peptides/drugs or (d) nanoparticles entrapped in the organic coatings. Another antimicrobial solution could be (e) the direct grafting of a nanoreactor onto the surface to control drug release.[206]

and biotinylated polymersomes are then immobilized on the surface by binding to steptavidin.[208–211] Using a plasma-polymerized acrylic acid surface that exposes strepdavidin to interact with biotinylated polymersomes also leads to successful immobilization.[212] Another non-covalent immobilization method is based on the adamantane-β-cyclodextrin host-guest complexation. Here the adamantane moiety on polymersomes fits tightly into the cavity of β-cyclodextrin which is accessible on the substrate surface.[213] Electrostatic interactions enable the reversible immobilization of polymersomes via Mg^{2+} bridges[214] or the immobilization of negatively charged (COO^-) polymersomes on positively charged ($NH_3{}^+$) surfaces.[215]

Covalent interactions include the prominent Schiff-base formation between aldehyde functionalized surfaces and amine functionalized polymersomes[216] or vice versa[217] with possible further reductive amination.[206] In the thiol-ene click reaction, the double bond of methacrylate exposed on polymersomes covalently binds to thiol functionalized surfaces.[218] Another covalent immobilization mehtode is based on the Copper (I) catalyzed alkyne azide cycloadditon (CuAAC). Azide functionalized polymersomes can covalently bind to alkyne functionalized surfaces, forming a stable triazole linker.[219] However, the cytotoxicity of Cu(I) represents a significant limitation of this well-established reaction in biological applications. With the strain promoted azide alkyne click (SPAAC) reaction, a catalyst free reaction pathway was developed that overcomes this limitation,[220,221] which was then optimized for polymersome immobilization described in detail in chapter 3.[222] Another covalent immobilization technique developed in chapter 4 is based on the thiol-maleimide Michael addition,[223] which was used to covalently link proteins to

polymersomes.[224]

1.5.4 Functional surfaces due to immobilized nanostructures

Specialized surfaces (e.g., hydrophilic, hydrophobic, reflective, non-adhesive, anti-fouling, drug releasing surfaces) play an important role in everyday life such as in cars, windows, displays, or medicine. Their properties and behavior is tuned towards their function and desired application. Especially for medical application such as implants, stents, or catheters optimized surfaces are crucial and can decide over the outcome of a surgery for instance. Active molecules can be immobilized on the surface. However, free compounds can get degraded fast by the complex environment, which keeps the surface active for only a short period of time. Nanostructures (e.g., Polymersomes, liposomes, micelles, particles) are able to protect such active agents by shielding them from the harsh environment.[93] Furthermore, the nanostructures can be designed to release the active agent when needed.[92,93,225] Therefore, immobilized self-assembled nanostructures have gained a lot of interest in recent years. If such nanostructures are immobilized permanently on the surface, not only would the active agent be released at the site of interest, but its lifetime would be prolonged, and it would even be possible to control the release of the active substance over longer periods of time. These benefits have made immobilized polymeric nanostructures hot topics in recent years.

The described immobilization techniques can be applied to the nanoreactors or drug carriers. For polymersomes to be functional on a surface, i.e. create an active surface, it is crucial that despite being immobilized they remain responsive to redox state, light, pH etc. To show that immobilized vesicles with a disulfide cross-linked polymer shell maintain their redox responsive release properties, polymersomes with encapsulated carboxyfluorescein (CF) were exposed to the reducing agent tris(2-carboxyethyl)phosphine (TCEP).[210] The resulting change in redox potential triggered the release of CF as visualized by a 10 hour increase of fluorescence. To evaluate pH responsiveness, polymersomes were loaded with pyranine, a pH sensitive dye, and immobilized on a glass substrate.[226] Depending on the pH of the surrounding buffer, the fluorescence was either increased (pH 8) or quenched (pH 6). Compared to free polymersomes, the immobilized ones retain their responsiveness although their physical behavior may change. If polymersomes are free in solution, their swelling, which is induced by a change of pH, occurs equally in all directions. Interestingly, immobilization causes them to swell more in z direction than in the lateral direction.[213] This indicates that immobilization of nanostructures on a surface has an influence on the physical properties.

Surface-immobilized nanostructures also have great potential in biosensing applications.[227] In particular, surfaces coated with catalytic nanocompartments can be used as detecting platform. For example, ribitol, a model sugar alcohol was detected by means of surface immobilized polymersomes loaded with the enzyme ribitol dehydrogenase (RDH).[227] To allow selective diffusion of sugar alcohols across the membrane into the cavity where RDH was encapsulated, the *E. coli* glycerol facilitator (GlpF) had been incorporated into the membrane of these polymersomes. Nanoreactors can also be immobilized in a distinct pattern as demonstrated for polymersomes encapsulating acid phosphatase.[208] To obtain the patterned nanostructures, the surface was first micro-contact printed with biotin and then strepdavidin was added to immobilize the biotinylated catalytic nanocompartment. These patterned catalytic nanocompartments successfully dephosphorylated the fluoro-

genic substrate ELF 97.

Intriguingly, it has been shown that immobilized cationic NPs are more effective in killing bacteria than free NPs in solution.[228] This could be due to the lack of movement of the NPs during the interaction with the bacteria. Poly(L-lactic acid) (PLLA) nanoparticles containing AgNPs and the detergent polyvinyl alcohol (PVA) as a stabilizer were immobilized through electrostatic interactions between negatively charged COO^- groups on the PLLA nanoparticles and positively charged NH_3^+ groups on the substrate (**Figure 1.9a**).[229] This surface was able to reduce biofilm formation up to 98% compared to immobilized PLLA nanoparticles which are lacking the AgNP. PLLA itself is not having any influence on biofilm growth. However, it might facilitate silver ion availability as lactic acid, a degradation product of PLLA, enhances the permeabilization through the bacterial cell wall. Additionally, the decrease in local pH due to lactic acid might enhances the oxidation and dissolution of the AgNP.

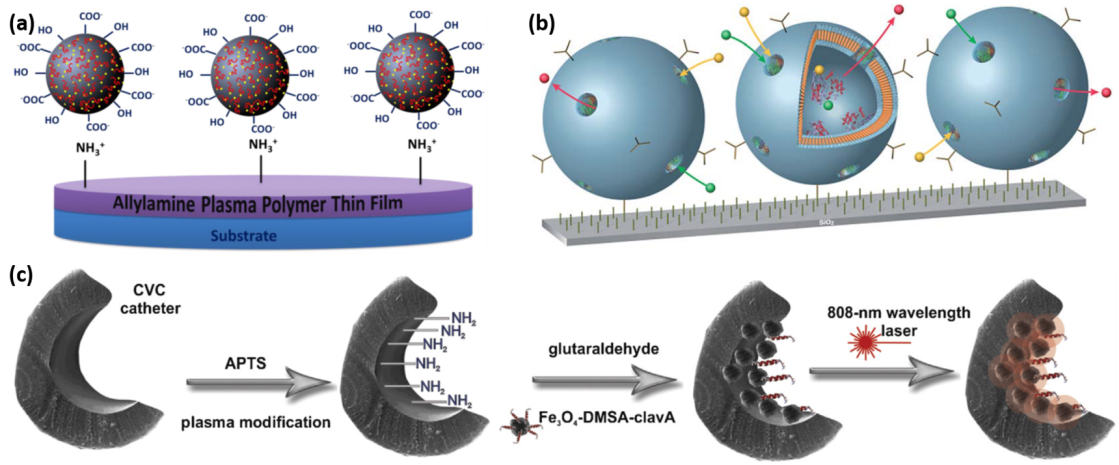

Figure 1.9: Schematic representation of various strategies to design antimicrobial surfaces by immobilization of different active nanostructures. (a) PLLA-AgNP nanoparticles are immobilized on an Allylamine plasma polymer thin film. The large grey spheres represent the PLLA nanoparticles, the yellow dots the AgNP, the red squiggles the detergent PVA.[229] (b) Catalytic nanocompartments encapsulating the enzyme PA are immobilized on silica wafers. OmpF is used to create pores in the polymersome through which the educts 7-ADCA and PGME (yellow and green dots) as well as the product cephalexin (red dots) can diffuse.[206] (c) CVC are modified with APTS to obtain amino-functionalized surfaces on which iron oxide NPs containing the AMP clavA are immobilized. An 808 nm wavelength laser causes local hyperthermia and ablation.[230]

The previously discussed nanoreactors that are able to produce the antibiotic cephalexin[152] have been immobilized through Schiff-base formation with further reductive amination on a silica surfaces (**Figure 1.9b**).[206] After immobilization, the nanoreactors stayed active and were able to produce and release the antibiotic over up to 7 days. This is a strong indication for a prolonged activity of immobilized nanocompartments in comparison to nanocompartments that are free in solution. Surfaces with immobilized nanoreactors were able to reduce bacteria attachment and proliferation.

AMPs, which often are natural peptides, obtained a lot of attention in recent years.[61,66] On the one hand, they do not seem to evoke resistance, on the other hand, they are able to selectively destroy bacterial membranes. The AMP clavanin A (clavA) was attached on iron oxide (Fe_3O_4) NPs functionalized with dimercaptosuccinic acid (DMSA).[230] These Fe_3O_4-DMSA-clavA NPs were then immobilized on the inner wall of a central venous catheter (CVC) which was previously functionalized by aminopropyl trimethoxysilane (APTS) to create an amino surface (**Figure 1.9c**). The clavA on the immobilized NPs was able to disrupt bacterial membranes. The CVC modified with the Fe_3O_4-DMSA-clavA NPs reduced gram negative bacteria attachment by nearly 90% compared to non-modified CVC. Furthermore, 808 nm wavelength laser irradiation causing a local hyperthermia and ablation which promotes adhered bacterial annihilation, was able to reduce already formed biofilms.

1.5.5 Key requirements for efficient antimicrobial surfaces

We are surrounded by specialized surfaces in our everyday life. Depended on the application of the surface, different requirements have to be fulfilled. Antimicrobial surfaces have to be able to efficiently kill bacteria and thereby decreasing the bacteria population over time or prevent bacteria from attachment. Furthermore, when such potent surfaces are applied in the biomedical field strict requirements have to be met. Antimicrobial coatings need to withstand any mechanical stresses exposed during application while maintaining long term stability and specific mechanical and physical properties.[1] For example, the mechanical stability the AMP GL13K coating, has been shown to be unaffected by ultrasonication which simulates *in vivo* fluid forces.[63] Coatings need to be resistant toward any kind of degradation, as well as have mechanical and thermochemical stability for the long-term retention of the coated substance thereby ensuring the antimicrobial effectiveness. No possible toxic or harmful compounds are allowed to be released at any time during application, neither through passive release or mechanical abrasion. Therefore, it is advantageous to reduce as much as possible toxic compounds throughout the production of the surface. Destructive factors leading to abrasion like shear forces or yield stresses are different for each environment; thus the antimicrobial surface needs to be designed specifically for the desired application in order to achieve required mechanical stability and minimize the amount of wear particles as much as possible.[231,232]

The antimicrobial surface needs to maintain its function over a lengthy time period under defined conditions without excessive expenditure on maintenance or repair. It is important to test the surfaces in relevant biological fluids (e.g. blood) due to the presence of macromolecules (e.g.proteins in blood) that can cover antimicrobial surfaces eliminating their antimicrobial activity. In drug delivery systems the finite release property of antimicrobial compounds limits their use in implants due to the release of antibiotic concentrations below the MIC after a certain time point. For short-term implants (e.g., catheters), the finite release property is not a problem as the implant is removed before full release of the antibiotic. However, for long-term implants, continuous strong release of antibiotics is crucial within the first few hours postimplantation, while the immune system is weakened and the implant is most susceptible to bacterial colonization.[1] To circumvent the finite release problems, surfaces which regenerate the antimicrobial activity have been studied.[201] An alternative solution is to use "smart antimicrobial surfaces" based on immobilized nanoreactors that produce antibiotics "on demand." This strategy is very promising as they are only active when needed and can be designed to be sensitive and responsive to

specific stimuli, such as enzymes[198] or external substrates.[206]

The antimicrobial surface should not be toxic, injurious, or physiologically reactive or cause unwanted immune responses. It is crucial that the material is compatible with tissue and biological fluids of a living system. Testing the biocompatibility of coatings is generally performed *in vitro* by evaluating the interactions between the surface and recognized cell culture lines.[1] However, such *in vitro* conditions do not adequately address the acceptability of antimicrobial surfaces in environments with blood contact for a prolonged time (e.g., central venous catheters). Interactions of these coatings with blood are critical for the functioning of the device. Therefore, the hemocompatibility of such surfaces needs to be studied. This can be done by determining platelet activation and adhesion and haemolysis in human blood,[65] even under high pressure and high-shear arterial flow.[233] The antimicrobial action of the surface should act on specific targets rather than using a wide spectrum of antibiotics in order to avoid or slow down bacterial resistance. AMPs are a promising alternative to conventional antibiotics, because they possess broad antibiotic effects, but supposedly induce less resistance than conventional antibiotics.[62,68]

Depending on their locations, medical devices can be classified as: i) totally external, ii) percutaneous and permucosal, or iii) totally internal implanted devices. Totally external devices as for example contact lenses usually do not present serious risks of infection to the patient because they can either be designed for single use or allow sterilization during the utilization if necessary. Percutaneous and permucosal devices (e.g., dental implants, central venous catheters) are invasive, being partially internal to the body tissues, and therefore with high risks of infections. Ideal surfaces of percutaneous and permucosal devices have to support osseointegration and perimucosal sealing, because it is important to resist periimplant infections, for example, periimplantitis.[63] Totally internal implant devices are usually contaminated because of specific reasons in restricted circumstances, for example, implant surface contamination before or during surgery, or hematogenous seeding from a distant infected site.[14] Short-term totally internal implant devices might not require a permanent coating and they can be used together with release of antimicrobials into the surrounding tissue. For long-term totally internal implant devices (e.g.,heart valves or joint replacements), stable coatings which do not dissipate over time are needed to protect against DAI.[1] The race for the surface (**Chapter 1.1.3**) is especially important for percutaneous and permucosal, or totally internal implanted devices.

Chapter 2

Aim and motivation

The aim of the research conducted and described in this thesis is the design of an antibacterial surface by the combination of an active and a passive strategy. Antibiotic resistance is a continuously increasing threat to human health, as previously curable bacterial infections are again becoming life-threatening. Bacteria are able to rapidly adapt to new environments by the evolution of new mutations. Using less antibiotics is crucial to slow down the creation of antibiotic resistance. Therefore, research must be performed to develop strategies in which potent, available antibiotics can be reduced as much as possible. On the other hand new antibiotics to which bacteria are not yet resistant and strategies to fight bacteria in which bacteria are less prone to develop resistances need to developed.

The scope of this thesis addresses the concept of a new design for antibacterial surfaces by the combination of a passive strategy to reduce bacteria attachment and an active strategy to kill bacteria locally. To do this, self-assembled polymeric nanostructures serve as the basis for either the passive strategy by creating a nanostructured surface or the active part as micelles decorated with an antimicrobial peptide (AMP) or by designing an antibiotic producing nanoreactor. Anyhow, these polymeric nanostructures need to be immobilized to create a nanostructured surface or to serve as a local source of antibiotic activity. Research showed that AMPs create less resistances due to their mode of action and immobilized nanoreactors have the advantage to be able to locally produce antibiotic when needed. Therefore, they are believed to reduce the amount of antibiotics used, slowing down the creation of antibiotic resistance. These surfaces are designed with the final goal of using them as possible implant materials. Therefore, it is crucial to minimize toxic components to an absolute minimum during production to minimize possible contaminants in the final product.

The studies presented in this thesis aim to contribute to the future development and advancement of the vast and important research field of antimicrobial surfaces.

Chapter 3

Immobilization of polymersomes via SPAAC reaction and coimmobilization of self-assembled polymeric nanostructures

This chapter is based on published work entitled: Surfaces with Dual Functionality through Specific Coimmobilization of Self-Assembled Polymeric Nanostructures.[222]

3.1 Introduction

Chemo-selective copper catalysed azide alkyne click (CuAAC) reaction is a popular covalent immobilization technique. However, using this well-established reaction in biological samples, is limited by the cytotoxicity of Cu(I). The strain promoted Azide-Alkyne click (SPAAC) reaction, inspired by the CuAAC reaction, is another, simple one-pot reaction without the need of any catalysts due to the high strain (18 kcal/mol) of the reactive triple bond in an 8-membered ring.[220,221] Due to its high selectivity, rapid kinetics, and low toxicity, this bio-orthogonal copper-free click reaction attracted a lot of interest in different fields.[234–237] Accordingly, SPAAC reactions were successfully applied to post-functionalize various nanostructures like liposome membranes,[238,239] nanoparticles,[240] quantum dots,[241] or self-assembled polymersome membranes.[242] Various cyclooctynes with high ring strain were designed to increase the reactivity and apply SPAAC reactions in biological environments, *in vitro* as well as *in vivo*.[243,244] The bio-orthogonal SPAAC reaction is a promising precedure for immobilizing nanostructures on surfaces in order to engineer and to ultimately optimize surfaces for biomedical applications.

The thiol-ene click reaction can proceed via the radical or nucleophilic Michael addition.[245] With the radical addition, the thiol group might be added non-selectively to all types of vinyl groups. Besides the radical initiator, an external source of energy is needed to generate radicals. On the other hand, the nucleophilic Michael addition profits from mild reaction conditions between the thiol as the nucleophile and the double bond of an α,β-unsaturated carbonyl compound, an acryl moiety. Different amine or phosphine based catalysts activate and promote the Michael addition between thiols and acrylates (**Figure 3.1**).[245] The latter has been applied to create nanostructured surfaces through

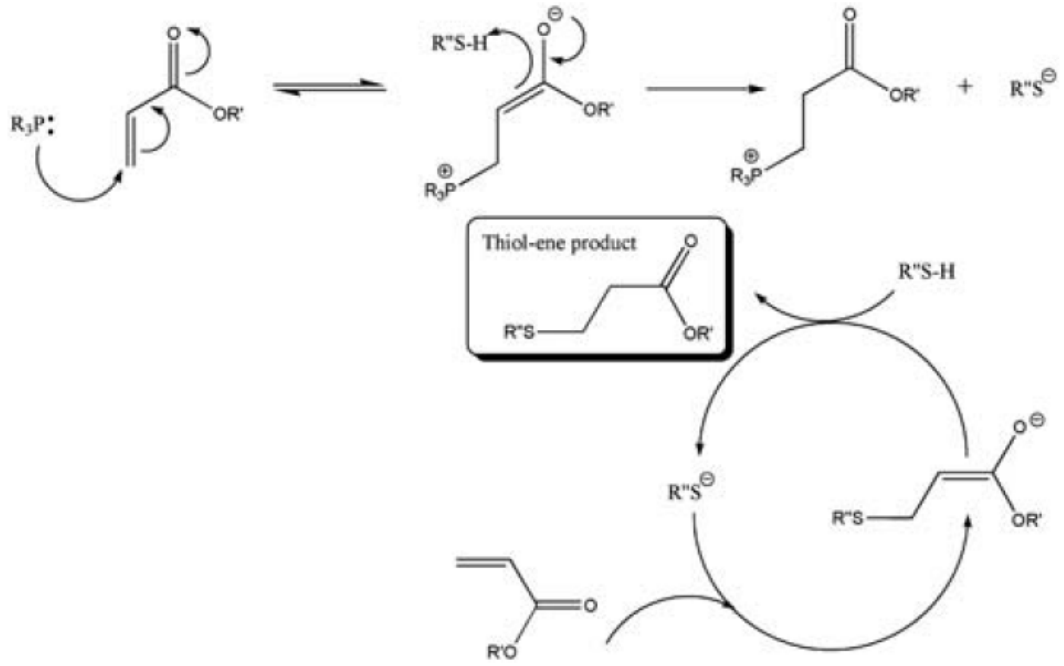

Figure 3.1: Proposed mechanism of the thiol-ene click reaction between an acryl group and a thiol moiety catalysed by a phosphine compound.[245]

the immobilization of methacrylate terminated PMOXA-*b*-PDMS-*b*-PMOXA based nanoassemblies. The architecture of the vesicles and micelles in solution stayed stable in the presence of tris(2-carboxyethyl)phosphine (TCEP), but changed when triethylamine, or propylamine was used.[218]

A number of soft lithography techniques can be used to immobilize vesicles in spatially defined patterns. For example, micro-molding in capillaries takes advantage of the capillary forces that are induced by pressing a micro-stamp on the surface which creates channel-like spaces between the surface and the stamp. Lipid vesicles were locally immobilized by adding a solution of vesicles in front of the stamp and subsequently, the capillary forces led to an influx of the solution into the defined space between the stamp and the surface.[215,246] Classical micro-contact printing (μCP) is another soft lithography technique that also uses a PDMS micro-stamp. However, here no connected pattern on the stamp are needed to create channels. Instead, the substrate to be immobilized is directly inked on the patterned side of the stamp and then brought in contact with the surface thereby transferring the pattern onto the surface of interest.[247] Corresponding solutions of nanostructures were directly inked on the PDMS stamps to immobilize liposomes,[246,248] inorganic nanoparticles,[249–251] or, as described in this chapter, polymersomes[222] in a defined pattern by μCP.

3.2 Scope of this chapter

The aim of the research presented in this chapter was to coimmobilize polymeric self-assembled nanostructures like polymersomes and micelles. These structures are known to provide protection for encapsulated biologically relevant molecules.[93] Coimmobilizing two distinct structures could allow the future design of new antimicrobial surfaces which are able to fight bacteria colonization with two active component protected by the polymeric nano-assemblies until further usage. The scope of this chapter addresses the study of a new immobilization technique which allows the immobilization of poylmersomes without the need of toxic additives. Furthermore, it is combined with an already known immobilization technique to study coimmobilization. This chapter aims to further advance the research and knowledge in the field of immobilizing self-assembled nanostructures and to achieve following goals:

(**i**) Preparation and characterization of polymersomes and micelles.

(**ii**) Optimizing a biocompatible immobilization technique.

(**iii**) Simultaneous coimmobilization of two distinct structures using two different immobilization techniques.

(**iv**) Immobilization of nanostructures creating a distinct pattern.

The approach developed in this chapter is based on the creation and careful characterization of surfaces with immobilized nanostructures. There is an interest to find new ways to immobilize and spatially control the immobilization of nanostructures to further develop and design new smart surfaces.

3.3 Experimental Procedures

3.3.1 Materials

$PMOXA_6$-*b*-$PDMS_{43}$-*b*-$PMOXA_6$ and azid terminated $PMOXA_7$-*b*-$PDMS_{40}$-*b*-$PMOXA_7$ were obtained by Dr. Samuel Lörcher;[82] Methacrylate-terminated $PMOXA_{25}$-*b*-$PDMS_{54}$-*b*-$PMOXA_{25}$ (Mn = 8400 g mol^{-1}) and $PMOXA_{19}$-*b*-$PDMS_{67}$-*b*$PMOXA_{19}$ (Mn = 8000 g mol^{-1}, Đ= 1.3) were purchased from Polymer Source Inc.; bodipy630/650, alexa fluor 488 azide, and Menzler glass coverslips (22 x 32 mm^2) from Thermo Scientific Inc.; silica wafers (P⟨100⟩) from Si-Mat Germany; the microstamp from Research Micro Stamps; (3-aminopropyl)triethoxysilane (APTES) from Acros organics; ethyltrimethoxysilane from Alfa Aesar; dicyclohexylcarbodiimide (DCC) and ethyl acetate from Fluka Analytical; 1-hydroxy-6-chloro-benzotriazole (6-Cl-HOBt) from Iris Biotech GmbH; sodium chloride (NaCl) and sodium phosphate dibasic (Na_2HPO_4) from Merck; potassium chloride (KCl) and potassium dihydrogen phosphate (KH_2PO_4) from PanReac AppliChem; dichloromethane (DCM) from VWR chemical; DBCO-Cy5, DBCO-acid, trimethylamine, toluene, ethanol, (3-mercaptopropyl)- trimethoxysilane, sodium hydroxide (NaOH), and tris(2-carboxyethyl)phosphine (TCEP) from Sigma-Aldrich. All chemicals were used as received unless stated otherwise.

3.3.2 Self-assembly

Five different triblock copolymers composed of poly(2-methyl-2-oxazoline) (PMOXA) and poly(dimethylsiloxane) (PDMS) were used in this study:

(**1**) $PMOXA_6$-*b*-$PDMS_{43}$-*b*-$PMOXA_6$ in combination with
(**2**) azide terminated $PMOXA_7$-*b*-$PDMS_{40}$-*b*-$PMOXA_7$.

(**3**) Methacrylate terminated $PMOXA_{25}$-*b*-$PDMS_{54}$-*b*-$PMOXA_{25}$ and
(**4**) methacrylate terminated $PMOXA_{19}$-*b*-$PDMS_{67}$-*b*$PMOXA_{19}$ in combination with
(**5**) sulforhodamine B (SRB) labeled $PMOXA_{18}$-*b*-$PDMS_{76}$-*b*-$PMOXA_{18}$.

Polymersomes containing 0.1, 1.0, and 10 mol% of azide terminated polymers were formed by thin film rehydration. A total of 0.5 μmol polymer were dissolved in 100 μl ethanol and dried into a film on a rotary evaporator. The polymer film was rehydrated with 1 mL PBS (137 mM NaCl, 2.7 mM KCl, 10 mM Na_2HPO_4, 1.8 mM KH_2PO_4, pH 7.4) and stirred overnight at room temperature (rt). The turbid solution was extruded 13 times through a 200 nm membrane (Nuclepore Trac-Etch membrane, Whatman®) using a 1 ml syringe extruder and purified by size exclusion chromatography (SEC) on a self-filled Sepharose 2B column (length: 25 cm, diameter: 1 cm) that was connected to an ÄKTAprime system for detecting the polymersome elution at 280 nm.

Polymersomes and micelles with methacrylate groups were formed by thin film rehydration in the dark.[218] To obtain approximatly 0.5 mol% SRB-labeled polymer, 1 μmol polymer was dissolved in 2 mL DCM (0.5 μmol ml^{-1}) and a drop (ca. 5 μl) of a 0.9 mM solution of SRB labeled polymer was added. The polymer solution was dried to a film prior to its rehydration with 2 mL PBS (pH 7.4) by stirring at rt over night.

3.3.3 Physical characterization of the nanostructures

Dynamic Light Scattering (DLS) was performed on a Zetasizer nano ZSP (Malvern Instruments) at 25°C. The scattering was recorded at a backscattering angle of 173°. 20 μL of polymersome solution was diluted in 500 μL PBS. Static light scattering (SLS) (LS instruments) was performed with a 30 mW HeNe laser at 23°C and target scattering intensity of 40 kHz. Nanostructures containing 1 mol% azide terminated polymers were diluted to solutions of 0.3, 0.2, and 0.1 mg mL^{-1} polymers (0.5 μmol ml^{-1} $\widehat{=}$ 2.25 mg mL^{-1}, dilution after purification: 3.4-fold). Each concentration was measured at scattering angles between 40° and 110° with an angular step of 10° for 20 s each. For the lowest concentration, DLS data was recorded on the same instrument at 90° for 60 s.

Transmission electron microscopy (TEM) images were recorded on a Phillips CM100 at an acceleration voltage of 80kV. 5 μL nanostructure solution diluted in PBS (1:7) were deposited on a glow discharged formvar and carbon coated copper grid. After 1 min adsorption, excess samples was blotted off, and the grids washed twice with 5 μL H_2O, once with 5 μL 2% uranyl acetate before being negatively stained with 5 μL 2% uranyl acetate for 10 s.

Fluorescent correlation spectroscopy (FCS) experiments (Zeiss LSM880) were performed with a Dibenzocyclooctyne (DBCO) labeled fluorophore, DBCO-Cy5 as the fluorescent dye and a HeNe laser (λ = 633 nm). A main beam splitter (MBS 488/561/633) was used. The pinhole diameter was set to 90 μm and calibrated using PBS containing 100 nM of

DBCO-Cy5. For each kind of polymersome with a different amount of azide groups, three independent polymersome preparations were stirred with DBCO-Cy5 overnight at 37°C at 100 rpm, and measured at 1% laser power. The amount of DBCO-Cy5 added was equal to the concentration of azide terminated block copolymer. For samples without azide terminated polymers, the same amount of DBCO-Cy5 was added as for the polymersome samples containing 1 mol% azide terminated polymers. Each measurement represents an average of 30 recordings of 10 s duration. The obtained autocorrelation curves were fitted by a 3-D diffusion model (**Equation 3.1**) either for a single-component, when analyzing the free dye, or for two-components when analyzing the polymersomes reacted with the dye, where the parameters for one component were constrained according to the recorded values of the free dye.[88]

$$G(\tau) = 1 + \frac{1}{N} * G_t * G_d \tag{3.1}$$

$$G_t(\tau) = 1 + \frac{T_t}{1 - T_t} * e^{-\frac{\tau}{\tau_t}} \tag{3.2}$$

$$G_d(\tau) = \sum_{i=1}^{n} \frac{\Phi_i}{(1 + (\frac{\tau}{\tau_{d,i}})^{\alpha_i}) * (1 + (\frac{\tau}{\tau_{d,i}})^{\alpha_i} * \frac{1}{S^2})} \tag{3.3}$$

Where N is the average number of particles in the confocal volume, $G_t(\tau)$ (**Equation 3.2**) describes the molecules in the triplet state, T_t represents the triplet fraction, and τ_t represents the triplet relaxation time. The term $G_d(\tau)$ (**Equation 3.3**) describes the diffusion of 1 component (n=1) or for two components (n=2) in three dimensions. Finally, τ_d represents the diffusion time, Φ the fractional intensities, S the structural parameter, and α the anomaly parameter. τ_t was fixed to 3 μs and S to 5. τ_d of DBCO-Cy5 was determined applying the one component system model to the measurements recorded of the free dye solution, the solution which was also used to calibrate the pinhole diameter. Then the average τ_d of the polymersomes interacting with the dye was determined using the two component system where the first component τ_d was fixed to the average of free DBCO-Cy5 (100.59 μs).

3.3.4 Preparation of functionalized substrates

The surfaces of silicon wafers or glass slides were activated by oxygen plasma (Plasma Cleaner, Harrick Plasma) for 5 min before being immersed in toluene (anhydrous, 25 mL) containing APTES (4.3 μL), ethyltrimethoxysilane (4.3 μL), and triethylamine (42 μL).[218] The surfaces were constantly shaken (80 rpm) overnight at rt. Subsequently, the surfaces were rinsed with toluene followed by ethanol and dried under a gentle stream of compressed air. Dried surfaces were further functionalized with DBCO as follows. 2 μmol of DBCO-acid, DCC, and 6-Cl-HOBt were separately dissolved in 1 mL ethyl acetate before being mixed together and stirred at 0°C for 1 h. The APTES functionalized surfaces were immersed in 20 mL ethyl acetate and the cooled reaction mixture was added. The surfaces were shaken horizontally at 80 rpm overnight at rt, to allow the peptide bond formation between the amine on the surface and the acid on the DBCO linker. Subsequently, the derivatized surfaces were rinsed with ethyl acetate, water, and ethanol, and then dried under a gentle stream of compressed air.

Bifunctionalized surfaces were prepared similarly. After plasma treatment, the glass slides

were immersed in a 0.4% (w/w) of silanes in toluene (1:1:1 weight% APTES, (3-Mercaptopropyl)trimethoxysilane, and ethyltrimethoxysilane) to achieve a 33% relative density of each silane. Subsequently, the surfaces were washed and the amine groups of the APTES served to further functionalize the surface with an acid-DBCO linker via peptide bond formation as described above, but with a reduced reaction time of 1.5 h in order to minimize any potential side reactions.

DBCO functionalized surfaces were characterized by various methods and compared to non-functionalized and amino (APTES) functionalized surfaces. Static water contact angles (KSV, instruments, CAM100 Version 2.1.1) were measured on at least 3 independently prepared surfaces. Attenuated total reflection – Fourier transformed infrared (ATR-FTIR) spectroscopy (Bruker Alpha, platinum-ATR) measurements consisting of 24 recorded scans were performed on the surfaces. DBCO-functionalized surfaces were immersed in 3.5 mL Alexafluor488-azide (900 nM in PBS) to react overnight at 37°C, 20 rpm. The surfaces were washed with PBS to remove uncoupled dye. The surfaces were visualized by confocal laser scanning microspcopy (CLSM) (Zeiss LSM510 META/ConfocoCor 2 FCS microscope) using an Argon2 ($\lambda = 488$ nm) laser and a water immersion objective (C-Apochromat 40x/1.2 W). The pinhole diameter was set to 70 μm and a main beam splitter (HFT488), a secondary beam splitter (NFT490) and a band pass filter (BP 505-550) where used throughout all experiments. All images were recorded with a detector gain fixed to 679. The brightness adjustments by ImageJ of all recorded images were treated identically.

3.3.5 Immobilization of self-assembled nanostructures

An aliquot of 10 mM bodipy in dimethylsulfoxid (DMSO) was diluted in water to obtain a 25 μM bodipy stock solution. The appropriate volume (end concentration 50 nM) was added to azide functionalized polymersomes in PBS. Bodipy interacts with the PDMS block of the membrane due to non-specific hydrophobic interactions and therefore allows the visualization of the vesicles. 400 μL of the bodipy-stained polymersome solution were added onto DBCO-functionalized surfaces of approximately 1 cm^2. The SPAAC immobilization reaction was allowed to proceed overnight at rt with horizontal shaking at 80 rpm. The surface was washed 3 times by immersion in 2 mL fresh PBS while shaking horizontally at 80 rpm for 5 min at rt.

To immobilize nanostructures on bifunctionalized surfaces, a bifunctional surface containing DBCO and thiol moieties as well as two different nanostructures were used. Bodipy (50 nM) was utilized to visualize the azide exposing polymersomes through hydrophobic interactions, while the methacrylate nanostructures were visualized by the addition of SRB labeled polymers during the self-assembly process.

A microstamp of parallel stripes (5 μm width, 5 μm spacing, 10 μm tall) was inked with a polymersome solution (azide or methacrylate exposing polymersomes) by spreading the solution with a Q-cotton tip on the stamp. The stamp was brought in contact with the bifunctionalized DBCO/thiol surface for 10 min and weighted with a glass petri dish lid (ca. 18 g). The stamp was removed and the surface was rinsed with PBS. The stamp was then washed by rinsing it with water, ethanol and sonication in ethanol for 10 min before reuse.

The SRB labeled methacrylate nanostructure (polymersome and micelle) solution obtained after self-assembly was diluted 1:1 with PBS. TCEP (20 mg mL^{-1}), the catalyst for the thiol-ene reaction was added at least 2 h prior to adjusting the pH to 7.0 with 2 M NaOH. Afterwards, this methacrylate nanostructure suspension was mixed 1:1 with bodipy containing, azide exposing polymersomes, and 400 μL of the mixture was applied to approximatly 1 cm^2 of the bi-functionalized surfaces. The immobilization reactions was allowed to proceed overnight while horizontally shaking at 80 rpm at rt. Afterwards the surfaces were washed by removing the reaction solution, followed by 3 immersions in 2 mL fresh PBS, while shaking horizontally at 80 rpm for 5 min at room temperature.

Atomic force microscopy (AFM) (JPK Nanowizard 3, Version 6.0.63) was used to characterize the surfaces of immobilized polymersomes containing varying ratios of azides. A Tap150 Al-G cantilever (Budget Sensors, resonance frequency 150 kHz, force constant 5 N m^{-1}) was used for AC mode measurements in PBS buffer. Images were analyzed with the JPK data processing software (Version spm_6.0.63). For further characterization, platinum-sputtered surfaces were examined by scanning electron microscopy (SEM) (Hitach S-4800) with an acceleration voltage of 5000 V at a working distance of 3.4 mm.

CLSM (Zeiss LSM880) was performed to visualize immobilized nanostructures. The bodipy containing azide-polymersomes and the SRB labeled methacrylate polymersomes and micelles were visualized after immobilization by CLSM in the airyscan mode. A HeNe laser (λ = 633 nm) was used to visualize bodipy containing vesicles, and a DBSS 561-10 Laser (λ = 561 nm) for SRB labeled nanostructures. The images were recorded with an oil immersion objective (Plan Apochromat 63x/1.4 oil DIC M27), a mean beam splitter (MBS 488/561/633) and an airyscan detector. The laser power was kept as low as possible (0.2% for λ = 561 nm, 2 – 20% for λ = 633 nm) to minimize bleaching, the gain was always below 800, and the pinhole diameter around 110 nm to be slightly above the minimal pinhole diameter for airyscan, which corresponds to 2.5 airy units and 2.7 airy units for λ = 633 nm and λ = 561 nm, respectively. The images were airyscan processed with the Zeiss software ZEN 2.3 SP1 and imageJ software for brightness adjustments.

3.4 Results and Discussion

3.4.1 Self-assembly of PDMS-*b*-PMOXA-*b*-PDMS with different ratios of azide terminated polymers

Nanostructures equipped with either azide or methacrylate funcional groups were created by self-assembly of PDMS-*b*-PMOXA-*b*-PDMS via thin film rehydration. In order to expose different concentrations of azide groups on the surface, the nanostructures were self-assembled from mixtures of $PMOXA_6$-*b*-$PDMS_{43}$-*b*-$PMOXA_6$ copolymers and azide-terminated $PMOXA_7$-*b*-$PDMS_{40}$-*b*-$PMOXA_7$ copolymers at different ratios (0.0, 0.1, 1.0, and 10 mol%). Extrusion and size exclusion chromatography were applied to obtain a narrow, specific size distribution of the resulting assemblies (**Figure 3.2**).

The assemblies prepared with increasing percentages of azide terminated block-copolymer were characterized by a combination of light scattering (LS), specifically DLS and SLS, and TEM. DLS measurements of all azide containing assemblies revealed an overall average diameter of 140 ± 15 nm according to the number particle size distribution (PSD) and

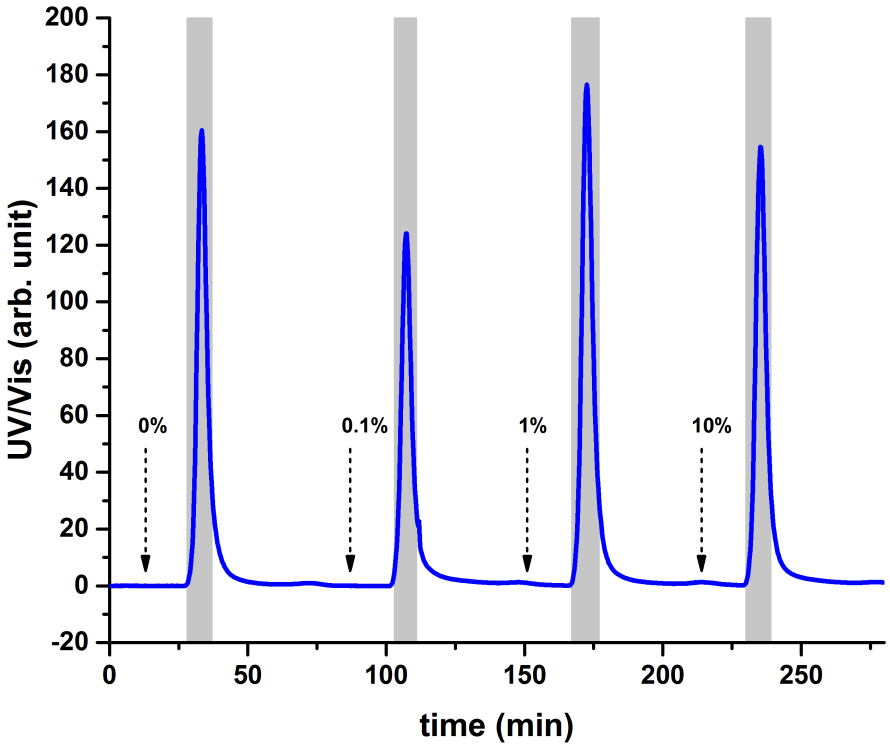

Figure 3.2: Size exclusion chromatograms (UV-vis absorption at 280 nm) of polymersomes prepared from polymer mixtures with 0.0, 0.1, 1.0, and 10 mol% of azide-functionalized polymer. Injection volumes were 880, 850, 860, and 860 μL, respectively. Arrows indicate the time point of injection. The polymersomes were eluted in PBS and collected as a single fraction indicated by the grey shading.

polydispersity indices (PDI) ranging from 0.03 to 0.23. Diameters that are all in a similar range indicate that the different ratios of azide derivatized polymers in the polymer mix did not affect the size of the resulting nanostructure. (**Figure 3.3**).

Therefore, for further characterization of the nanostructure architecture, only the assembly containing 1 mol% azide-terminated block-copolymer was considered. Specifically, the shape factor was calculated according to **Equation 1.4**: a hydrodynamic radius (R_h) of 84 $\pm$ 7 nm and a radius of gyration (R_g) of 76 $\pm$ 1 nm was obtained (**Figure 3.4**). The resulting shape factor (ρ=R_g/R_h) of 0.9 indicated a hollow, spherical architecture.[140] Consistently, TEM micrographs of the different assemblies revealed a morphology that is characteristic of hollow spherical structures, independent of the amount of azide-terminated block-copolymer (**Figure 3.5**).

3.4.2 Self-assembly of methacrylate terminated polymers

In order to promote the formation of nanostructures that expose fluorescently labeled methacrylate, two different methacrylate terminated PMOXA-*b*-PDMS-*b*-PMOXA copoly-

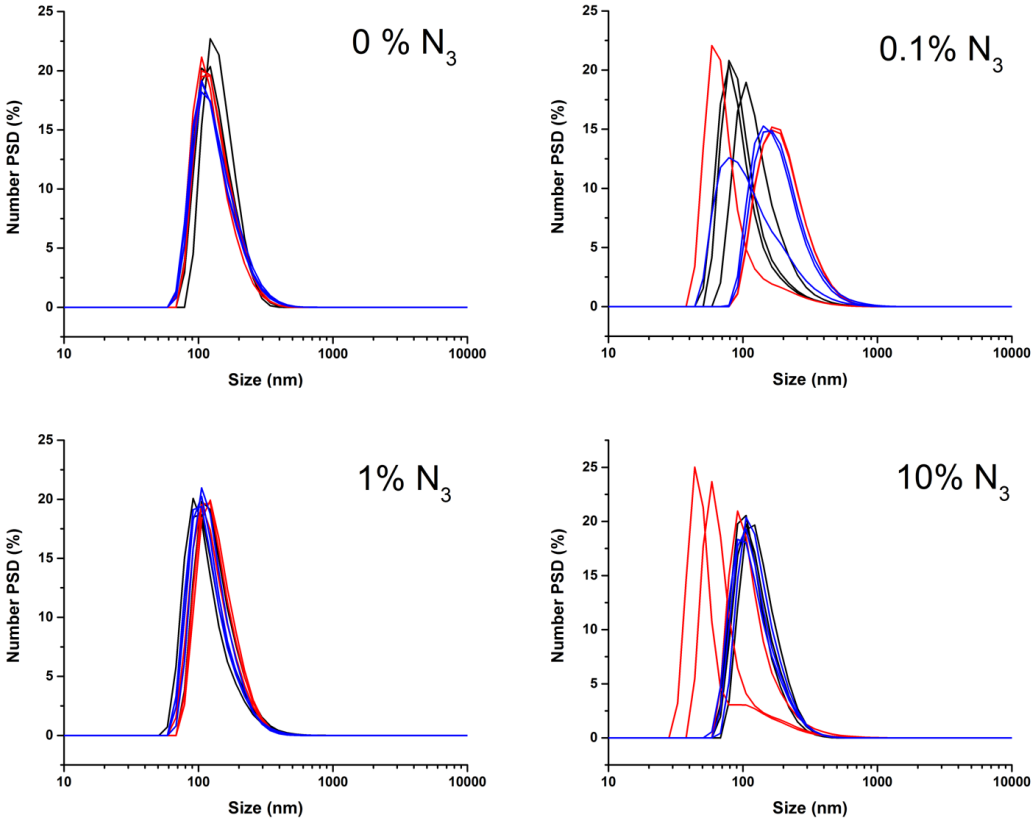

Figure 3.3: DLS of polymersomes with different ratios of azide terminated polymers revealed similar diameters for the number average PSD. Three independent samples per type of polymersomes were measured three times each (black, red, and blue curves).

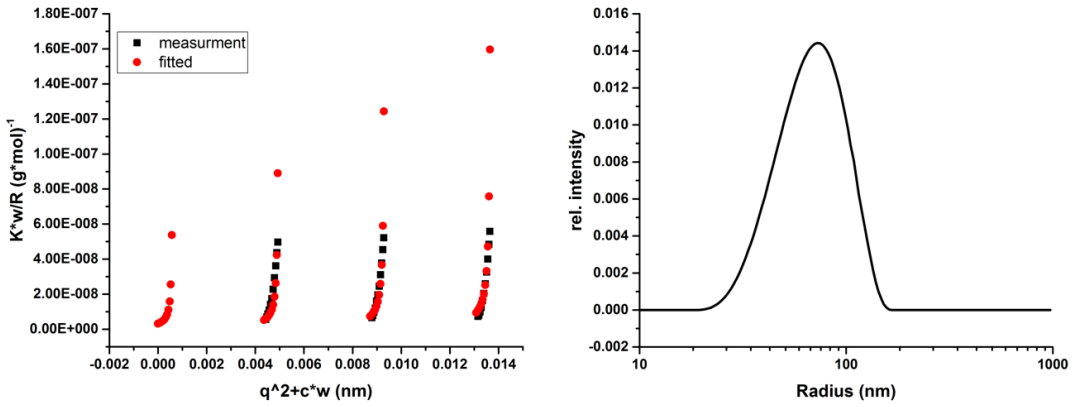

Figure 3.4: LS data of self-assembled structures containing 1 mol% azide terminated polymers. Previously extruded polymersomes were diluted with filtered PBS (Millex-LCR syringe filters, hydrophilic, polytetrafluoroethylene - PTFE, 0.45 μm; Millipore) to a final polymer concentration of; 0.3, 0.2, and 0.1 mg mL^{-1}. Left: Zimm Plot of SLS data acquired every 10° from 40° to 110°. Right: DLS measurement of the 0.1 mg ml^{-1} solution recorded at 90°

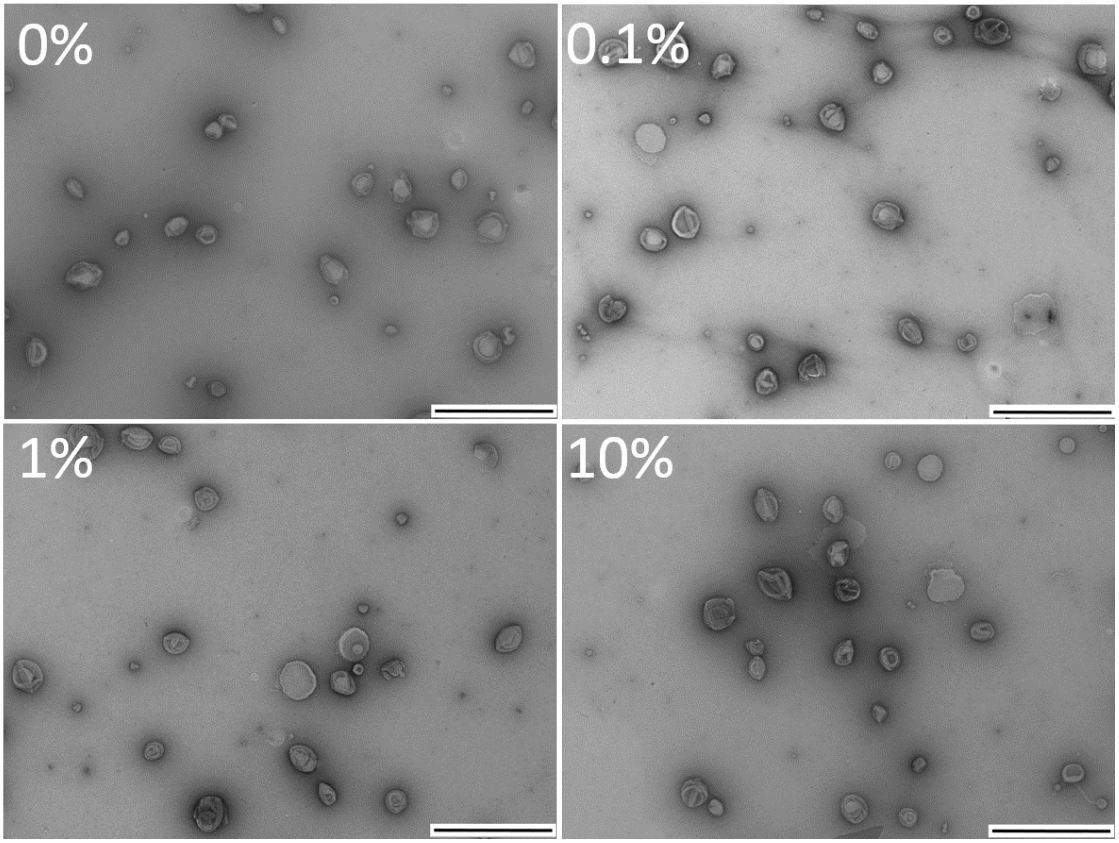

Figure 3.5: TEM images of polymersomes self-assembled from $PMOXA_6$-*b*-$PDMS_{43}$-*b*-$PMOXA_6$ with different ratios of azide-terminated polymers. Scale bars: 1 μm.

mers ($PMOXA_{19}$-*b*-$PDMS_{67}$-*b*-$PMOXA_{19}$ to form polymersomes, or $PMOXA_{25}$-*b*-$PDMS_{54}$-*b*-$PMOXA_{25}$ to form micelles)[218] were mixed with traces of SRB labeled $PMOXA_{18}$-*b*-$PDMS_{76}$-*b*-$PMOXA_{18}$.

The full characterization of the methacrylate functionalized polymers and the assemblies formed can be found in reference.[218] Methacrylate terminated $PMOXA_{19}$-*b*-$PDMS_{67}$-*b*-$PMOXA_{19}$ copolymers self-assembled into polymersomes with a diameter of 180 ± 95 nm by number PSD (**Figure 3.6A**) which is slightly larger than the size of azide functionalized polymersomes, and a PDI of 0.32 to 0.51 as determined by DLS. The higher PDI is in agreement with the respective TEM analysis, which revealed spherical morphologies of different sizes (**Figure 3.7A**). The presence of the shoulder indicated the presence of some bigger particles or aggregates. Micelles formed by methacrylate terminated. $PMOXA_{25}$-*b*-$PDMS_{54}$-*b*-$PMOXA_{25}$ copolymers appeared as round structures in TEM micrographs (**Figure 3.7B**) with a diameter of 80 ± 50 nm obtained by number PSD (**Figure 3.6B**) (maximal PDI 0.43). Methacrylate terminated nanostructures could not be purified by SEC due to interactions with the chromatography resin. Hence, they were examined without SEC, which explains the higher PDI compared to that of polymersomes assembled from azide terminated polymer.

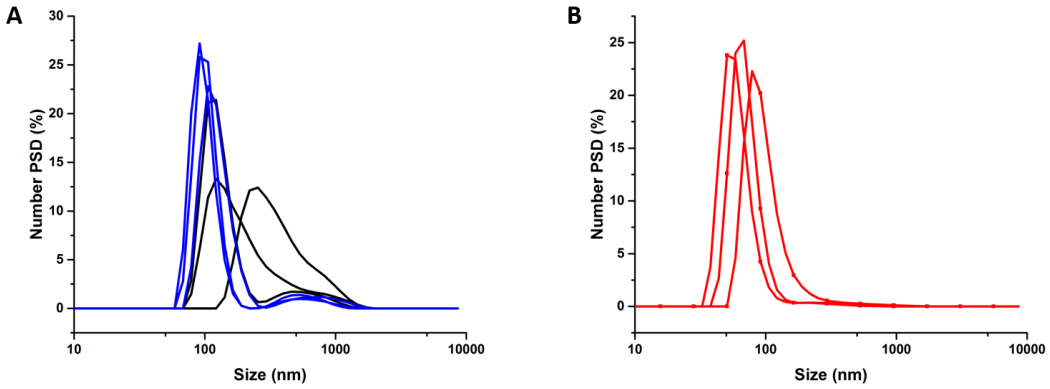

Figure 3.6: DLS measurements of A) two identically prepared methacrylate polymersome samples (black and blue traces), which were self-assembled from methacrylate terminated $PMOXA_{19}$-*b*-$PDMS_{67}$-*b*-$PMOXA_{19}$ block copolymer. The plot shows the number average PSD versus size for each measurement. Each sample was measured 3 times. B) methacrylate micelles self-assembled from $PMOXA_{25}$-*b*-$PDMS_{54}$-*b*-$PMOXA_{25}$. The number average PSD of three measurements are displayed.

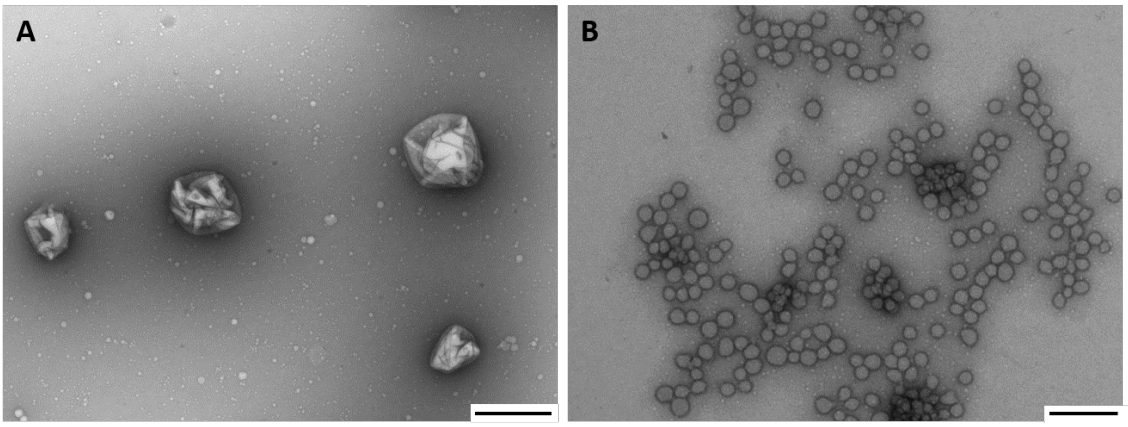

Figure 3.7: TEM images of A) polymersomes self-assembled from methacrylate terminated $PMOXA_{19}$-*b*-$PDMS_{67}$-*b*-$PMOXA_{19}$ block copolymer, scale bar: 500 nm, and B) micelles self-assembled from methacrylate terminated $PMOXA_{25}$-*b*-$PDMS_{54}$-*b*-$PMOXA_{25}$, scale bar: 200 nm.

3.4.3 Azide accessibility on polymersomes

Accessibility of the azide moieties exposed on polymersomes was assessed by FCS, which allows the study of the diffusion time of fluorescent molecules and their interactions with bigger assemblies, such as nanoparticles, liposomes, or polymersomes.[88,93,252] Fluorescently labeled DBCO (DBCO-Cy5) was reacted with azide functionalized polymersomes. The diffusion time (τ_d), was then determined by a two component fit where the first component's diffusion time was fixed to the one obtained for free DBCO and compared to free DBCO-Cy5 in solution determined by the one component fit (**Figure 3.8** and **Table 3.1**). The increase of two orders of magnitude in τ_d confirms that the DBCO-Cy5 molecule

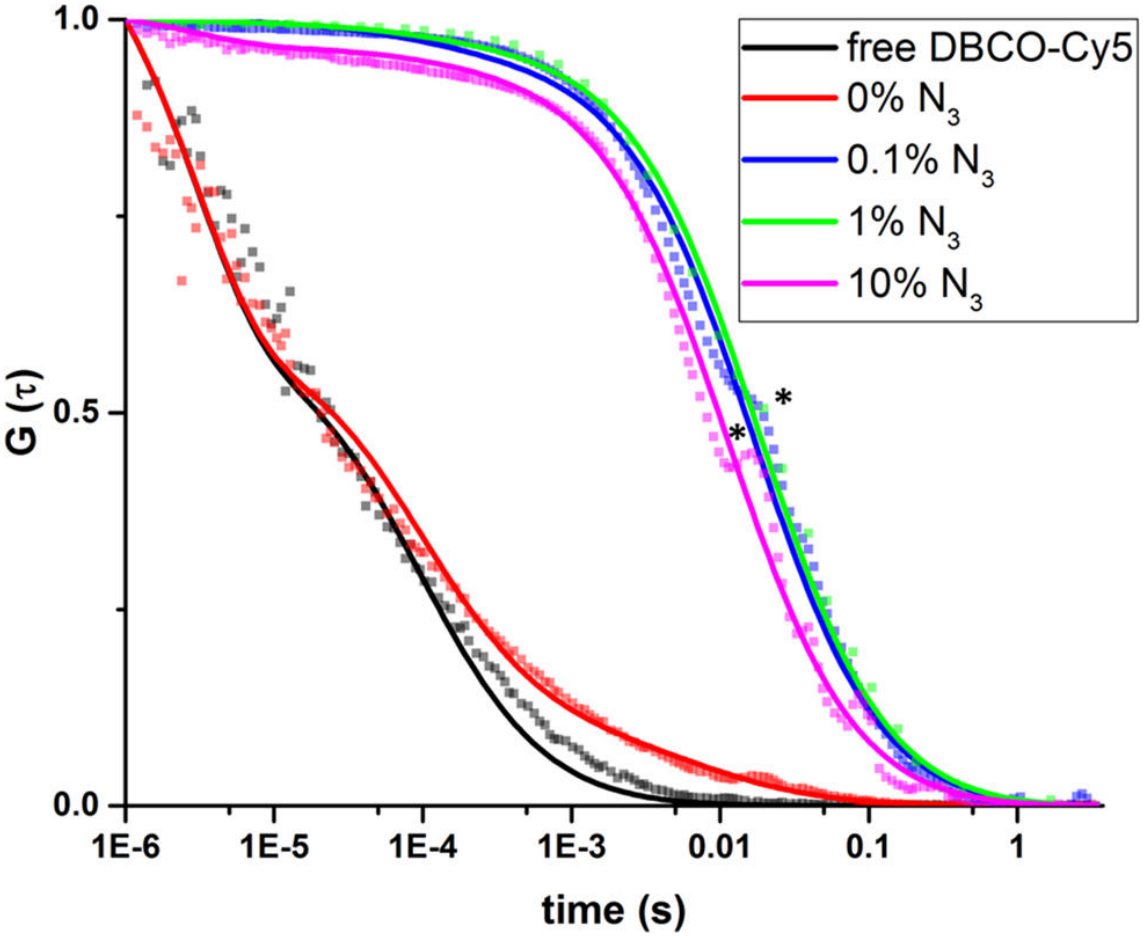

Figure 3.8: FCS measurements of DBCO-Cy5 interaction with polymersomes containing different amounts of azide-terminated polymers. DBCO-Cy5 was added to the outside of the polymersomes and after overnight reaction the normalized autocorrelation curves for azide containing polymersomes showed a strong shift to higher diffusion times compared to azide free polymersomes (red line) or free DBCO-Cy5 (black line).The samll step ($\star$) in the autocorrelation curve is indicative of the presence of some clusters of polymersomes.

was bound to the azide-exposing polymersomes, which diffuse significantly slower through the confocal volume than the free fluorescent molecules. Additionally, the R_h calculated through the diffusion time is in accordance with the expected size of the polymerosomes (**Table 3.1**). The calculated sizes are all in a similar range, however the FCS measurements seem to clearly indicate that polymersomes with 1 mol% azide terminated polymers

are bigger than the ones with 1 mol% azide terminated polymers. This might be due to some in-homogeneity of the sample as also some clusters of polymersomes are present, indicated by the small step in the autocorrelation curve (noted by $\star$). Polymersomes without azide groups were reacted with the same amount of DBCO-Cy5 as used for the polymersomes containing 1 mol% azide terminated polymers and a similar autocorrelation curve as the free dye was observed (**Figure 3.8**). The fit of this autocorrelation curve resulted in a 73% population of free DBCO-Cy5 and a 27% fraction of slow diffusing particles, which has been associated to a fraction of DBCO-Cy5 non-specifically interacting with unfunctionalized polymersomes, probably due to hydrophobic interactions with the polymeric membrane. The measured $\tau_d \approx 10'000$ μs, corresponding to a calculated R_h of 54 $\pm$ 7 nm is smaller than for the azide containing polymersome samples. However, in the case of azide exposing polymersomes, the slow diffusion fractions were close to 100%, whereas here the slow diffusion fraction accounted only for about one third. The significant increase of the slow diffusing fraction in azide containing polymersomes confirms an efficient bonding indicating that the azide groups were accessible on the polymersome surface. (**Table 3.1**).

	Free DBCO-Cy5	$PMOXA_6$-*b*-$PDMS_{43}$-*b*-$PMOXA_6$ polymersomes formed with x% azide-terminated $PMOXA_7$-*b*-$PDMS_{40}$-*b*-$PMOXA_7$			
		0.0%	0.1%	1%	10%
diffusion time [μs]	100 $\pm$ 4	9390 $\pm$ 1200	17630 $\pm$ 1050	21920 $\pm$ 3830	12580 $\pm$ 3410
Polymersome fraction [%]	N/A	27 $\pm$ 9	95 $\pm$ 1	95 $\pm$3	87 $\pm$9
R_h [nm]		54 $\pm$ 7	101 $\pm$ 6	126 $\pm$ 22	72 $\pm$ 20

Table 3.1: FCS parameters for each ratio of azide containing polymersomes.

3.4.4 Surface functionalization

To immobilize azide containing polymersomes through the SPAAC reaction, surfaces were functionalized with DBCO in a two-step procedure (**Figure 3.9**). First, surfaces were functionalized with primary amines using silane chemistry. A 50% relative density of amines on the surface was achieved by mixing the functional amine silane APTES and non-functional ethyl silane prior to the reaction with the surface.[218] Secondly, DBCO functional groups were introduced via a peptide bond formation using a carboxylic acid-functionalized DBCO.

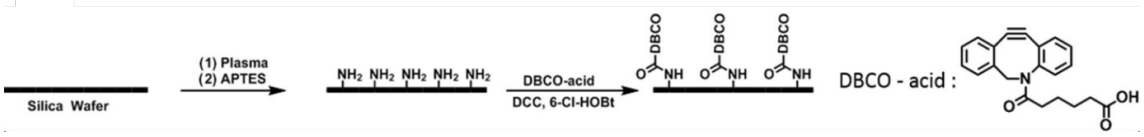

Figure 3.9: Schematic presentation of surface modification steps to obtain DBCO-functionalized surfaces.

To evaluate the functionalization of the surfaces we analyzed the changes in surface hy-

drophobicity and ATR-FTIR spectroscopy. Amine modified surfaces possess an increased hydrophobicity ($87 \pm 2°$) compared to non-functionalized surfaces ($67 \pm 1°$). Further functionalization with DBCO ($86 \pm 1°$) did not affect the hydrophobicity (**Figure 3.10A**).

ATR-FTIR spectroscopy was performed after each functionalization step. A non-functionalized silicon wafer was used as background. DBCO functionalized surfaces show an inverted peak around 2200 cm^{-1} indicating the presence of the triple-bond[253] compared with the non-functionalized or amine functionalized surface (**Figure 3.10B**).

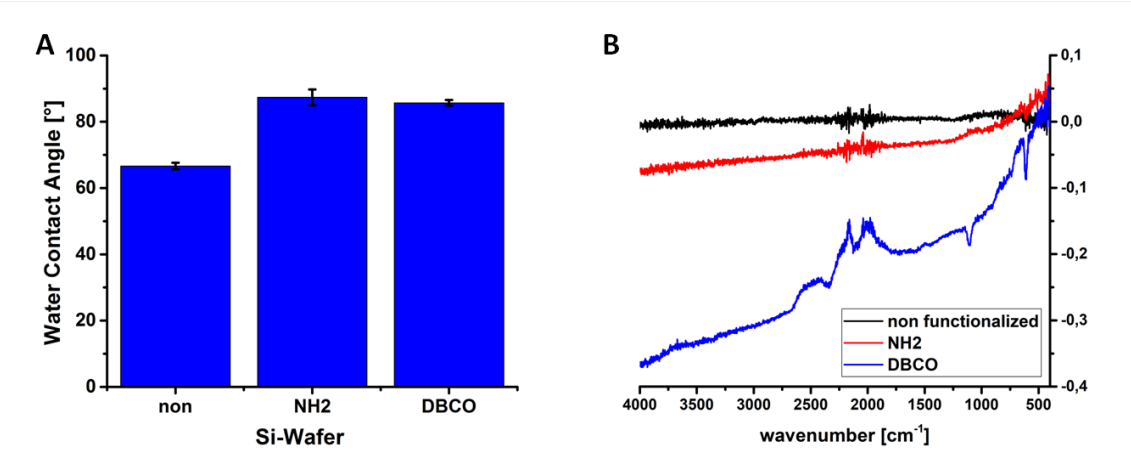

Figure 3.10: A) Water contact angles of non- functionalized (non), amino functionalized (NH_2) and DBCO functionalized surfaces. C) ATR-IR of non- functionalized (non), amino functionalized (NH_2) and DBCO functionalized surfaces.

Importantly, only surfaces functionalized with DBCO showed fluorescence after reaction with an azide functionalized fluorescent dye (**Figure 3.11**). Therefore, the surfaces were successfully functionalized with DBCO, rendering them reactive towards azide containing molecules.

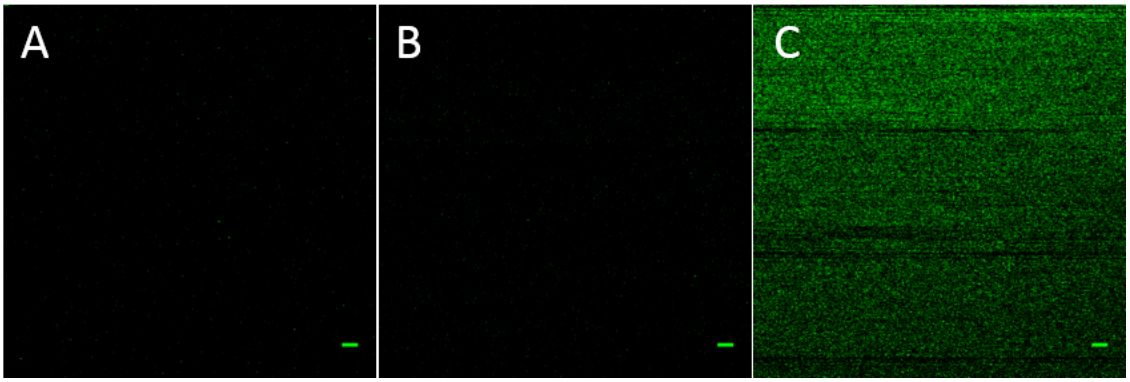

Figure 3.11: LSM micrographs after reacting the surface during the different functionalization steps with Alexafluor488-azide: non-functionalized surface (A), NH_2 functionalized surface (B), DBCO functionalized surface (C). Images were recorded with the same settings and processed equally. Scale bars: 10 μm.

3.4.5 Immobilization of azide-functionalized polymersomes on surfaces

The SPAAC reaction was conducted to immobilize the azide exposing polymersomes to the DBCO functionalized surface. The obtained surfaces after polymersome immobilization were characterized by a combination of CLSM, SEM, and AFM. A hydrophobic fluorescent dye (Bodipy630/650) was entrapped inside the polymersomes to allow their detection by CLSM. Numerous round fluorescent objects were observed in the expected size range confirming the immobilization of fluorescent structures and indicating successful polymersome immobilization on solid support by SPAAC (**Figure 3.12**).

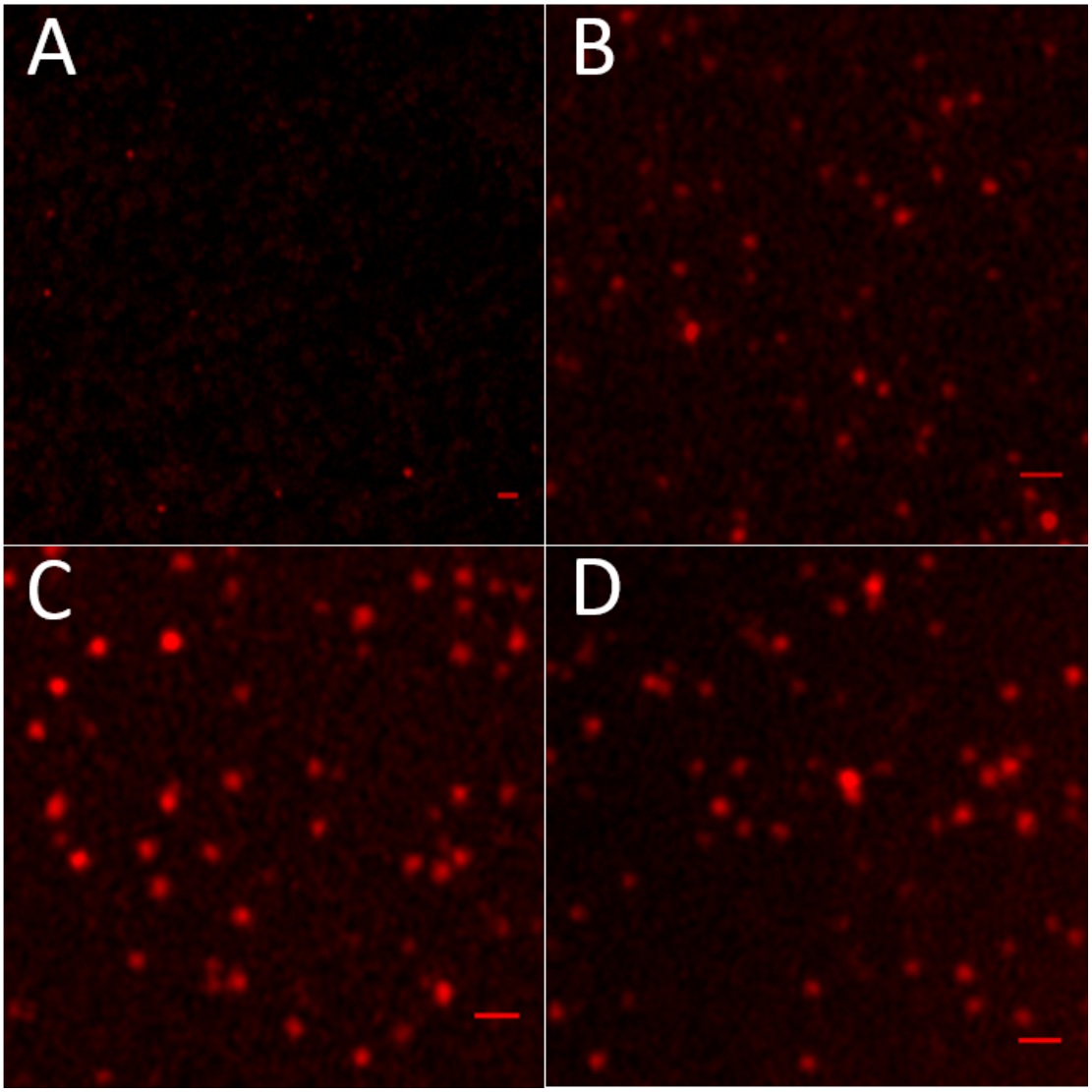

Figure 3.12: CLSM of immobilized polymersomes with different ratios of azide-terminated polymers: A) 0 mol%, B) 0.1 mol%, C) 1 mol%, and D) 10 mol% on DBCO-functionalized surfaces. Scale bar: 1 μm

A clear difference in immobilization density was detected between the azide-free (0 mol%) polymersome where only one polymersome per 100 μm^2 was found, compared to the azide-

exposing polymersomes (0.1, 1.0 , or 10 mol%) where 20-40 polymersome per 100 μm^2 were visualized. The polymersomes were counted using particle count on Fiji. However, no significant difference between the polymersomes containing 0.1, 1.0, or 10 mol% azide terminated polymers was observed (**Table 3.2**).

Azide ratio	0 mol%	0.1 mol%	1 mol%	10 mol%
Polymersomes (= red dots) per 100 μm^2	1.6	40.7	4.4	31.3
	1.2	33.5	5.3	23.6
	1.2	43.5	9.4	26.3
	0.9	36.8	37.0	6.1
	2.7	46.8	44.1	13.9
Average ± standard deviation	1.5 ± 0.6	40.3 ± 4.7	20.0 ±17	20.2 ±9.1

Table 3.2: Polymersomes were mixed with Bodipy prior immobilization to be able to visualize them on the surface by airyscan LSM as red dots. Several images of each kind of immobilized polymersomes were taken. The round fluorescent dots were counted by analyze particles on Fiji by ImageJ. The size of the image was calculated to put in relation with the immobilized polymersomes.

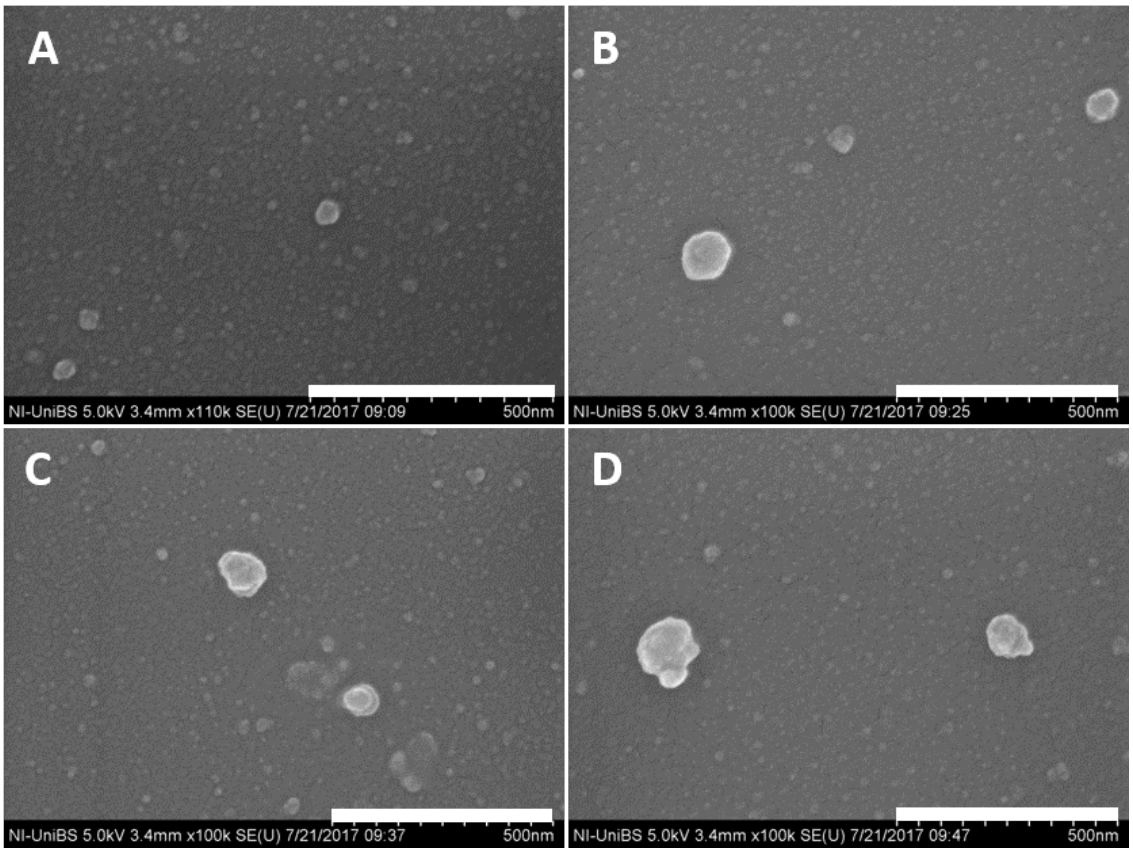

Figure 3.13: SEM of immobilized polymersomes with different ratios of azide-terminated polymers: A) 0 mol%, B) 0.1 mol%, C) 1 mol%, and D) 10 mol%, Scale bar: 500 nm

The images obtained by SEM (**Figure 3.13**), are in agreement with the CLSM micrographs, and provide further evidence of the immobilization of azide containing polymersomes on solid support.

In addition, surfaces reacted with azide containing polymersomes showed round structures on the surface of 70 – 120 nm in height when imaged by AFM while immersed in PBS buffer (**Figure 3.14**), supporting the previously obtained findings.

Reaction with azide-free polymersomes and the DBCO functionalized surface only revealed very few fluorescent dots by CLSM (**Figure 3.12A** and **Table 3.2**), few immobilized vesicles by SEM (**Figure 3.13A**) and no structures of the expected heights by AFM (**Figure 3.14A**). Together, this data strongly suggests that the immobilization was due to the azide functional groups on the polymersome exterior. Therefore, polymersomes exposing azides on their surface have been successfully immobilized by SPAAC reaction on DBCO functionalized silica wafers.

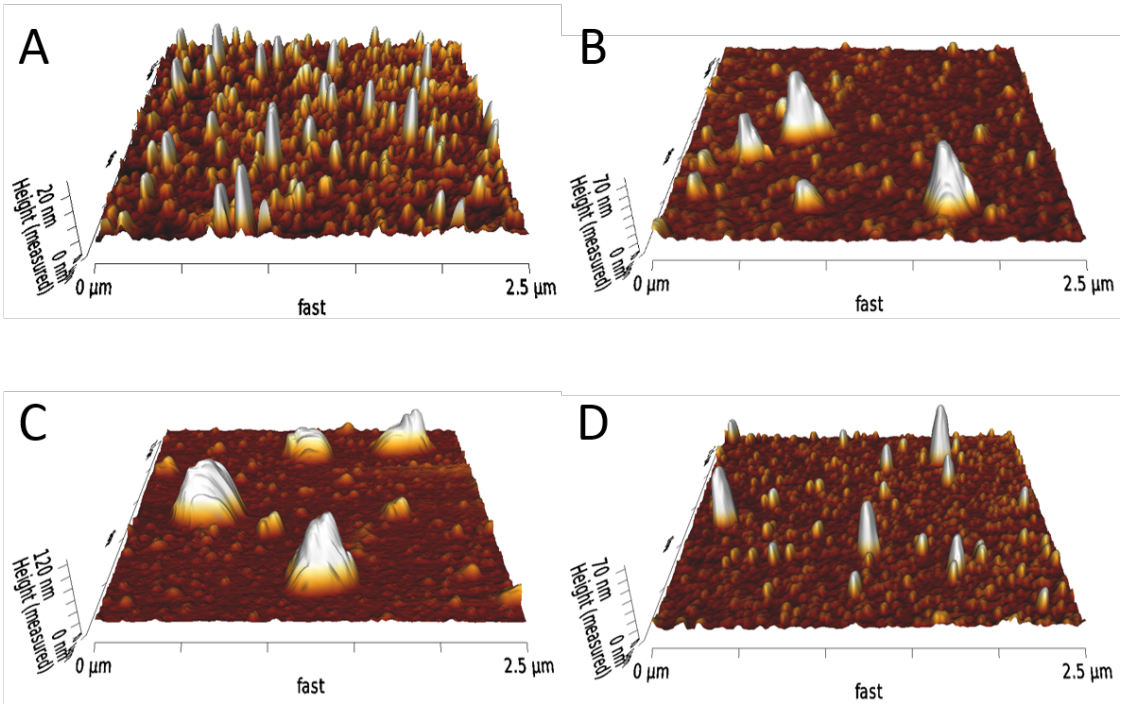

Figure 3.14: AFM of immobilized polymersomes with different ratios of azide-terminated polymers: A) 0 mol%, B) 0.1 mol%, C) 1 mol%, and D) 10 mol% on DBCO-functionalized surfaces. Scan size was 2.5 μm x 2.5 μm each and the height scale bars were 70 nm (A), 120 nm (B), 70 nm (C) and 20 nm (D), respectively.

3.4.6 μCP of polymersomes to obtain patterned surfaces

In order to equip surfaces with different functionalities, it is attractive to create patterns of one of the functionality of interest. Hence, μCP was used to immobilize self-assembled nanostructures. Polymersomes exposing azide groups and containing bodipy entrapped in their membrane were used as ink on the PDMS microstamp, transferred to the with DBCO

and thiols bifunctionalized surface, and visualized by CLSM. A clear striped pattern alternating between fluorescence and background every 5 μm was observed (**Figure 3.15A**), indicating successful surface patterning. Further, the distinct fluorescent spots observed in the patterned lines indicate that the polymersomes remained intact throughout the printing process and were transferred from the stamp to the surface. Similarly, polymersomes exposing methacrylate groups and labeled with SRB were successfully micro-contact printed onto the surface (**Figure 3.15B**). The methacrylate exposing nanostructures covalently bind to the thiol moieties on the surface through the thiol-ene reaction using TCEP as a phosphine catalyst (**Figure 3.1**).[218] Our results further underline that also PDMS-based nanostructures can be printed from a PDMS based stamp onto a functionalized surface.

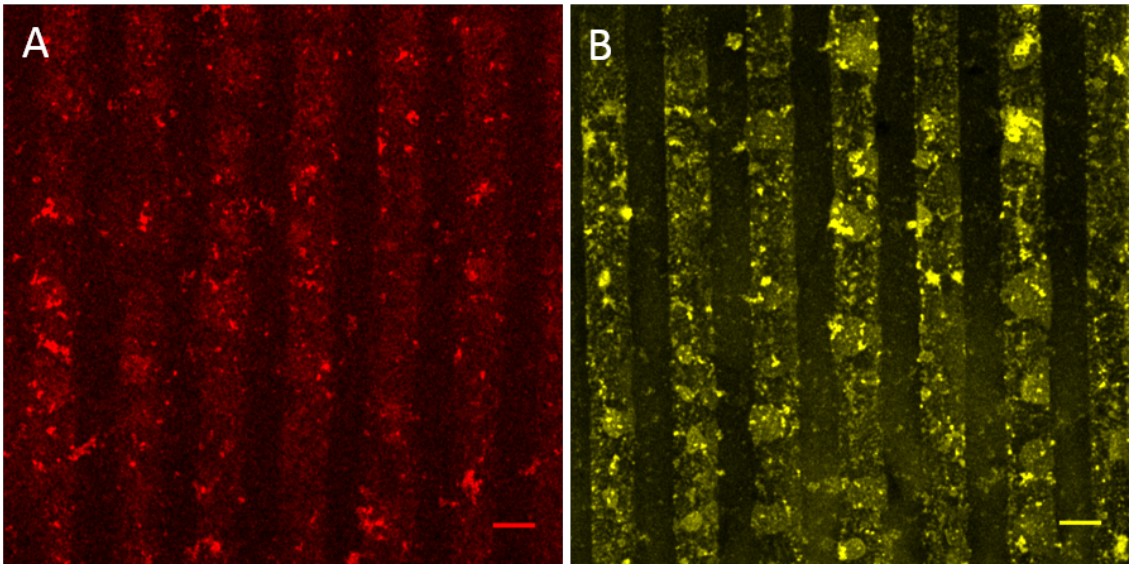

Figure 3.15: Polymersomes are immobilized within a pattern by μCP and visualized by CLSM: A) Azide functionalized polymersomes visualized through entrapped fluoresencent dye (bodipy, red) and B) SRB (yellow) labeled methacrylate functionalized polymersomes. Scale bars: 5 μm.

3.4.7 Coimmobilization of two different structures

In order to obtain multifunctional surfaces we were interested to coimmobilize different types of nanostructures with different functional groups on the same solid support. Surfaces were functionalized with both, thiols, to perform the thiol-ene reaction with methacrylate nanostructures,[218] and DBCO, to perform the SPAAC reaction with azide containing polymersomes. Therefore, plasma activated silica wafers were reacted simultaneously to thiol and amine containing silanes prior to the condensation reaction between the amine and the DBCO-acid. In order to avoid any unwanted side reactions between thiols and alkynes, the condensation reaction time was reduced to 1.5 h. The immobilization of the azide containing polymersomes was visualized through bodipy (red) interacting with the membrane while the immobilization of the methacrylate nanostructures was visualized by SRB (yellow). Traces of SRB labeled polymer was mixed with methacrylate terminated polymer during self-assembly to obtain fluorescent nanostructures. A mixture of the two

differently functionalized polymersomes was added on the bifunctionalized surface. However, prior mixing the two nanostructures, the SRB labeled methacrylate nanostructures were reacted to TCEP while the azide exposing polymersomes were separately mixed with bodipy.

CLSM micrographs showed successful coimmobilization of the polymersomes due to the presence of both fluorescent signals associated to SRB in the methacrylate polymersomes and bodipy in the azide exposing polymersomes. (**Figure 3.16A**). To go one step further in obtaining nanostructured bifunctional surfaces we simultaneously immobilized two different assemblies: azide-exposing polymersomes (containing bodipy) and methacrylate-exposing micelles labeled with SRB. Azide exposing polymersomes containing bodipy were mixed equally with SRB labeled micelles exposing methacrylate groups and added on the bifunctionalized surface. After overnight reaction, the immobilized structures, visible as round fluorescent dots for the polymersomes and micelles were observed by CLSM (**Figure 3.16B**). Furthermore, bodipy-stained, azide-exposing polymersomes were microcontact printed onto a bifunctionalized surface followed by a second μCP immobilization of SRB-labeled methacrylate-exposing micelles with the stamp rotated 90° to create a checkerboard pattern (**Figure 3.16C**). After patterning single nanoassemblies, it was shown that different nanoassemblies could be not only randomly coimmobilized on the same surface, but also in a distinct pattern.

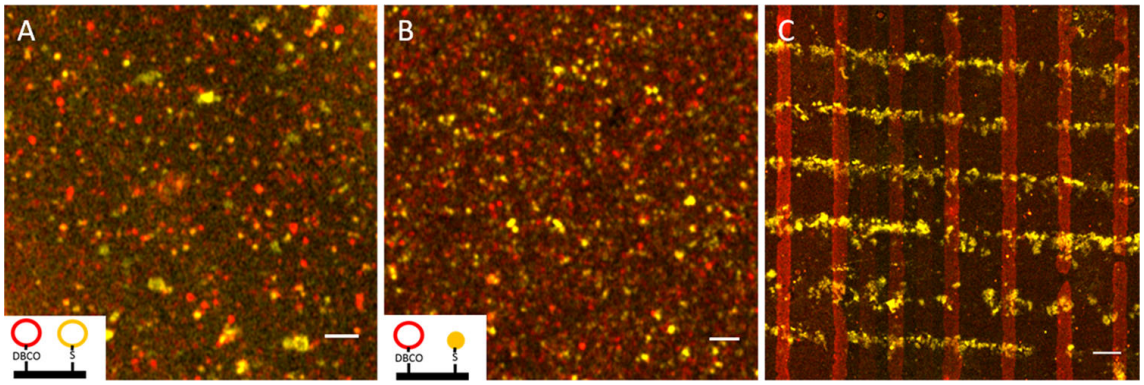

Figure 3.16: CLSM micrographs of azide-functionalized polymersomes containing bodipy (red dots) coimmobilized with SRB-labeled methacrylatefunctionalized nanostructures (yellow dots) on DBCO and thiol bifunctionalized surfaces. (A) Coimmobilization of azide-exposing polymersomes and methacrylate-exposing polymersomes; (B) azide-exposing polymersomes and methacrylate-exposing micelles; and (C) checkerboard pattern obtained by first printing azide-exposing polymersomes and then methacrylate-exposing micelles with the stamp rotated by 90°. Scale bars: (A, B) 2 μm; (C) 5 μm. *Hollow structure in the inset represents polymersomes and filled structures micelles.

3.5 Conclusions

Surfaces with nanostructured architecture and bifunctionality were successfully generated by the coimmobilization of azide containing polymersomes together with methacrylate exposing polymersomes or micelles on a solid support. To support simultaneous immobilization of the nano-assemblies, surfaces were bi-functionalized by using SPAAC and

thiol-ene reactions, each of them serving to specifically bind nano-assemblies exposing appropriate functional groups (azide and methacrylate, respectively). The SPAAC reaction was analyzed in detail as it was used for the first time to immobilize polymeric nanostructures, while the thiol-ene immobilization reaction has been used in conditions already reported.[218] A comparison between polymersomes containing different ratios of azide terminated polymers (0.1 - 10 mol%) revealed that the ratio does not influence the polymersome immobilization, suggesting that only a few attachment points are required for their successful immobilization via the SPAAC reaction. Additionally, μCP was applied to immobilize polymersomes in a spatially defined pattern onto surfaces. Coimmobilization of different functionalized nano-assemblies to engineer multifunctional surfaces represents a general approach to induce a nanostructured architecture on a solid support and a dual functionality through the active compounds that can be entrapped inside these nano-assemblies. Indeed, different cargos (as shown here by using dyes as models for biologically active low weight molecules) can be protected either in micelles or polymersomes. Such nanostructured surfaces with dual functionality are expected to improve the surface efficacy in applications, such as antimicrobial surfaces, or biosensing.

Chapter 4

AMP decorated and immobilized micelles

This chapter is based on published work entitled: Decorating nanostructured surfaces with antimicrobial peptides to efficiently fight bacteria.[223]

4.1 Introduction

Micro and nanostructured surfaces have evolved in Nature as broadly occurring passive strategies to prevent bacteria colonization with resulting host infections.[163,166] Features of surface structures, including, size and geometry, hamper bacterial attachment and survival.[40,254,255] The underliying principles of these naturally occurring passive defense strategies are key to mimicking their anti-biofouling efficiency by surfaces designed to fight bacterial infections without additional antimicrobial compounds. Antimicrobial or antifouling surfaces are important in many medical and industrial contexts.[1,256]

To improve the antimicrobial performance of microstructured surfaces in terms of functionality and biological efficacy, active surfaces have been developed by including antimicrobial agents.[1,20,62,257] The active agents can be either released from the surface or be effective upon contact.[258] The advantages of such surfaces include a high local concentration of the agent[193] and time-controlled release profiles.[206] In this respect, antimicrobial peptides (AMPs) are particularly appealing since they can be designed to display broad-spectrum antimicrobial activity, even against bacteria resistant to conventional antibiotics, besides excellent biocompatibility.[62,66,259] The amphipathic structure of AMPs, characterized by hydrophilic, cationic and hydrophobic domains,[61] allows for a multitude of effects, the most important being bacterial membrane lysis.[66,259]

KYE28 (KYEITTIHNLFRKLTHRLFRRNFGYTLR) is a particularly appealing AMP because it displayed improved antimicrobial effects when incorporated in surface-immobilized, microgel-based multilayers compared to when bound to plane glass surfaces or presented in peptide-loaded monolayers.[194] KYE28 is part of the helix D of human heparin cofactor II.[194] The antimicrobial action of KYE28 is based on bacterial cell membrane disruption which induces leakage and eventually leads to cell death.[260–262] Apart from broad spectrum antimicrobial activity, this peptide also exhibits potent anti-inflammatory effects by binding to circulating endotoxins and suppressing cytokine production.[260,263]

4.2 Scope of this chapter

There is a huge interest in surfaces that hinder bacterial attachment and proliferation on them. Therefore, the aim of the research presented in this chapter was to combine a passive antimicrobial strategy with an active antimicrobial strategy. The passive strategy involves the immobilization of micelles to create a microstructured surface and the active strategy the addition of the AMP KYE28 to the micelle-immobilized surface (**Figure 4.1**). The PMOXA-*b*-PDMS-*b*-PMOXA block copolymers used for micelle self-assembly are not only biocompatible, PMOXA is also known to decrease blood clotting and protein adsorption.[106] These features are advantageous for medical applications as they possibly suppress an immune response and/or bacterial colonization.[104,106] In addition, PMOXA is a peptidomimetic polymer known to be stable towards degradation.[106,107]

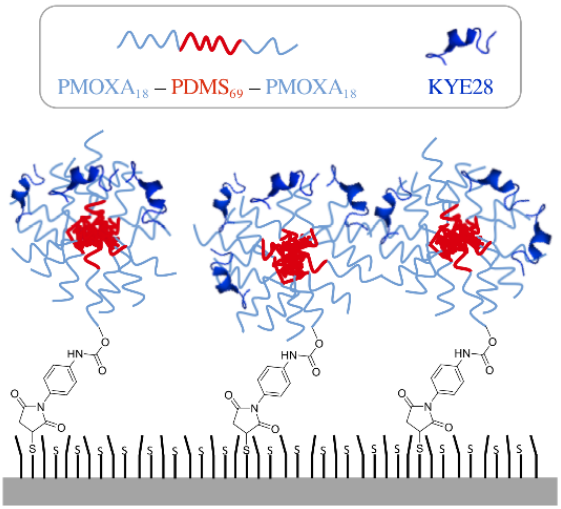

Figure 4.1: Schematic presentation of the combination of the passive (immobilized micelles) and active (AMP decoration) approach to create antimicrobial surfaces.

This chapter focuses on the design of a new antibacterial surface by combining a passive strategy, which reduces bacterial attachment, with an active strategy by the addition of an active AMP to kill bacteria and further reduce the bacteria load on the surface. Furthermore, a new immobilization technique which allows the immobilization of micelles without the need to self-assemble already functional group exposing nanostructures is studied. The aim is to further advance the research and knowledge in the field of antimicrobial surfaces by achieve following goals:

- (**i**) Micelle preparation and characterization.
- (**ii**) Optimizing micelle immobilization to create nanostructured surfaces.
- (**iii**) AMP synthesis and characterization.
- (**iv**) Characterization of AMP decorated nanostructured surfaces.

The approach developed in this chapter is based on the creation and careful physical characterization of surfaces with immobilized and AMP-decorated nanostructures. There is an interest to find new designs to successfully fight bacterial colonization.

4.3 Experimental Procedures

4.3.1 Material

The block copolymer $PMOXA_{18}$-*b*-$PDMS_{69}$-*b*-$PMOXA_{18}$ was obtained by Dr. Samuel Lörcher;[82] Si-wafers (⟨P100⟩) were obtained from Si-Mat Germany, silicon dioxide Quartz crystal microbalance (QCM) sensor chips (5 MHz quartz crystal, q-sense) from Biolin Scientific, p-maleimidophenyl isocyanate crosslinker (PMPI) and Atto-647 maleimide from Atto-Tec GmbH, dimethyl-sulfoxide (DMSO), anhydrous toluene, piperidine, N,N'-Diisopropylcarbodiimide (DIC), Diisopropylethylamine (DIEA), 3-(mercaptopropyl)trimethoxysilane, KI, diethyl ether, carboxyfluorescein (CF), and α-cyano-4-hydroxycinnamic acid from Sigma Aldrich. 1,2-dioleoyl-sn-glycero-3-phosphoethanolamine (DOPE), and 1,2-dioleoyl-sn-glycero-3-phosphoglycerol, monosodium salt (DOPG) were purchased from Avanti Polar Lipids. Ethyltrimetoxysilane was from Alfa Aesar, Bodipy630/650 from Thermo Scientific Inc., NaCl from Merck, and D-glucose monohydrate, and Triisopropylsilane (TIS) from Fluka. Milli-Q water (resistivity of $\geq$ 18 MΩ·cm) used was obtained from a Purelab Option-R 7/15 system (ELGA), henceforth referred to as H_2O. 0.9 % NaCl solution in Milli-Q is henceforth referred to as NaCl solution. Bacterial tryptone, yeast extract, agar, and soytone were from Becton Dickinson, potassium phosphate from AppliChem, and KYE28-Cys from Bio Peptide. Cl-MPA ProTide resin (0.2 mmol g^{-1}, 200 mesh), and OxymaPure were obtained from CEM, N,N-dimethylformamide (DMF) from J.T. Baker, Dichloromethane (DCM), and trifluoroacetic acid (TFA) from VWR, HPLC grade acetonitrile (ACN) from Scharlau. 9-fluorenylmethyloxycarbonyl (Fmoc) protected amino acids Ile, Lys(Boc), Tyr(tBu), Asn(Trt), Leu and Phe were purchased from Novabiochem and Gly, Thr(tBu), Arg(Pbf), His(Boc) from Iris Bio. All chemicals were used as received unless stated otherwise.

4.3.2 Micelle self-assembly and characterization

Micelle self-assembly was achieved using solvent evaporation. Briefly, a 10 mM stock solution of $PMOXA_{18}$-*b*-$PDMS_{69}$-*b*-$PMOXA_{18}$ was prepared in ethanol. 50 μL of the polymer solution was added to 1 mL of H_2O in a glass vial. The colloid was stirred at 350 rpm overnight at rt and stored at 4°C until further usage. The procedure to functionalize preformed micelles with maleimide moieties was modified from Kiene et al.[224] as follows: A stock solution of PMPI (1 mM) was prepared in DMSO and further diluted with H_2O to the corresponding concentrations (1 mM, 200 μM, 50 μM, and 19 μM) immediately before functionalization. Micelles (0.5 mM) were diluted (1:1 v/v) with the different PMPI concentrations resulting in 200, 40, 10, and 4 mol % PMPI. The reactants were mixed for at least 6 h at rt. Subsequently, the mixture was ultra-filtrated (5 min at 11,000 g) with a 30 kDa membrane filter to remove unreacted PMPI. The filtrate was washed with H_2O and filtered again (2x). Then, the filter cake was resuspended in H_2O to obtain a micelle suspension corresponding to 0.25 mM polymers.

For transmission electron microscopy (TEM), 5 μL micelle suspension were adsorbed to a glow discharged formvar-coated copper grid (400 mesh) for one minute. Excess sample was blotted off and the grid washed twice with water and once with 2 % uranyl acetate before being negative stained with 2 % uranyl acetate for 10 s. Dry grids were imaged with a Philips CM100 at an acceleration voltage of 80 kV.

Dynamic light scattering (DLS) was performed in triplicates on a Zetasizer Nano ZSP (Malvern Instruments) at 25°C. The micelle suspension (20 μL) was diluted with 480 μL H_2O and the scattering recorded at a backscattering angle of 173°. The zeta-potential (ζ) was measured in 10 mM NaCl on the same instrument at 25°C.

4.3.3 Peptide-Micelle interaction

KYE28 with an additional cysteine at the C-terminus (KYE20-Cys) was reacted to Atto-647-maleimide overnight at 4°C. The labeled peptide was purified by column purification (PD Minitrap sephadex G-25, GE Healthcare) to remove free Atto-647-maleimide.

Peptide-Micelle interactions were analyzed by fluorescence correlation spectroscopy (FCS) on a commercial Zeiss LSM 510 META/Confocor2. The micelles were mixed with Atto-647 labeled KYE28 or free dye overnight at 4°C. A 10 μL aliquot was then placed on a glass coverslip (0.16-0.19 mm thickness) and excited at 633 nm with a HeNe laser with a pinehole of 90 μm and a power of 5mW. Autocorrelation curves were recorded using a 40x water-immersion objective (Zeiss C/Apochromat, NA 1.2) and appropriate filter sets. The FCS autocorrelation curves were fitted with either a one component curve or a two-component curve where the diffusion time of the first fraction was fixed to the one obtained for free dye. The fitting was conducted as previously described.[93]

Anionic bacterial model liposomes were self-assembled from a 75/25 mol/mol mixture of DOPE / DOPG. The lipid mixture was dissolved in chloroform and dried to a thin film under vacuum. The thin film was rehydrated with 0.1 M CF dissolved in 10 mM Tris buffer, pH 7.4. The hydrated lipid mixture was treated with eight freeze-thaw cycles in liquid nitrogen followed by one minute heating in a 60°C water bath and 30 s vortexing. The sample solution was extruded 30 times through polycarbonate filters (pore size 100 nm) mounted in a LipoFast miniextruder (Avestin, Ottawa, Canada) to obtain unilamellar liposomes. Non encapsulated CF was removed by two subsequent gel filtrations (Sephadex G-50, GE Healtcare, Uppsala, Sweden) with Tris buffer as eluent. CF leakage was monitored on a SPEX-fluorolog 1650 0.22-m double spectrometer (SPEX Industries, Edison, U.S.A.) through emitted fluorescence at 520 nm. Liposomes were diluted with Tris buffer to obtain a 10 μM lipid sample for the leakage assay. After 10 min the substrate (peptide or micelle) was added and after another 30 min 0.8 mM Triton X-100 (Sigma-Aldrich, St. Louis, U.S.A.) was dropped into to disrupt the liposomes and obtain 100% leakage while the emitted fluorescence was monitored for another 5 min. Micelles were decorated with KYE28-Cys by mixing micelles and peptide together and keeping them at 4°C until gel filtration was conducted to remove non-attached peptide.

4.3.4 Synthesis of AMP KYE28

The peptide KYE28 (KYEITTIHNLFRKLTHRLFRRNFGYTLR) was synthesized by microwave-assisted automated solid phase peptide synthesis (Liberty Blue, CEM Corporation). Cl-MPA ProTide resin (0.2 mmol g^{-1}, 200 mesh) was used for the synthesis with DMF as the solvent. Fmoc protected amino acids were deprotected with piperidine (20% v/v, 3 mL) followed by coupling the next amino acid by amide bond formation in the presence of DIC (0.25 M, 1 mL), and a mixture of OxymaPure and DIEA (0.5 M and 0.05 M, 0.5 mL). The microwave power was set to reach 90°C (50°C for Histidine) during deprotection and coupling. The first amino acid was coupled to the resin in a more basic

environment, in a mixture of DIEA and KI (1 M and 125 mM, 1 mL). After microwave assisted synthesis of the complete sequence, the peptide bound resin was transferred to a syringe vessel, rinsed with DCM, and allowed to dry in air. Resin cleavage and amino acid side chain deprotection was accomplished by adding 4 mL cleavage solution (95 % TFA, 2.5 % H_2O, and 2.5 % TIS) and stirring for 4 h at rt and 80 rpm. After collection of the TFA mixture containing the cleaved peptide, the resin was washed several times with cleavage solution and the supernatants were combined with the peptide solution. The peptide was precipitated in ice cold diethyl ether (40 mL) and pelleted by centrifugation (5 min, 2300g). The supernatant was removed and the precipitated peptide resuspended in ice cold diethyl ether (repeated 3x). The precipitated peptide was finally dissolved in H_2O containing 0.1 % TFA and lyophilized.

The peptide was purified by semi-preparative reverse phase high-performance liquid chromatography (HPLC) (Shimadzu) on a Proto 300 (Higgins Analytical) C18 column (250 mm x 10 mm) with 5 μm particle size at a flow rate of 4 ml min^{-1}. The mobile phase was a mixture of ACN and H_2O each acidified with 0.1 % v/v TFA. The run started with 5 % ACN increasing linearly to 25 % over the first 4 min. Then, up to minute 26 a linear gradient from 25 % to 38 % ACN was applied to collect KYE28 around minute 24. After this, the column was washed with 95 % ACN up to minute 30 and decreased again back to 5 % over half a minute where it stayed until the end of the run at minute 37. UV-Vis absorbance was simultaneously measured focusing on λ = 214 nm. The solvents were evaporated in a rotary evaporator, followed by lyophilization.

Matrix-assisted laser desorption/ionization time of flight mass spectrometry (MALDI-Tof-MS) analysis of the peptide was performed on a Bruker Microflex system. A saturated α-cyano-4-hydroxycinnamic acid solution (1:1, v/v, H_2O:ACN, 0.1 % TFA) was mixed with 100 pmol μL^{-1} of purified peptide solution in H_2O at a sample to matrix ratio of 1:20 and 1 μL of the mixture was dropped onto the target plate and allowed to air dry.

4.3.5 Antimicrobial Activity of KYE28 - MIC and MBC

Minimal inhibitory concentrations (MICs), defined as the lowest concentration of an antimicrobial that will inhibit the visible growth of a microorganism after overnight incubation, were determined using *JM101 K12 Escherichia coli (E. coli)*. Overnight cultures of *E. coli* grown in LB medium (LB, 5 g bacterial tryptone, 2.5 g of yeast extract, 5 g NaCl, 500 mL H_2O) were pelleted and resuspended in 10 % tryptic soy broth (TSB) (1.7 g bacterial tryptone, 0.3 g soytone, 0.25 g of D-Glucose monohydrate, 0.5 g NaCl, 0.25 g potassium phosphate, 100 mL H_2O) in NaCl at a concentration of 10^7 colony forming units (CFU) mL^{-1}. KYE28 was diluted in H_2O at concentrations ranging from 125 μg/L to 64 mg/L as described in the NCSLA guidelines.[264] 90 μL of each KYE28 concentration were combined with 10 μL of *E. coli* (10^7 CFU mL^{-1}) per well in a 96-well plate and incubated overnight at 37 °C. MIC was determined.

The minimal bactericidal concentration (MBC), i.e. the lowest concentration of antimicrobial that will prevent the growth of an organism after subculture on to antibiotic-free medium was determined by plating 10 μL spots of undiluted samples from wells without visible growth of *E. coli* and from the lowest KEY28 concentration with visible *E. coli* growth on LB-agar plates (7.5 g agar/500 mL LB). The LB-agar plates were incubated overnight at 37 °C and quantitatively assessed the next day.

4.3.6 Production and characterization of surfaces with KYE28 decorated micelles

QCM sensor chips and 64 mm^2 squares cut from Si-wafers were functionalized with thiol groups. Therefore, the supports were activated for 5 min in an oxygen plasma[218] followed by being submerged in anhydrous toluene containing 0.3 % of silanes ((w/w); 3-(mercaptopropyl)-trimethoxysilane:ethyltrimetoxysilane, 1:1). Supports were shaken horizontally at 80 rpm overnight at rt, rinsed with toluene and ethanol and dried under a gentle stream of compressed air.[222]

For micelle immobilization, thiolated Si-wafer squares were placed in a 24-well plate and 450 μL of resuspended maleimide-micellar solution were added to each well. After shaking the plates at 80 rpm overnight at rt the surfaces were washed twice with H_2O and placed in a dry well.

To decorate the immobilized micelles with KYE28, 400 μL of a KYE28 stock solution (640 μg/mL in H_2O) were carefully applied to each well containing a surface. Alternatively, micelle-coated surfaces were placed in a Petri dish and 40 μL of KYE28 stock solution was added to each square. Squares were then covered with a sterile parafilm so that the droplet evenly spread over the whole surface and the KYE28 was left to adsorb overnight. Wet tissue was placed in the Petri dish to prevent drying of the protein solution.

Atomic force microscopy (AFM, JPK Nanowizard 3, Version 6.0.63) was used to characterize surfaces with immobilized micelles before and after peptide adsorption. Dry surfaces were measured in amplitude-modulation mode using a Tap300 Al-G cantilever (Budget Sensors, resonance frequency 280 kHz, force constant 40 N m^{-1}) for measurements in air, and a Tap75 Al-G (Budget Sensor, resonance frequency 75 kHz, force constant 3 N m^{-1}) for measurements in H_2O. The phase was always set to 0 deg. All images were recorded at a pixel resolution below the tip radius ($<$ 10 nm). Images were further processed and analyzed with Gwyddion (version 2.51).

The thickness of the modified surfaces was determined by spectroscopic ellipsometry (Accurion, Cauchy model). Three separate measurements on each surface were averaged.

Static water contact angles were measured with a drop shape analyzer (KRÜSS). Depending on the surface area 2-4 drops were analyzed per surface.

Confocal laser scanning microscopy (CLSM) was performed at 20°C on a ConcfoCor (ZEISS LSM 880, inverted microscope ZEISS Axio Observer, Carl Zeiss). Bodipy (10 mM in DMSO) was diluted in H_2O to a concentration of 25 μM and subsequently added to maleimide-micelles in H_2O to a final concentration of 50 nM. Bodipy-stained, surface-attached micelles were imaged using an oil-immersion objective (Plan Apochromat 63x/1.4 oil DIC M27) and a mean beam splitter (488/561/633). For images recorded in airyscan mode, a He-Ne laser at 633 nm wavelength was used as an excitation source (5 % laser power), with the pinhole set at 103 μm and the gain to 800. Intensity values were calculated with ZEN software and then normalized.

XPS measurements were carried out with a VG ESCALAB 210 spectrometer, using monochromatized AlK_a (1486.6 eV) as radiation source. 20 eV pass energy was applied for

all narrow scan measurements while 100 eV was applied for wide scans. Normal electron escape angle and a step size of 0.05 eV were applied. The Gaussian broadening of the spectrometer was calibrated for the 20 eV analyzer pass energy to 0.55 eV. The binding energy scale was calibrated with reference to the $4f_{7/2}$ level of clean gold sample at 84.0 eV binding energy. Fitting of the core level lines was performed applying the Doniach-Sunjic (asymmetrical Lorentzian) function[265] with Shirley background subtraction,[266] using UNIFIT for Windows (Version 2016) software.[267] The individual peaks were fitted by a convolution of an asymmetric function with Lorentzian and Gaussian line shapes. The intensities were then estimated by calculating the integral of each peak. Scofield sensitivity factors were used to derive the atomic concentrations.[268]

Quartz crystal microbalance with dissipation monitoring (QCM-D) was performed with a Q-Sense E1 system (Biolin Scientific, Sweden). All measurements were performed on 14 mm diameter, 5 MHz quartz crystal with a sputter-coated silicon oxide (model no QSX303) surface coating. Prior to experiments, each sensor crystal was rinsed with water, ethanol and then subjected to oxygen plasma (Harrick Plasma, Ithaca) to remove undesired contaminants. The clean sensors were functionalized with thiol moieties as described for the Si-wafers. All QCM-D measurements were conducted under continuous flow conditions, with a flow rate of 50 μL min^{-1}, and controlled by an IPC pump from Ismatec. The measurements were recorded at multiple odd overtones (5th, 7th, 9th) and the data shown was obtained at the seventh overtone (n=7). The viscoelastic modelling was done with the Qtools software package assuming a film density of 1000 kg m^{-3} and a bulk aqueous solution viscosity of 0.001 Pa s^{-1}. For the viscoelastic modelling, data produced from 5th, 7th, and 9th overtones were used. The data are expressed as the mean $\pm$ standard deviation of the mean where appropriate. All measurements were performed in triplicates.

4.3.7 Antibacterial Activity of Micelle Modified Surfaces

Functionalized Si-wafer squares were placed in a 24-well tissue culture plate and infected with 1 mL of *E. coli* ($5{\cdot}10^4$ CFU mL^{-1},[269] 1 % TSB in NaCl). *E. coli* were allowed to adhere for 90 min at 37°C without agitation. Non-adherent cells were removed by washing with NaCl. Surfaces were placed in a fresh well, covered with 10 % TSB in NaCl and incubated for 20 h at 37°C. Subsequently, planktonic cells were removed by washing with NaCl and modified surfaces were stained with the LIVE/DEAD BacLight stain (ThermoFisher Scientific). Stained surfaces were visualized with the CLSM using a water immersion objective (C-Apochromat 40x/1.2W Korr FCS M27) with excitation at 488 nm and 561 nm wavelengths (each 1.5 % laser power) and a mean beam splitter (488/561/633) at 20 °C. The pinhole was set to 47 μm and the gain to 600. Fluorescence was tracked from 500-550 nm and 610-718 nm. Fluorescence images were processed with Fiji.[270] In parallel, corresponding surfaces were transferred to 15 mL falcon tubes and sonicated for 5 min with 2 mL 1 % TSB in NaCl to disperse adherent bacteria. The bacteria suspension was serially diluted (10^{-1}, 10^{-2}, 10^{-3}, 10^{-4}, 10^{-5}, 10^{-6}) in NaCl and 50 μL of each dilution were spotted in triplicate on LB-Agar plates. After an overnight incubation at 37°C, the CFUs were counted on the 10^{-3} dilution if numbers were adequate, or back calculated for this dilution from a countable dilution (n = 3). Further on, Welch's t-test was applied.

4.4 Results and Discussion

4.4.1 Micelle Self-Assembly

Micelles were formed by self-assembly of $PMOXA_{18}$-*b*-$PDMS_{69}$-*b*-$PMOXA_{18}$ block copolymer[82] and characterized by a combination of DLS, TEM, and ζ-potential measurements. TEM analysis revealed single particles with a homogenous micellar morphology (**Figure 4.2**). A mean radius of 15 ± 6 nm was determined by measuring over 100 micelles on several TEM micrographs. Consistently, DLS measurements yielded a unimodal peak associated with a hydrodynamic radius (R_h) of 19 ± 5.5 nm (**Figure 4.3**). A ζ-potential of 5 mV indicated that the surface charge of the micelles was neutral.

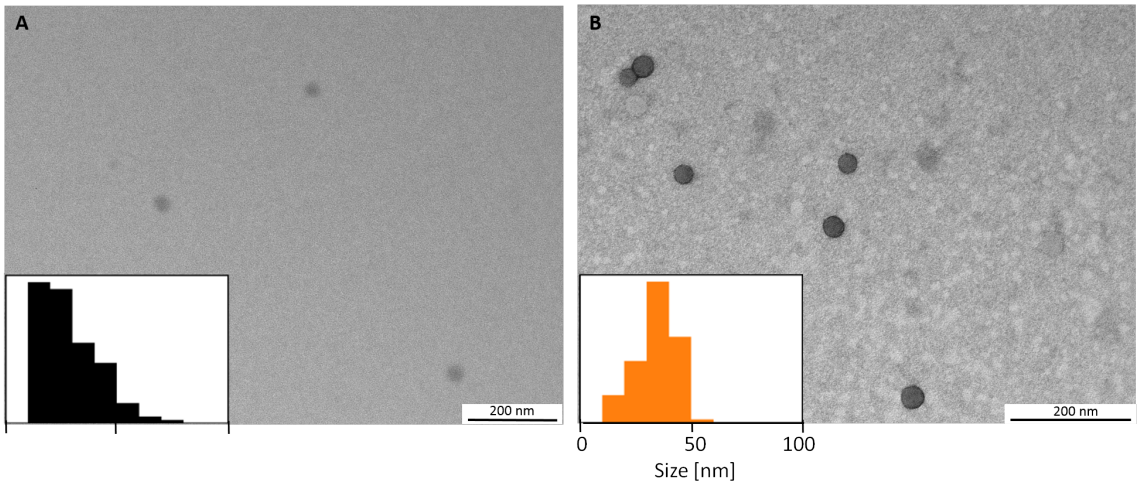

Figure 4.2: TEM micrographs with inlets of the size distribution histogram measured by image processing of A) micelles assembled from $PMOXA_{18}$-*b*-$PDMS_{69}$-*b*-$PMOXA_{18}$ and of B) assembled micelles reacted to p-Maleimidophenyl-isocyanate (PMPI). Scale bars: 200 nm.

4.4.2 Peptide-Micelle interaction

Amphiphilic molecules including AMPs are known to interact with polymeric nanostructures[162] and the adsorption of KYE28 to the micelles was investigated. Therefore, the peptide was fluorescently labeled with Atto-647 maleimide, and its interaction with the micelles studied by FCS. FCS auto-correlation curves were recorded for free Atto-647-maleimide in solution, the Atto-647-KYE28 in solution, and micelles mixed either with free dye or Atto-647-KYE28 (**Figure 4.4**). The auto-correlation curves for free dye (black curve) and micelles incubated with the dye (blue curve) overlapped, and similar diffusion times of 56 ± 2 μs and 62 ± 3 μs, respectively, were calculated. This data indicated that the dye is freely moving in solution and not interacting with the micelles. In contrast, a shift to a higher diffusion time (157 ± 35 μs) was obtained for the labeled KYE28 (green curve). The calculated R_h based on the diffusion time increased from 0.9 nm for free dye to 2.3 nm for labeled KYE28. The auto-correlation curve was fitted with a two component model, where one diffusion time was fixed to the one previously measured for the free dye. This fitting showed that 34 % of the dye was still free in solution while 66 % was attached to the peptide. Mixing the micelles with the labeled peptide (red curve) lead to a significant shift toward longer diffusion times (747 ± 63 μs). This shift to slow diffusion reflects

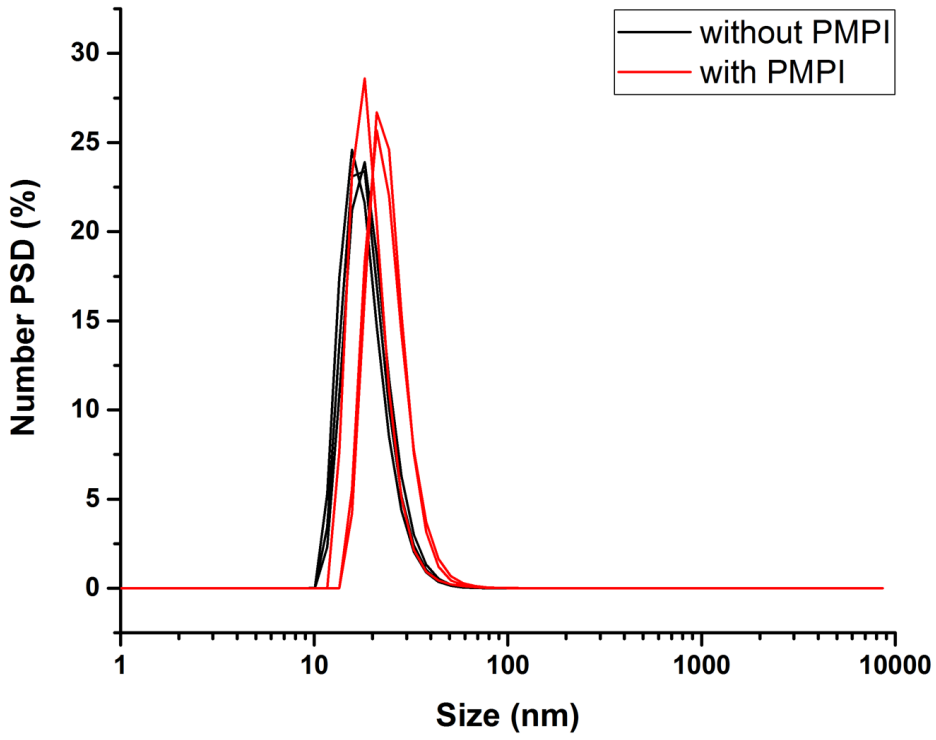

Figure 4.3: DLS measurements of micelles without PMPI (black) and after reaction to PMPI (red) revealed similar number particle size distributions (PSD). The two samples were measured each three times.

that the labeled peptide was interacting with the micelles to yield KYE28-decorated micelles. An R_h of 11 ± 1 nm was calculated from the diffusion time obtained for micelles interacting with labeled peptide, which is in good agreement with the size of the micelles previously determined by TEM and DLS. The counts per molecules (CPMs) recorded for free dye, labeled peptide, and micelles interacting with labeled peptide indicate an average of one dye molecule per peptide and one to two labeled peptides per micelle (**Table 4.1**).

	τ_D [μs]	Fraction [%]	CPM [kHz]	CR [kHz]
Atto 647 maleimide (dye)	56 ± 2	100	30.6 ± 0.6	22.5 ± 0.3
Micelle + dye	62 ± 3	100	33.4 ± 0.4	222 ± 3
Labeled Peptide	157 ± 35	66	29.5 ± 1.0	688 ± 143
Micelle + labeled peptide	747 ± 63	99	49.4 ± 1.4	1796 ± 75

Table 4.1: FCS fitting parameters of the micelle-peptide interaction study.

To test whether KYE28 decoration conferred antimicrobial properties upon micelles, CF encapsulating DOPE/DOPG (75/25 mol/mol) liposomes were mixed with micelles. These liposomes are mimicking the anionic bacterial membrane and are extensively used in AMP

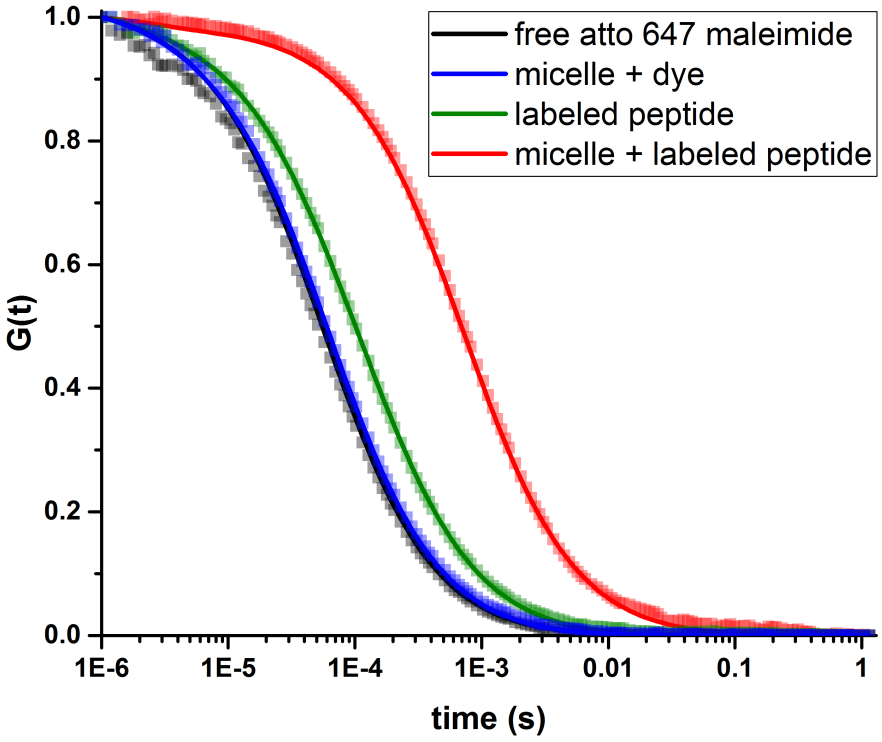

Figure 4.4: Normalized FCS auto-correlation curves of Atto-647 maleimide (black), dye mixed together with micelles (blue), Atto-647 labeled KYE28 peptide (green), and micelles mixed with Atto-647 labeled KYE28 peptide (red). Raw data are represented by squares while the fitted autocorrelation curves by a colored line.

studies. Importantly, the DOPE/DOPG membranes gave similar results on AMP interaction, as membranes prepared from *E. coli* lipid extracts. Furthermore, these liposomes agreed with bacterial lysis experiments.[271] CF is a fluorescent dye which is self-quenched at high concentrations, thus showing increased fluorescence when diluted.[272] CF was encapsulated in bacterial membrane mimicking liposomes to monitor the ability of the peptide and micelles to induce leakage and therefore, destroying the integrity of the anionic membrane mimicking DOPE/DOPG liposomes (**Figure 4.5**). The detergent Triton X was added in the end to determine 100 % leakage. In the self-leaking experiment, the stability of the liposomes was confirmed. The peptide free in solution caused leakage in a dose-dependent manner. With a high concentration of 1 μM 100 % leakage was caused, while with a lower concentration of 0.1 μM partial leakage of 45 % was was reached (**Figure 4.5A**). The micelles (10 μM polymer) alone did not result in any detectable liposome lysis. In contrast, micelles decorated with 1 μM peptide before purification by gel filtration, led to 67 % leakage (**Figure 4.5B**). These results suggest that the bare micelles free in solution will not harm bacteria, but should be able to kill them when decorated with KYE28.

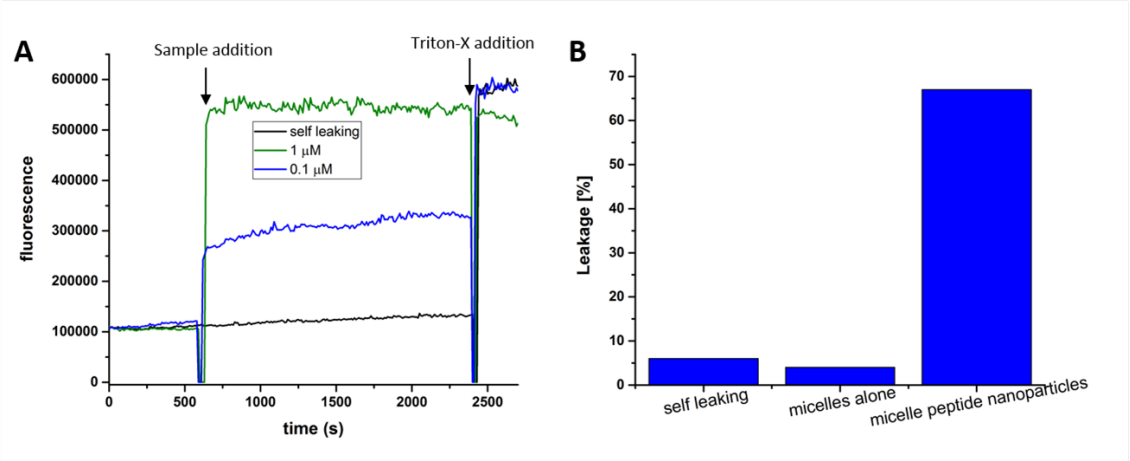

Figure 4.5: Leakage experiments on CF-containing DOPE/DOPG liposomes. After 10 min, the sample was added to the liposome solution and after an additional 30 min Triton-X was added to cause 100 % leakage. A) Peptide alone in two different concentrations: 1 μM Peptide led to 100 % leakage while 0.1 μM led to 45 % leakage. B) Micelles alone did not cause any leakage; the leakage was in the range of the self-leaking of liposomes. The AMP decorated micelles caused nearly 70 % leakage.

4.4.3 Surface functionalization

Micelles and surfaces were functionalized with opposite moieties to enable the immobilization. To obtain a surface with a 50 % relative density of thiol groups for further coupling, Si-wafers were functionalized by silane chemistry with a 1:1 mixture of thiol and ethyl functionalized silanes.[218,222] The functionalized surfaces were analyzed by amplitude modulation AFM to characterize material properties by height and phase. No significant height difference across the surface was expected as the silane functionalization is known to result in self-assembled monolayers.[273] Therefore, to study non-functionalized and functionalized Si-Wafers the focus has to be put on the phase, indicating if the interaction between the AFM tip and the surface is attractive (positive phase) or repulsive (negative phase). Compared to non-functionalized Si-wafers where the phase was negative and homogeneous (**Figure 4.6A and C**), phase imaging of the functionalized surface revealed material differences that indicate the presence of thiol and ethyl groups. The yellow ellipsoidal patches of 10-50 nm in diameter (**Figure 4.6B and C**) are likely to reflect thiol groups due to increased attractive behavior towards the tip than other regions as the hydrophilicity of the thiols is higher compared to the ethyl groups.

The surfaces were further analyzed by ellipsometry and static water contact angle (**Figure 4.7**). The functionalization of the Si-wafer with thiol groups led to a decrease in hydrophobicity from 67° ± 1° to 58° ± 1° water contact angle due to the polarity of the thiol groups. An increased thickness from 4.3 to 5.0 nm was modeled by ellipsometry, representing the added silane layer composing of 50 % thiol functionalized silanes.

4.4.4 Immobilization of Micelles on Functionalized Surfaces

To covalently attach micelles to the thiol functionalized Si-wafers by means of thiol-maleimide Michael addition, maleimide exposing micelles were produced by functional-

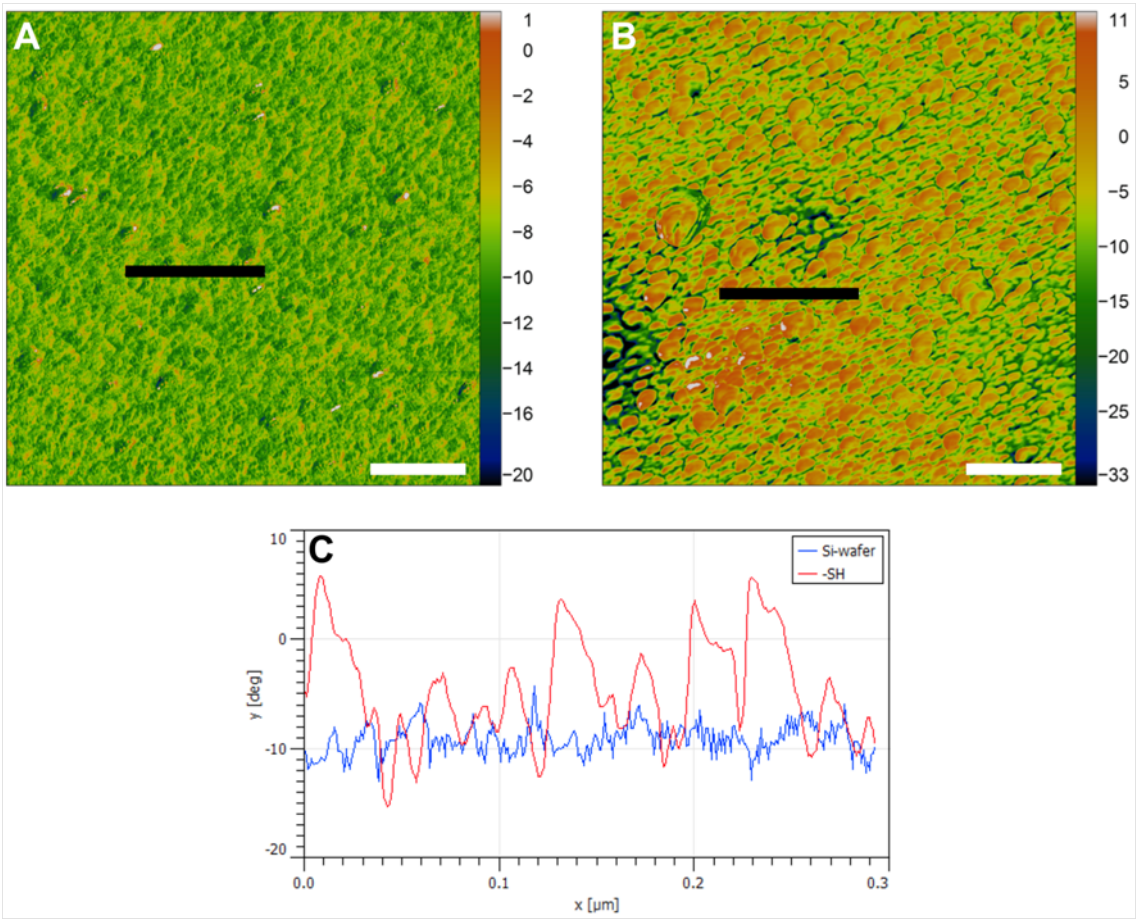

Figure 4.6: AFM micrograph showing the phase (°) channel of A) untreated Si-wafer and B) thiol functionalized Si-wafer. Scale bars are shown in white: 200 nm. C) Measured profile lines in black (300 nm, A, B) of the phase are displayed.

izing already preformed micelles with different concentrations of PMPI-crosslinker in an easy one pot reaction. Due to possible hydrolysis up to 200 mol % PMPI was reacted to micelles. TEM (**Figure 4.2**) and DLS analysis (**Figure 4.3**) before and after PMPI addition demonstrated that shape and diameter of the micelles remained largely unaffected by functionalization with maleimide. Specifically, a radius of 16 ± 5 nm was obtained from TEM and an R_h of 23 ± 6 nm by DLS for micelles after their reaction to PMPI . Low ζ-potentials of 5, 5, and 4 mV were measured for 4, 40, and 200 mol % PMPI. The corresponding surface charge was comparable to that of non-functionalized micelles, with all samples having a solvent conductivity of 0.7 Sm^{-1}.

Thiol functionalized surfaces were reacted overnight with maleimide exposing micelles to create surfaces with immobilized micelles. To trace the micelles by fluorescence, Bodipy630/650, a hydrophobic dye adsorbing non-specifically to micelles,[88] was added prior immobilization. The fluorescent intensities of immobilized micelles that were maleimide-functionalized with different concentrations of PMPI (0 - 200 mol %) were examined by CLSM (**Figure 4.8**) to compare immobilization efficiencies between the different micelles added to the surface. Surfaces reacted with Bodipy-stained maleimide-functionalized mi-

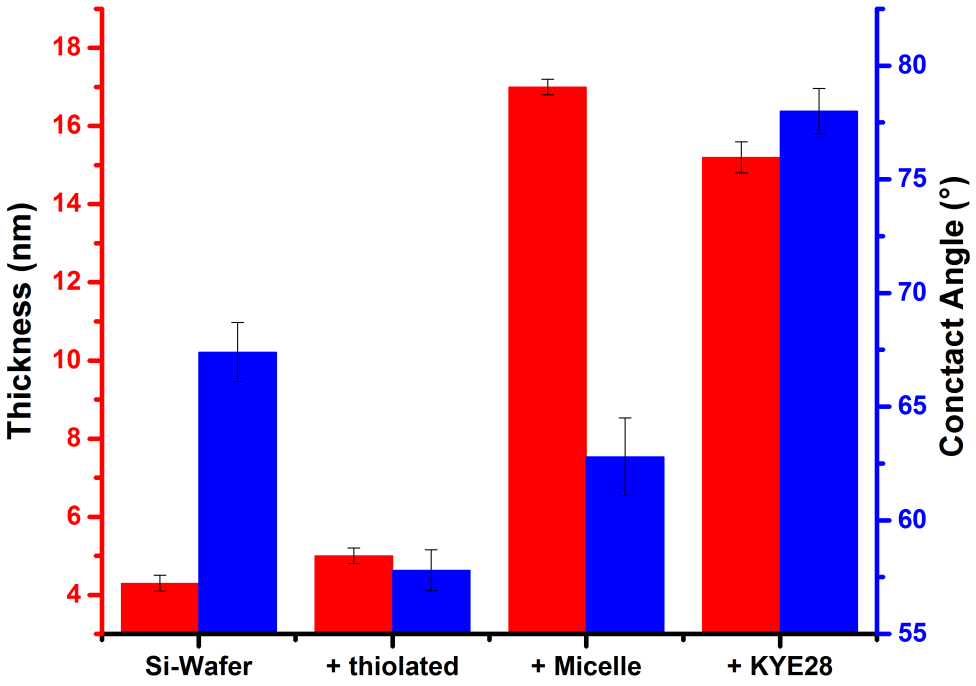

Figure 4.7: In situ assessment of thickness by ellipsometry (red bars) and static water contact angles (blue bars) during different stages of surface fabrication. Error bars were calculated by a standard deviation for all samples (n=3).

celles showed higher fluorescent intensities and therefore more micelles on the surface, than those treated with Bodipy-stained micelles lacking maleimide. The different amounts of PMPI used for maleimide functionalization did not have a significant influence on the fluorescent intensities, suggesting a similar extend of immobilization. This data corroborated that maleimide-functionalized micelles can be covalently immobilized on thiol-functionalized surfaces by the Michael addition and that only little maleimide functionalities were needed to achieve stable immobilization of micelles. The surface roughness was calculated from AFM micrographs. It showed that the less PMPI was used for maleimide grafting the rougher was the final surface. However, the complete absence of maleimide resulted in the lowest roughness (**Figure 4.8**). The surface corrugation is indicative of individual micelles being immobilized, as individual micelles are larger and stick out from the surface. Together, these results show that for the successful immobilization on thiol-functionalized surfaces, maleimide-exposing micelles are crucial.

As PMPI is sensitive to moisture, a tenfold excess is suggested to overcome hydrolysis. Therefore, the 10 mol% PMPI presumably corresponds to 1 mol% functional groups, which has previously been used for polymersome immobilization.[222] Based on these considerations, a concentration of 10 mol% PMPI was chosen for all further experiments. Moreover, the fluorescent intensity study showed that this concentration was sufficient for successful

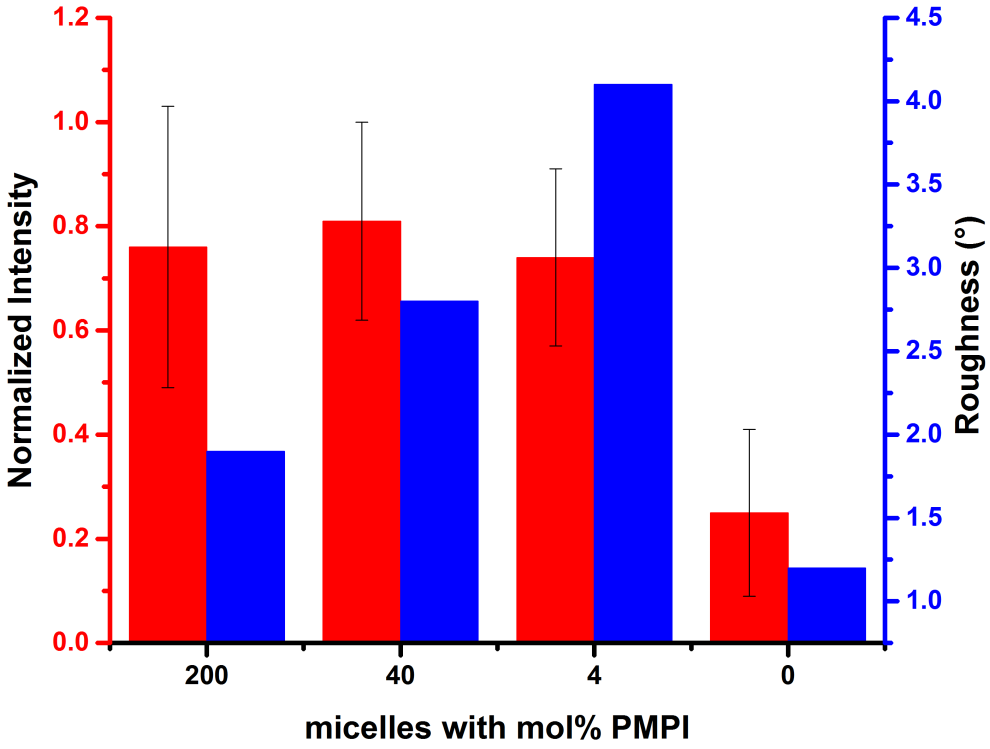

Figure 4.8: Confocal laser scanning microscopy intensities (red) comparison and AFM calculated roughness (blue) comparison between immobilized micelles treated with different mol% PMPI (0-200) prior immobilization.

immobilization.

AFM micrographs recorded in liquid (H_2O) (**Figure 4.9A and B**) and in air (**Figure 4.10A-C**) revealed immobilized micelles in the phase and height channels. The micelles were detected with a higher phase than the surrounding, which was indicative of an increased attractive regime. This was likely due to the higher hydrophilicity of the polymer micelles attached to the thiol patches compared to the surrounding surface. When recorded in liquid the micelles displayed a lower height than when recorded in air.

When assessed by ellipsometry(**Figure 4.7**), the thickness was found to be increased by 12 nm due to the immobilized polymeric micelles. The final thickness for a surface with surface-attached micelles was therefore 17.0 nm. The water contact angle of 63° (**Figure 4.7**) indicates that the hydrophobicity stayed similar to thiol-functionalized surfaces.

4.4.5 Synthesis of the antimicrobial peptide KYE28

The AMP KYE28 was synthesized by Fmoc solid-phase peptide synthesis with microwave heating having the advantage of reduced synthesis time and chain aggregation.[274] This peptide was chosen as a model peptide due to its antimicrobial and anti-endotoxic prop-

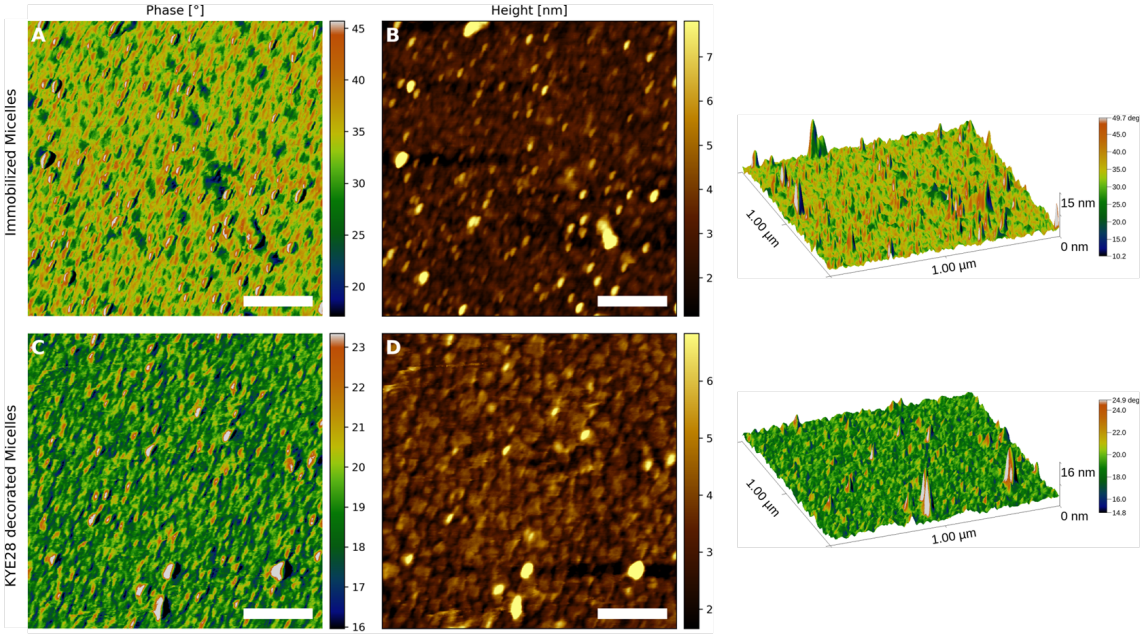

Figure 4.9: AFM images recorded in H_2O of surfaces before and after adsorption of KYE28. A) Phase-contrast image and B) height image of surfaces with immobilized micelles lacking KYE28. C) Phase-contrast image and D) height image of surfaces after KYE28 adsorption. On the right side are displayed 3D images of the height with phase as overlay of immobilized micelles (top), and of the surface after KYE28 adsorption (bottom). Scale bars: 200 nm.

erties.[261] The main peak in the HPLC elugram of the raw peptide corresponds to KYE28 and was collected during the depicted time around minute 24 (**Figure 4.11A**). The mass was confirmed by MALDI ToF-MS, where the single and double charged species are observed at 3591 m/z and 1792 m/z, respectively (**Figure 4.11B**). A yield of up to 22 % after HPLC purification was achieved. The peptide was purified successfully as visible by the HPLC elugram of the purified KYE28 solution (**Figure 4.12**).

First, we assessed the antimicrobial potential of the purified KYE28 peptide in solution, the MIC and MBC were measured and determined to be both 32 μg/mL corresponding to 8.9 μM. This was in the range of the MICs that have been reported for KYE28 using different bacteria species and strains.[261]

4.4.6 Modification of Surface-Attached Micelles with the antimicrobial peptide KYE28

KYE28 was dissolved in water (640 μg/mL) and adsorbed to the surface-immobilized micelles by overnight immersion of the surface in the peptide solution (450 μL). An HPLC elugram of the KYE28 solution was recorded before and after immersion of the surface to estimate the amount of adsorbed peptide (**Figure 4.12**). The concentration of KYE28 in the solution was reduced by 28 %, corresponding to a possible maximum of 80 μg KYE28 on the surface, comparable to findings by Nyström et al.[193] The surface was either used in dry state for AFM, ellipsometry or static water contact angle measurements, immersed in water for liquid AFM studies or immersed in bacteria medium for antimicrobial testing.

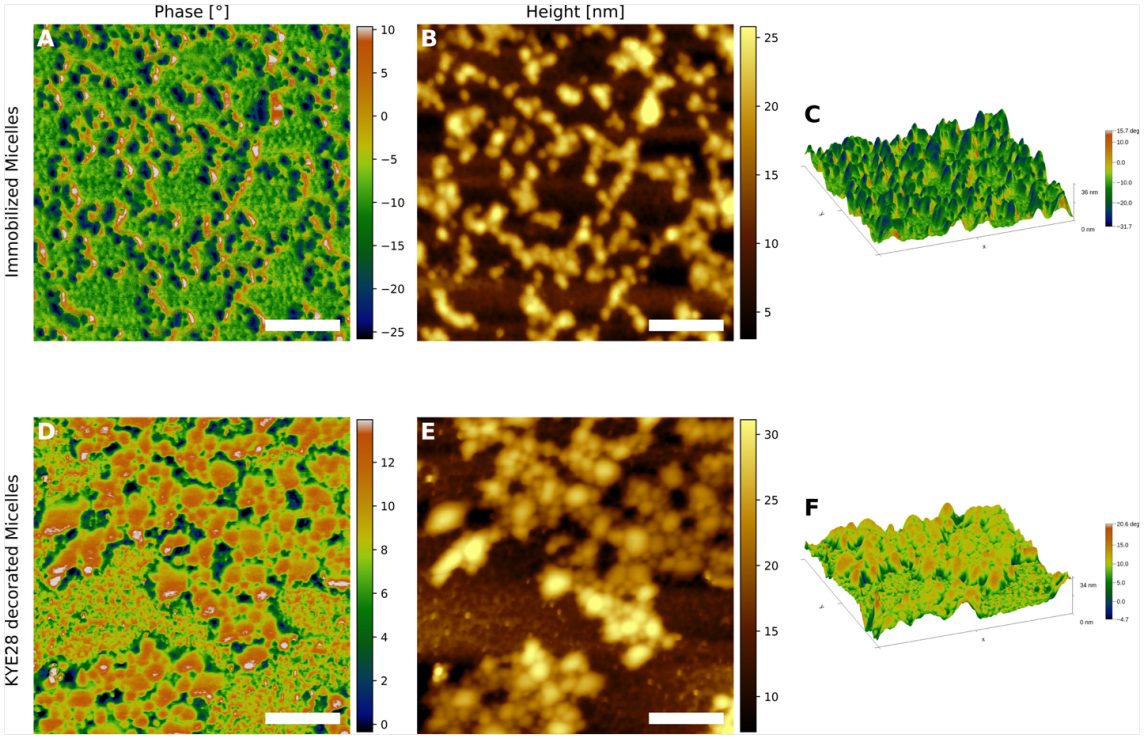

Figure 4.10: AFM micrographs recorded in air of immobilized micelles. A and D) Phase contrast images, B and E) height images, and C and F) 3D images of the height with phase as overlay of immobilized micelles (top), and of a surface after KYE28 adsorption (bottom). Scalebars are A-B) 400 nm, and D-E) 200 nm. C) Axis length is 2 μm, and F) axis length is 1 μm.

The increased phase shift in AFM micrographs showed that after KYE28 adsorption, the micelles remained more attractive to the AFM tip than the surrounding areas. (**Figure 4.9A and C and 4.10D and F**). However, compared to surfaces with immobilized bare micelles, for which the average phase was around 30-35°, the overall phase was reduced to 20°, i.e., exhibited less attractive forces after KYE28 decoration (**Figure 4.9A,C**). Height images revealed the structures on the surface to be in a similar size range (**Figure 4.9B and D and 4.10B and E)**. Further, upon peptide adsorption, the surface lost parts of its previous flexibility as indicated by the overall lower phase. Similar effects were found for peptide loaded on surface-bound microgels.[275] It is possible that the peptide incorporated between the outer hydrophilic polymer blocks in the micelle and thereby hampered flexibility. Furthermore, KYE28 decoration led to a slight increased water contact angle of 78°, i.e., an increase in hydrophobicity of the surface possibly results from the amphiphilic nature of the peptide. In addition, ellipsometry revealed a slight decrease in thickness to 15.2 nm upon KYE28 adsorption (**Figure 4.7**). This decrease is likely due to a reduced water content resulting from the incorporation of the amphiphilic AMP.[276]

X-Ray photoelectron spectroscopy (XPS) was further employed to analyze the chemical composition of the different surfaces. XPS of thiol-functionalized, immobilized micelles, and KYE28-decorated, immobilized micelles revealed the presence of O, N, C, and Si (**Figure 4.13A**). On surfaces with immobilized bare or KYE28 decorated micelles the N 1s peak was detected. It represents the nitrogen in the PMOXA block of the triblock

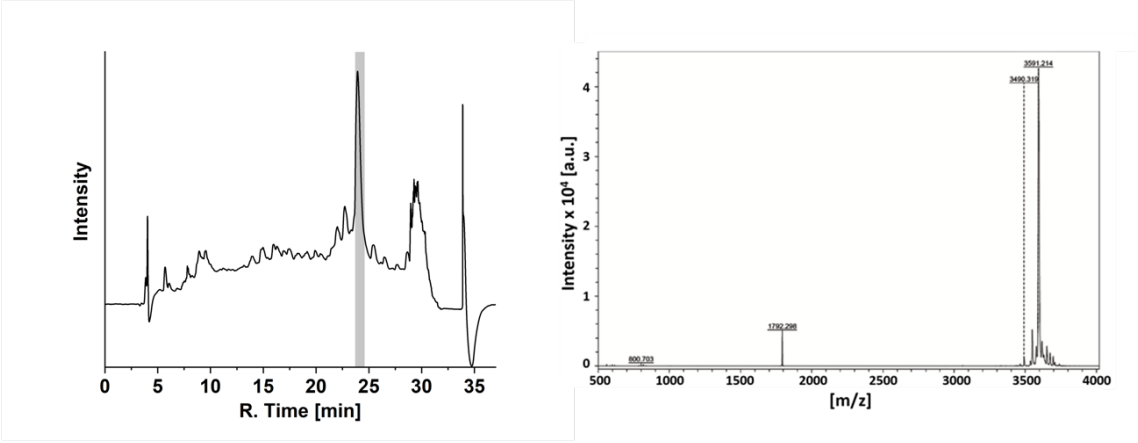

Figure 4.11: A) HPLC elugram. The grey area was collected. B) Linear positive MALDI-ToF spectra of the collected KYE28.

copolymer, and additionally, the nitrogen in the peptide in case of the KYE28-loaded surface. Accordingly, the nitrogen concentration was 3.6 and 7.3 atomic percent (at. %) (**Table 4.2**). A corresponding peak of low intensity (0.8 at. %) was also found on the thiolated surface (**Figure 4.13B**), reflecting nitrogen adsorption from the atmosphere.

Surface modification	N [at. %]	C [at. %]	O [at. %]	Si [at. %]
Thiolated	0.8	20.3	41.9	37.0
Immobilized micelles	3.6	47.7	27.1	21.6
Immobilized miecelles with adsorbed KYE28	7.3	57.7	21.7	13.3

Table 4.2: Atomic percent (at. %) calculated from XPS measurements.

Moreover, this surface showed some metal impurities at binding energies of 796 eV, 781 eV for cobalt and 228 eV for molybdenum, which were absent on both micelle-derived surfaces. These metal impurities came from the solvent (ethanol) used to wash the surfaces after thiol functionalization. However, the surfaces with immobilized micelles were rinsed with H_2O and thus, metal impurities were washed away.

The surface analysis by XPS showed changes in the C 1s core level spectra for each surface, proofing the chemical difference between them. The high resolution spectra were deconvoluted into three components for the surfaces with immobilized micelles. The peak at 289 eV, not seen for thiolated surfaces, is characteristic of guanidine and carboxylic acid groups (**Figure 4.13C**). For the peptide decorated surface, the peak broadened towards higher binding energies due to Histidine, Arginine, and Glutamic acid (287 eV, 289 eV).[277] A long peptide with various different amino acids increases the complexity of the peak with many different contributions and therefore more components at different binding energies are needed to model it. Thus, the broadening was explained by a deconvolution using five components. Two components corresponding to guanidine and imidazole (289 eV, 287 eV) were added in comparison to bare micelles (**Figure 4.13C and Figure 4.14**).[277] KYE28 adsorption on the surface-attached micelles was further supported by a 2-fold increase

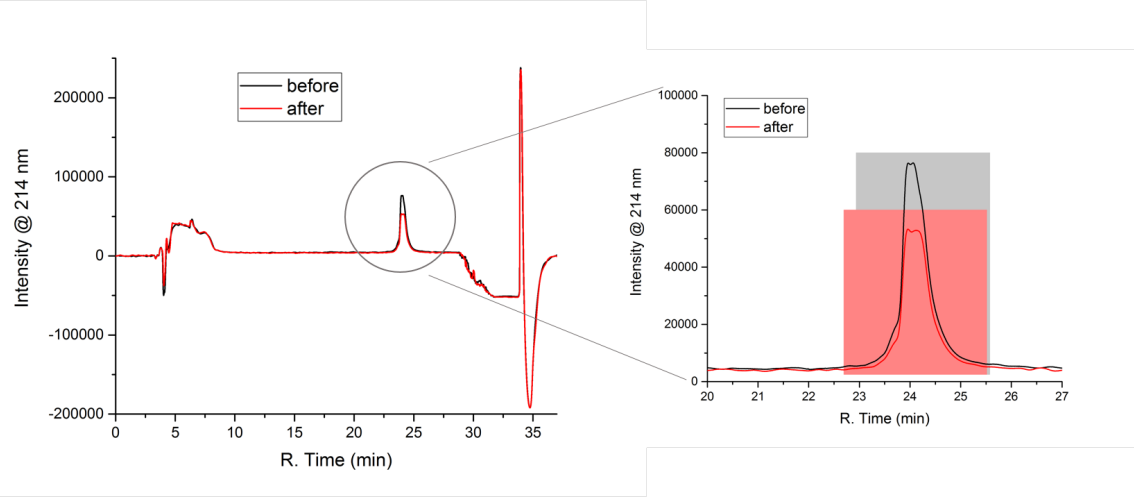

Figure 4.12: HPLC elugram of the KYE28 solution before immersing the micelle immobilized surface in it (black) and after immersing the surface in it (red) to let the peptide adsorb onto the immobilized micelles.

of nitrogen amount due to the peptide backbone and nitrogen containing amino acids. Furthermore, the relative amount of carbon increased to 57.7 at. % and oxygen decreased to 21.7 at. % (**Table 4.2**). These results clearly demonstrate the immobilization of the micelle and their decoration with KYE28, the latter localized to a large extent in the periferal corona of the immobilized micelles based on hydrophobic interactions.

QCM-D experiments monitored the immobilization of maleimide exposing micelles and the subsequent adsorption of KYE28 in real time (**Figure 4.15**). First, a stable baseline was established on thiol functionalized QCM chips. After injecting micelles into the QCM-D chamber, the resonance frequency immediately dropped (ΔF = (-123 $\pm$ 14, -119 $\pm$ 14, -114 $\pm$ 13) Hz for the 5^{th}, 7^{th}, and 9^{th} overtone, respectively) relative to the mass accumulation on the chip (**Figure 4.15A,B,E,F**). At the same time, the dissipation increased (ΔD = (9.7 $\pm$ 1.1, 9.9 $\pm$ 1.5, and 9.7 $\pm$ 1.3) $*10^{-6}$ for the 5^{th}, 7^{th}, and 9^{th} overtone, respectively) indicating increased viscoelastic properties (**Figure 4.15C-F**). Based on viscoelastic models, which are fed by the frequencies and dissipations measured, a density of 2.6 mg mm^{-2} was estimated for micelles immobilized on the sensor surface. It is important to note that this value does not correspond to the dry micelle density but to hydrated micelles which include associated H_2O oscillationg with the chip during the measurements.[276] After micelle adsorption, the surface was rinsed with water. The shift in frequency and dissipation indicated the removal of non-covalently attached micelles upon rinsing. The viscoelastic model showed a mass reduction to 2.2 mg mm^{-2}, which corresponds to a mass reduction of 15 %. When KYE28 solution was applied to immobilized micelles on the QCM-D chip, the frequency increased (ΔF to -104 $\pm$ 2, -102 $\pm$ 3, and -100 $\pm$ 2 Hz for the 5th, 7th, and 9th overtone, respectively) and therefore, the mass decreased to 2.1 mg mm^{-2}, corresponding to a further mass reduction of 5 %. Furthermore, a drop in dissipation was observed (**Figure 4.15**). Similar frequency shifts after peptide addition have been reported in QCM-D studies on the interaction of AMPs with lipid membranes.[278,279] Furthermore, an increase in frequency resulting in an underestimation of protein adsorption has been reported for thick polymer surfaces with low

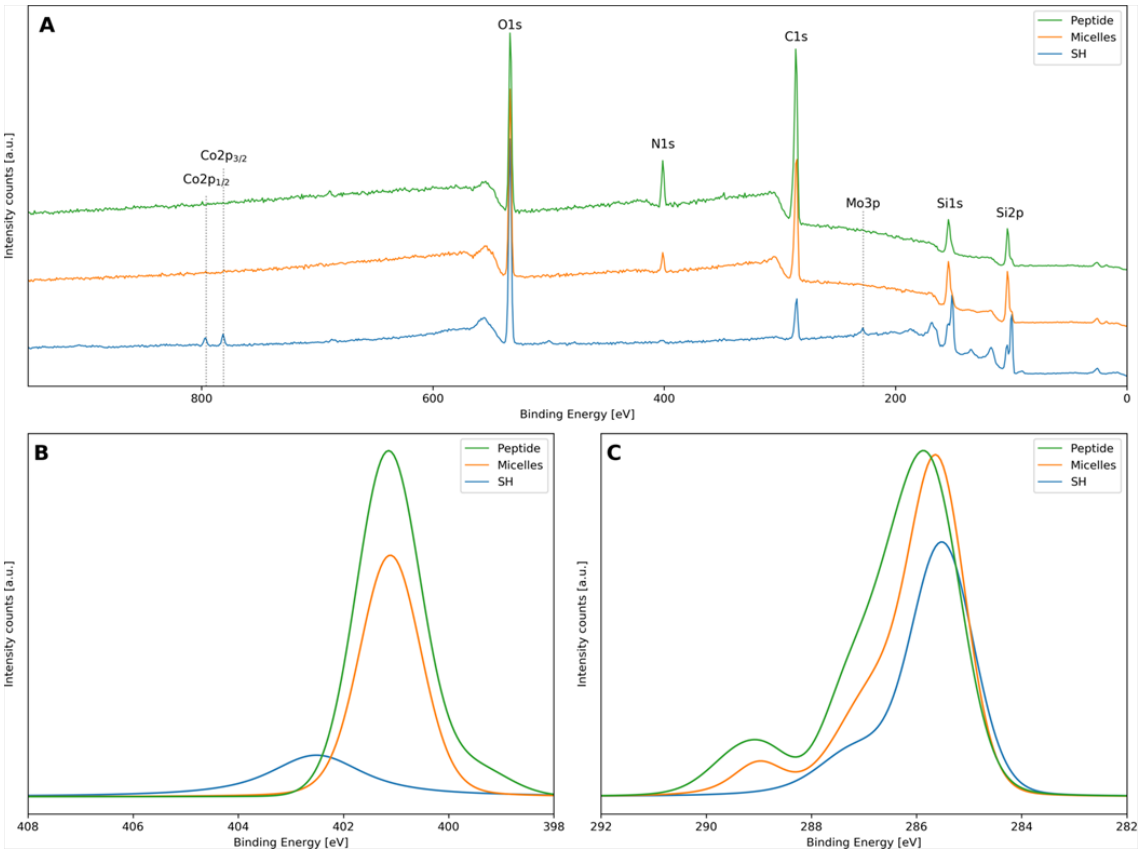

Figure 4.13: XPS spectra of thiolated surfaces (blue), surfaces with immobilized micelles (orange), and surfaces with KYE28-decorated micelles (green). A) Wide-scan XPS spectra with vertical shift, B) Overlapped, fitted and normalized curves for N 1s, and C) C 1s.

viscosity. It has been suggested that the adsorption of the protein leads to a partial collapse of the polymer strains and water is squeezed out.[276] We believe that a similar effect of peptide adsorption occurs in our system. Specifically, peptide binding is expected to result in osmotic deswelling, and hence in the release of trapped hydration water. Consistent with this notion, KYE28 loaded into anionic poly(acrylic acid)-based microgels has been found to result in an increase of frequency, associated with a drop in mass due to the removal of adsorbed water.[194] Despite such complications in mass quantification for KYE28-decorated micelles, the QCM-D experiments revealed that micelle immobilization and decoration were fast processes, occurring within minutes.

4.4.7 Antimicrobial Activity of Peptide-Modified Micelle Surfaces

The KYE28-decorated nanostructured surface was tested for its antimicrobial potential using a static biofilm formation assay.[280] Different surfaces were immersed in an *E. coli* inoculum (5 *10^4 CFU mL^{-1}) and adhering bacteria were allowed to proliferate in bacteria growth medium overnight at 37°C. After 20 h, surfaces were stained with a LIVE/DEAD cell staining kit and imaged by CLSM to qualitatively assess the growth of bacteria (**Figure 4.16A-C**). Initial biofilm formation was found on thiol-functionalized wafers. Note that there is always a small fraction of dead bacteria in *E. coli* inoculum, and therefore, a fraction of dead bacteria was present on all surfaces, including bare Si-wafers and

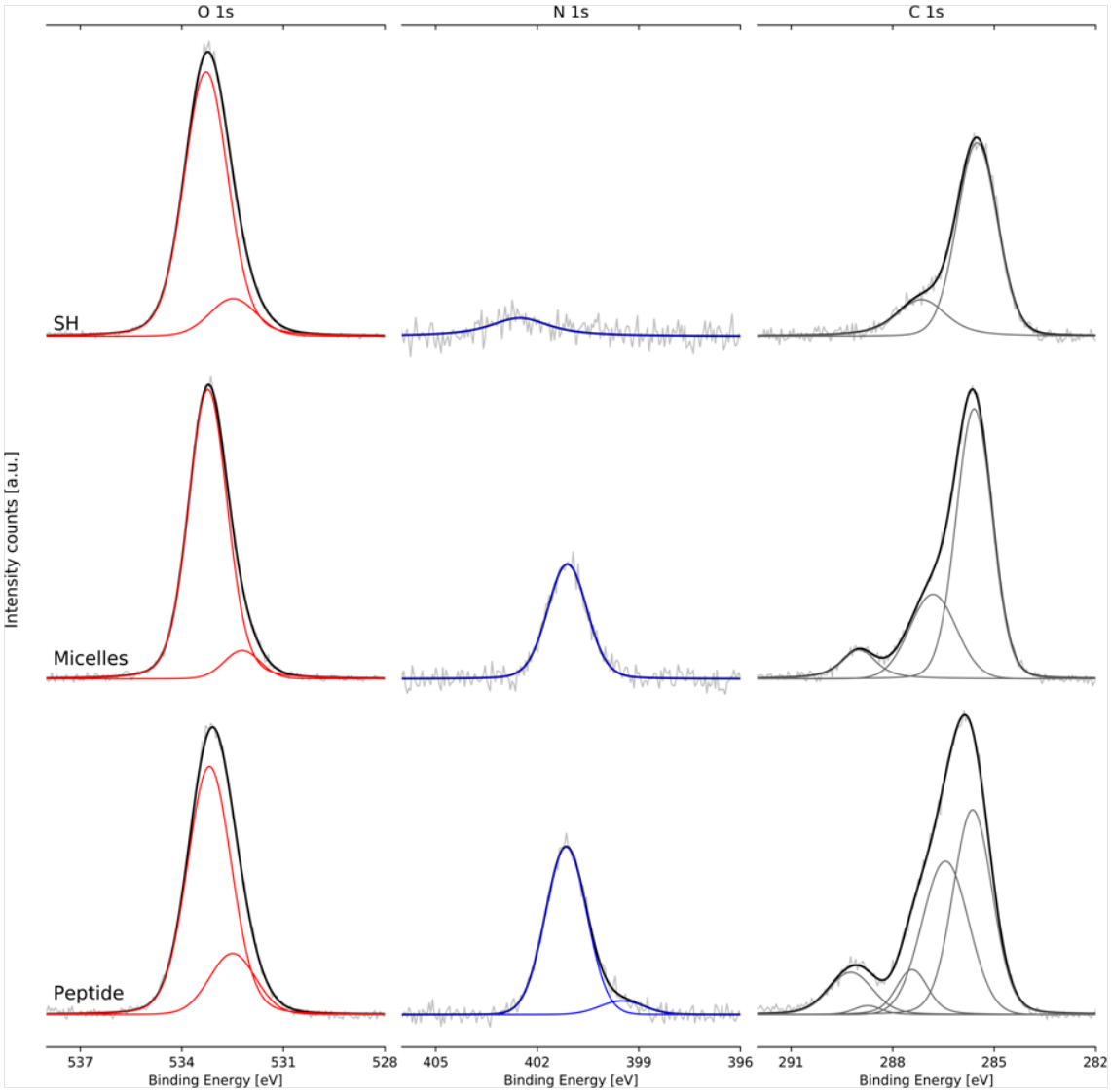

Figure 4.14: XPS O 1s, N 1s, and C 1s core level spectra of thiolated, micelle immobilized and peptide decorated surfaces. Measurements are displayed in a semi-transparent line while the fitted sum of the components is in black. The components for O 1s, N 1s, and C 1s, are in red, blue, and grey, respectively.

thiol-functionalized wafers. On surfaces with immobilized micelles or KYE28 decorated micelles, small bacteria agglomerations and single bacteria were observed. The adsorption of KYE28 to micelles, clearly reduced the number of adhering bacteria. These data are in line with findings for KYE28 loaded surface bound anionic microgels reported by Nyström et al.[193] To quantitatively assess the number of surviving celles, bacteria were detached from the surfaces by sonication and spotted on LB-Agar plates for CFU counting after 24 h (**Figure 4.16D**). *E. coli* were able to adhere and proliferate better on non-functionalized Si-wafers or thiolated surfaces, compared to surfaces with bare micelles. On the latter, *E. coli* survival was reduced by more than half to 43 % compared to non-functionalized wafers and to 35 % compared to thiol-functionalized surfaces. This reduction of bacteria survival demonstrates the efficacy of the passive strategy based on surface attached PMOXA-*b*-

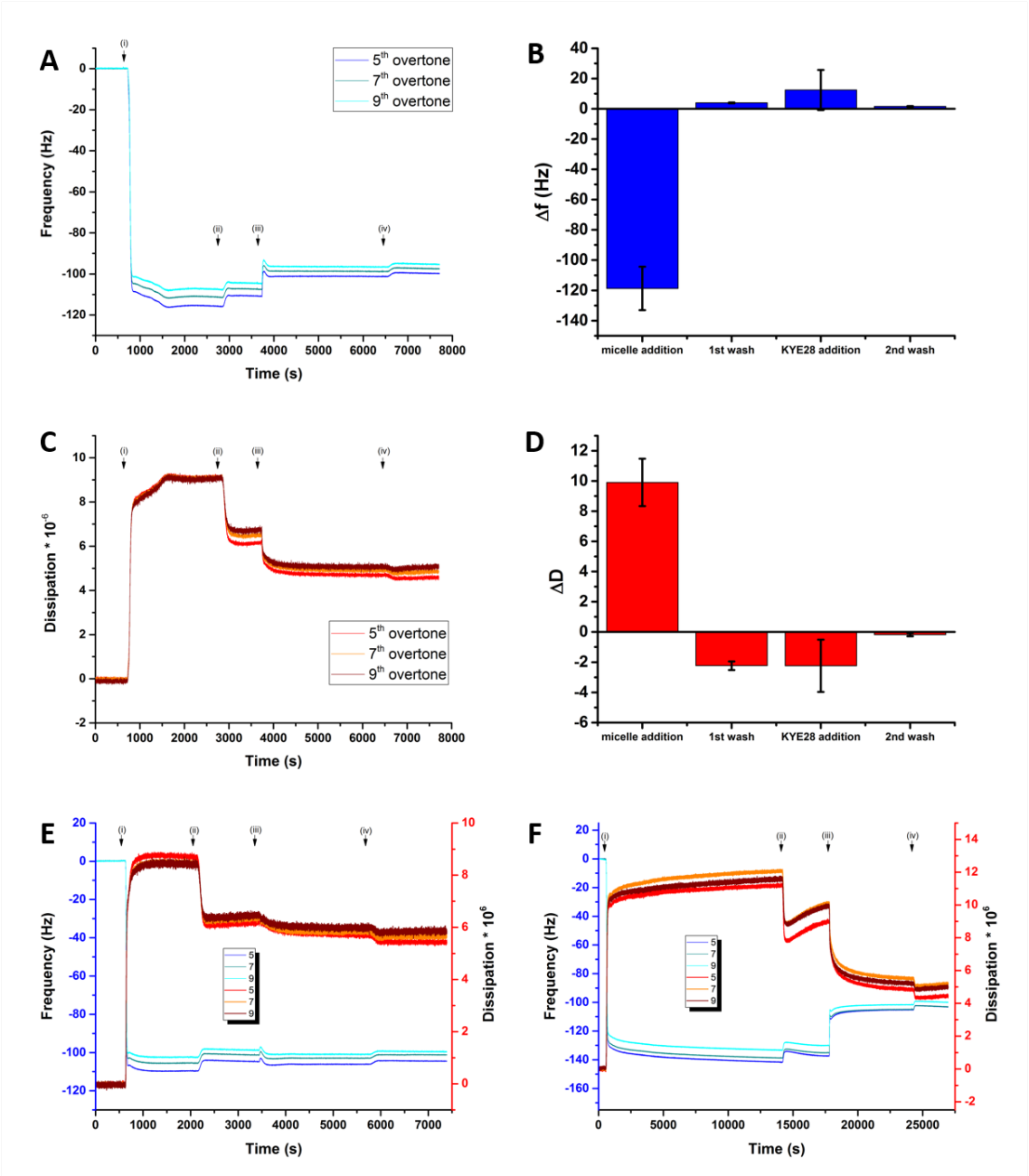

Figure 4.15: QCM-D measurements of surface deposition and KYE28-loading of micelles. Simultaneous changes in frequency and dissipation were recorded at 3 overtones (n=5, 7, 9) as a function of time. A) Frequency diagram and C) dissipation diagram of a representative QCM-D experiment. E and F) Additional QCM-D diagrams where the blue colors show the frequencies of the 5th, 7th, 9th overtone while the red colors show the dissipations of the same overtones. While applying continuous flow (50 μL/min), equilibration of the chip with H_2O followed by (i) injection of micelles dispersed in H_2O, (ii) 1^{st} washing with H_2O, (iii) injection of KYE28 dissolved in H_2O, and (iv) 2^{nd} washing with H_2O. Diagrams represent the averaged shifts in B) frequency and D) dissipation for the 7^{th} overtone.

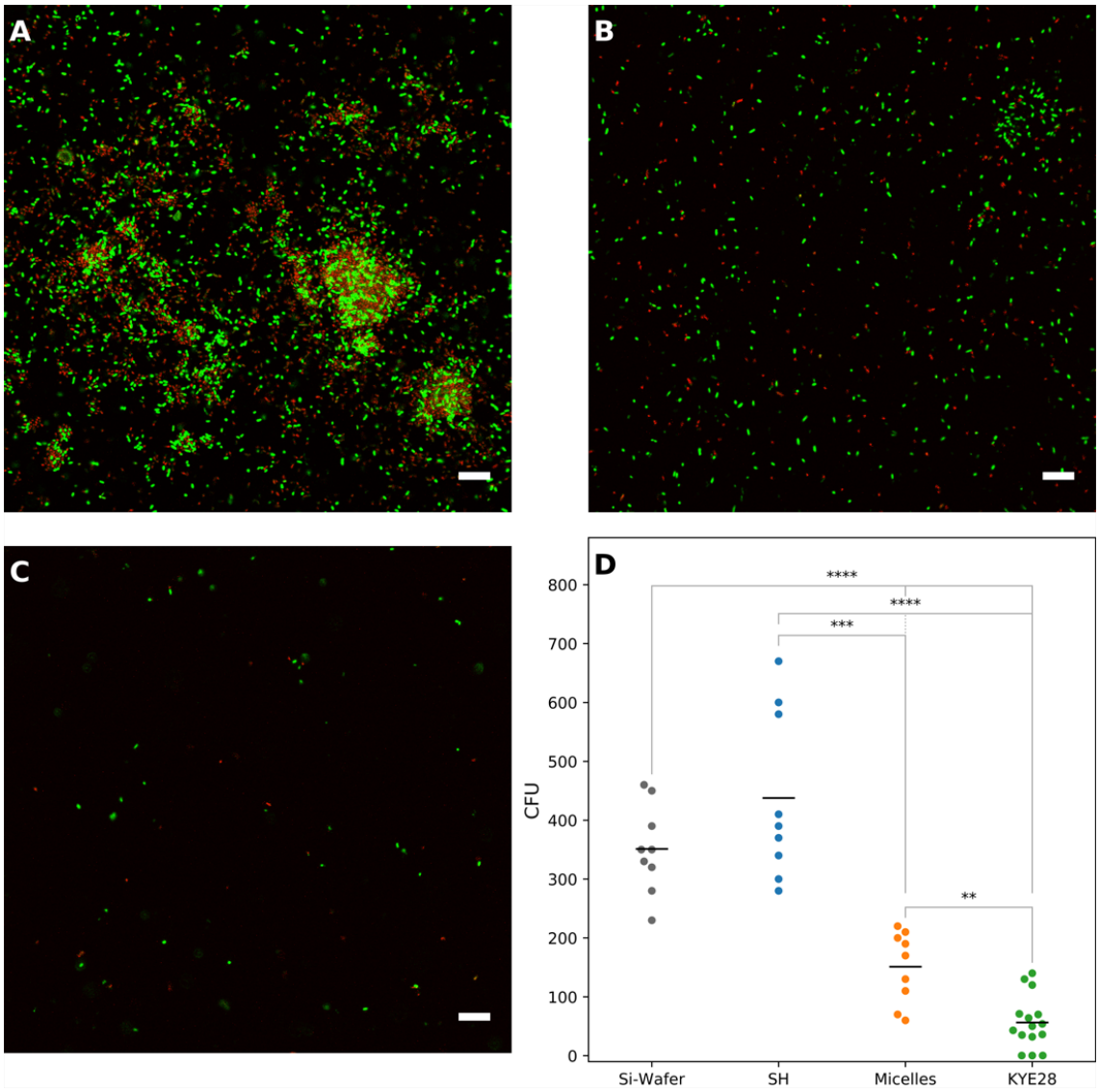

Figure 4.16: Static biofilm assay. The surfaces were visualized by CLSM after staining the adhering bacteria with the LIVE/DEAD stain. Bacteria with a damaged membrane were stained with propidium iodine (red, dead), whereas bacteria with intact membranes were stained with cell-permeable Syto9 (green, alive). A) thiolated surface, B) immobilized micelles, and C) immobilized micelles with adsorbed KYE28. Scale bars, 10 μm. D) CFU counting for the 10^{-3} dilution. Black bars represent the average values of the measurements (Welch's t-test, ** $p < 0.01$, *** $p < 0.001$, **** $p < 0.0001$, $n \geq 3$).

PDMS-*b*-PMOXA micelles. The adsorption of KYE28 to the micelles further reduced the adherence and survival of bacteria on the surface to 16 % compared to non-functionalized wafers and to 13 % compared to thiol-functionalized surfaces. Thus, the passive defense by the nanostructured surface was enhanced and the overall antimicrobial properties of the surface were improved by decorating micelles with the active component KYE28.

4.5 Conclusions

Passive and active approaches were combined for the efficacious prevention of bacterial growth. The passive strategy consisted of nanostructured surfaces that were successfully designed and generated by immobilizing PDMS-*b*-PMOXA-*b*-PDMS micelles on a thiol functionalized surface by Michael addition. Attachment of micelles which in solution hardly affected bacterial growth, rendered the surface antibacterial compared to non-functionalized and thiol-functionalized surfaces. When the antimicrobial peptide KYE28 was incorporated into the surface-bound micelles as an active component, *E. coli* survival was further reduced. Thus, the passive defense properties bestowed by immobilized micelles were enhanced by the active module. The dual strategy of the antimicrobial AMPs (active) and nanostructured surface (passive) allows an optimization of the antimicrobial efficacy and opens new avenues in the fight against biofilm formation. Importantly, this design of modular antimicrobial surfaces is straightforward and scalable by few modification steps. In addition, the functional properties can be readily changed by the choice of peptide,[281,282] as long as it is able to interact with the micelles while retaining its activity. Varying the peptide-polymer combination might also result in an increased decoration efficiency. Future modifications of the active module for example by combining different AMPs with overlapping bacterial spectra or synergistic antimicrobial effects, or by the combination of antimicrobial effects with anti-inflammatory effects and other biological functionalities, open up opportunities for specifically tailored antimicrobial surfaces.

Chapter 5

Microstructured surfaces with Cephalexin producing nanoreactors

5.1 Introduction

Microstructured surfaces that minimize the risk of infections are widespread in nature. Research ideas in most disciplines often start by observing nature and trying to mimic the structures of interest. Further the mimics will then be optimized and improved for a specific application by adding possible non-natural components. Antibacterial surfaces can be enriched with antibiotic agents. Despite the possible cytotoxicity of silver, silvernanopraticles (AgNPs) are considered a safe reservoir of antimicrobial silver cations. AgNPs are very effective in killing bacteria by releasing silver ions. Antiseptic creams containing silver are on the market as well as materials (e.g., wind instrument heads, medical devices) with protective silver coatings.[283] Immobilization of AgNPs seems to increase the antimicrobial potential compared to free AgNPs in solution.[228]

Cephalexin is a cephalosporin that belongs to the class of β-lactam antibiotics like the penicillins. Its action is based on the disruption of the bacterial cell wall synthesis and it is effective against *S. aureus, S. epidermidis, E. coli* and *P. mirabilis*.[153,154] Cephalexin can be produced enzymatically by the enzyme penicillin acylase (PA) which catalyses the condensation of phenylglycinmethylester (PGME) and 7-aminodesacetoxycephalosporanic acid (7-ADCA). Due to the broad substrate specificity and the high regio-, stereo-, and chemoselectivity, PA is able to resolve racemic mixtures. In addition to condenstation reactions the enzyme also hydrolyses the acyl side chains of penicillins and cephalosporins.[284,285] PA is used in industry to produce 6-aminopenicillanic acid or 7-ADCA, the starting materials for various semi-synthetic β-lactam antibiotics.[286] The catalytic pocket uses only one single amino acid, a serine, for the catalytic centre.[287]

The outer membrane pore F (OmpF) is a bacterial membrane protein which allows the passive diffusion of molecules up to about 600 Da.[138] The susceptibility to β-lactam antibiotics or also fluoroquinolones is dependent on non-specific porins like the OmpF for entry of these drugs into the bacteria. It is an important pore also for the creation of antibiotic resistances as bacterial mutations can hinder the entry of antibiotics into the bacteria, by slightly changing the pore structure and/or by reducing the amount of pores in the

bacterial membrane.[288] The OmpF channel is asymmetric, meaning the pore has different characteristics at the outer and inner face of the membrane. Because penicillins have a size similar to the narrowest part of the pore, they can occlude the OmpF during their passage through the pore. However, interactions between pore wall and the antibiotic can help to let the antibiotic pass through the pore. Important for these mostly electrostatic interactions are the charges and therefore, the pH of the solution.[289–291] Mahendran et al. showed that negatively charged compounds translocated more efficiently through the pore than zwitterionic ones.[292]

Certain short peptides can also arrange them self in the membrane to create a pore. Melittin (GIGAVLKVLTTGLPALISWIKRKRQQ), a 26 amino acid peptide, is such a pore producing peptide. It is the main pain producing substance in bee venom, presumably due to its strong interactions with cell membranes and its pore forming abilities.[293] While melittin translocates through the membrane, it forms short lived pores[294] for which a toroidal pore model has been suggested.[295] The peptide:lipide ratio influences the pore size; higher ratios leads to bigger pores.[294] Interestingly, melittin has also antibacterial properties.[293] MelP5 (GIGAVLKVLATGLPALISWIKAAQQL) is a melittin where 5 amino acids have been changed to make the peptide less charged (+3 instead of +6) and thereby more hydrophobic. MelP5 was more effective in pore formation as a lower peptide concentration already resulted in pore formation and the pores were larger and sometimes longer lasting.[296]

5.2 Scope of this chapter

There is a huge interest in smart surfaces that successfully fight bacterial colonization. Therefore, the aim of the research presented in this chapter was to create microstructured, smart antimicrobial surfaces where passive and active antimicrobial strategies are combined. The active strategy involving the production and immobilization of cephalexin producing nanoreactors was developed and examined in our laboratory at the University of Basel whereas the microstructured surfaces exhibiting passive defense properties were designed and provided by the collaborating research group of Prof. Jian Xu from the Chinese Academy of Science, Institute of Chemistry (**Figure 5.1**).

This chapter focuses the design and development of an antimicrobial producing nanoreactor permeabilized by OmpF or melittin. Furthermore, the characterization and antimicrobial testing of several materials and surfaces for possible passive strategies are presented. The aim is to further advance the knowledge in the field of smart antimicrobial surfaces by achieving the following goals:

- (**i**) Characterization of a microstructured surface designed to allow for a passive antimicrobial strategy.
- (**ii**) Encapsulation of enzymes into polymersomes to create nanoreactors.
- (**iii**) Nanoreactor permeabilization for antibiotic release.
- (**iv**) Nanoreactor immobilization on a microstructured surface.

The dual antimicrobial approach contemplated in this chapter is based on the careful characterization of the surfaces and the nanoreactors. Furthermore, two different nanoreactor

permeabilization strategies were studied.

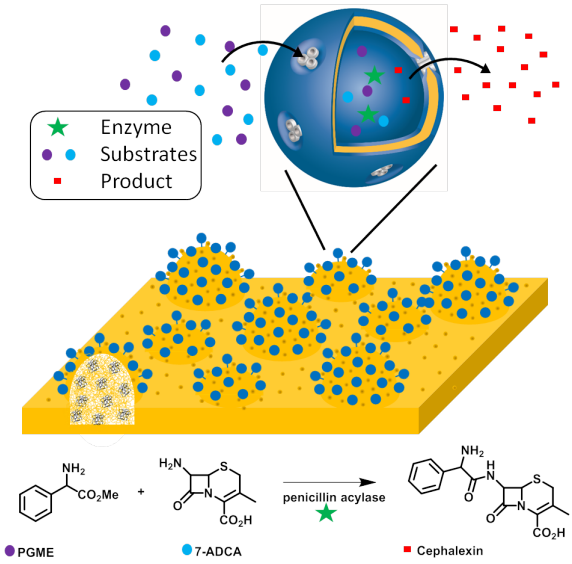

Figure 5.1: Schematic presentation of the microstructured surface with immobilized nanoreactors.

5.3 Experimental Procedures

5.3.1 Materials

Polypropylene and cotton based materials as well as organosilica covered glass and silica surfaces were prepared by the research group of Prof. Dr. Jian Xu. Bacterial tryptone, yeast extract, agar, and soytone were from Becton Dickinson; potassium phosphate dibasic (K_2HPO_4) was purchased from AppliChem; sodiumchlorid (NaCl), sodium phosphate dibasic (Na_2HPO_4) from Merck, D-glucose monohydrate, and zinc chloride from Fluka; Potassiumchlorid (KCl), Cephalexin hydrate, sodium carbonate (Na_2CO_3), sodium hydrogen carbonate ($NaHCO_3$), sodium hydroxid (NaOH), horseradish peroxidase (HRP), (R)-(-)-2-phenylglycine methyl ester hydrochlorid (PGME), 7-Aminodesacetoxycephalosporanic acid (7-ADCA), HPLC grade trifluoroacetic acid (TFA), Sepharose 2B, D-Sorbitol, Atto488-NHS, 5(6)-carboxyfluorescein (CF), and melittin from Sigma Aldrich; HPLC grade acetonitrile (ACN) from Scharlau; *E. coli* penicillin acylase (PA) (MW = 70 kDa) from ASA Spezialenzyme GmbH; octyl glucopyranoside (OG), and Triton X-100 from Anatrace; and bodipy630/650, and 3,3',5,5'-tetramethylbenzidin (TMB) from Thermo Scientific. Purified OmpF was kindly provided by Andrea Belluati, [122] $PMOXA_6$-*b*-$PDMS_{43}$-*b*-$PMOXA_6$ and azid terminated $PMOXA_7$-*b*-$PDMS_{40}$-*b*-$PMOXA_7$ by Dr. Samuel Lörcher. [82]

5.3.2 Microstructured surface - passive strategy

The antimicrobial activity was assessed by the Japan industrial standard (JIS) test. 50 μL *E. coli* inoculum ($8.3{\cdot}10^5$ CFU mL^{-1}) was added to the surface of interest and covered with a sterile square of parafilm. The surface was kept overnight at 37°C in a humid environment. The next day, the surface including the parafilm was placed in a 15 mL falcon tube containing 3 mL 1% tryptic soy broth (TSB) (1.7 g bacterial tryptone, 0.3 g

soytone, 0.25 g of D-Glucose monohydrate, 0.5 g NaCl, 0.25 g K_2HPO_4, 100 mL H_2O) in PBS (137 mM NaCl, 2.7 mM KCl, 10 mM Na_2HPO_4, 1.8 mM KH_2PO_4, pH = 7.4) and sonicated for 5 min to remove all attached bacteria. The resulting bacteria suspension was serially diluted (10^0, 10^{-1}, 10^{-2}, 10^{-3}) in PBS and 50 μL of each dilution was spotted in triplicate on LB-Agar (5 g bacterial tryptone, 2.5 g yeast extract, 5 g NaCl, 7.5 g agar, 500 mL H_2O) plates and incubated overnight at 37 °C. Colony forming units (CFUs) were counted the next day. Static water contact angles (KSV, instruments, CAM100 Version 2.1.1) were measured for at least 3 surfaces.

Surfaces with adsorbed organosilica microparticles were sputtered with platinum and characterized by scanning electron microscopy (SEM) (Hitach S-4800) with an acceleration voltage of 5000 V at a working distance of 3.4 mm. In addition, the surface covered with 1 μm particles was imaged by atomic force microscopy (AFM) (JPK Nanowizard 3, Version 6.0.63) in air. A Tap300 Al-G cantilever (Budget Sensors, resonance frequency 300 kHz, force constant 40 N m^{-1}) was used for AC mode measurements. Images were analyzed with the JPK data processing software (Version spm_6.0.63).

Bacterial attachment was studied by immersing the surface of interest in 2 mL *E. coli* inoculum ($5{\cdot}10^5$ CFU mL^{-1}) per well of a 12-well plate. The 12-well plate was shaken horizontally at 60 rpm at 37°C. After 30 min, 3 hours, or 6 hours the surface was washed by removing the bacteria suspension and adding 2 mL 1% TSB in PBS. Then the surface was transferred to a 15 mL falcon tube containing 1 mL 1% TSB in PBS and sonicated for 5 min to remove attached bacteria. The obtained bacteria suspension was serially diluted (10^0, 10^{-1}, 10^{-2}, 10^{-3}, 10^{-4}, 10^{-5}, 10^{-6}) in PBS and 50 μL of each dilution was spotted in triplicate on LB-Agar plates. CFUs were counted after an overnight incubation at 37°C.

5.3.3 Cephalexin producing nanoreactors - active strategy

Cephalexin was detected by a sorbitol-zinc assay similar to the spectrocolorimetric assay developed by Bundgaard to quantify aminopenicillines.[297] Briefly, 20 % sorbitol in an 0.2 M carbonate (0.04 M Na_2CO_3, 0.16 M $NaHCO_3$) buffer containing 0.15 μg mL^{-1} Zn^{2+} ions at pH = 9.2 was prepared. A 50 μL sample was mixed with 50 μL sorbitol-zinc solution and heated at 60°C for 10 min while shaking horizontally (300 rpm). Then, NaOH solution (1 M, 50 μL) was added. After 10 min incubation at room temperature (rt) 130 μL of the mixture were added to a well of a 96-well plate for UV-Vis measurement on a SpectraMaxPlus 384 (Molecular Devices, Sunnyvale, USA).

Cephalexin, PGME, and 7-ADCA were identified by high performance liquid chromatography (HPLC). The sample was loaded onto a chromolith performance RP-18c 100-4.6 mm column and eluted by a 0.1 % TFA in ACN : water (15 : 85) isocratic gradient at a flow rate of 0.5 mL min^{-1} over 15 min. UV-Vis absorbance was simultaneously measured focusing on λ = 214 nm.

PA was coupled to Atto-488-NHS (Atto-Tec GmbH, Germany) overnight at 4°C. Free Atto-488-NHS was removed from labeled PA by dialysis against PBS using a 8-10 kDa dialysis membrane (Spectra/Por Biotech CE Tubing from spectraLabs.com).

Nanoreactors were self-assembled by thin film rehydration. 0.5 μmol of $PMOXA_6$-*b*-$PDMS_{43}$-*b*-$PMOXA_6$ in ethanol were mixed with 1 mol% azide-terminated $PMOXA_7$-*b*-

$PDMS_{40}$-*b*-$PMOXA_7$ and dried to a thin film by rotary evaporation under reduced pressure (150 mbar). The film was rehydrated with 1 mL of filtered PBS (Durapore membrane filters 0.45 μm HV, Merck) containing 2.2 mg PA, labeled PA, or HRP. The obtained suspension was stirred overnight at 4°C and then extruded 13 times through a 400 nm pore-size polycarbonate membrane (Nuclepore Trac-Etch membrane, Whatman®) on a 1 mL syringe extruder. Non-encapsulated enzyme was removed from polymersomes by size exclusion chromatography (SEC) on a Sepharose 2B column (length: 25 cm, diameter: 1 cm) connected to an ÄKTAprime system. The column was eluted with filtered PBS and the polymersome containing fraction detected at 280 nm. For CF encapsulated polymersomes, 50 mM CF in PBS was used for rehydration. OmpF was added to the polymer mixture before film formation to create OmpF permeabilized nanoreactors. Negative controls for OmpF permeabilized nanoreactors were prepared by adding dialysed OG instead of OmpF to the polymer. To obtain melitin permeabilized vesicles, melittin (20 μM) was added to the nanoreactors or CF encapsulated polymersomes immediatly before use.

For transmission electron microscopy (TEM), 5 μL nanoreactor suspension were adsorbed to a glow discharged formvar-coated copper grid (400 mesh) for one minute. Excess sample was blotted off and the grid washed twice with water and once with 2 % uranyl acetate before negative staining for 10 s with 2 % uranyl acetate. Dry grids were imaged with a Philips CM100 at an acceleration voltage of 80kV.

PA encapsulation was analyzed by fluorescence correlation spectroscopy (FCS) on a Zeiss LSM 510 META/Confocor2. 10 μL aliquots of Atto-488-NHS, Atto-488-labeled PA, and Atto-488-labeled PA encapsulated nanoreactors were placed on a glass slide (0.16-0.19 mm thickness) and excited at 488 nm with a Argon laser. Autocorrelation curves were recorded using a 40x water-immersion objective (Zeiss C/Apochromat, NA 1.2) and appropriate filter sets. The FCS autocorrelation curves were fitted with either a one component curve or a two-component curve where the diffusion time of the first fraction was fixed to the one obtained for free dye or Atto-488-labeled PA. The fitting was conducted as previously described.[93] Additionally, giant unilamellar vesicles (GUVs) with encapsulated Atto-488-labeled PA were prepared as follows. 30 μL ethanol containing 30 nmol $PMOXA_6$-*b*-$PDMS_{43}$-*b*-$PMOXA_6$ and 0.3 nmol azide terminated $PMOXA_7$-*b*-$PDMS_{40}$-*b*-$PMOXA_7$ was added to a plasma cleaned glass vial (2.5 mL) and dried under vacuum to a thin film. Then, 250 μL sucrose (300 mM) containing Atto-488-labeled PA (2.2 mg mL^{-1}) were added and pipetted up and down 4 times to induce GUV formation. GUV preparations were stored at 4°C until further use. For confocal laser scanning microscopy (CLSM), the GUV membranes were stained with Bodipy630/650 (50 nM). GUVs were imaged at 20 °C using a water immersion objective (C-Apochromat 40x/1.2W Korr FCS M27) with an excitation wavelength of 488 nm and 633 nm (each 1 % laser power) and a mean beam splitter (488/561/633). The pinhole was set to 1 airy unit and the gain to 750 and 500 for the 488 and the 633 channel, respectively. Fluorescence was tracked from 499 - 629 nm (Atto-488-labeled PA) and 638 - 737 nm (Bodipy). Fluorescent images were processed with Fiji.

Cephalexin production was studied using the sorbitol zinc-assay described above. In brief, 7-ADCA and PGME were mixed in PBS to a concentration of 66 mM and 33 mM, respectively. The pH of the mixture was adjusted to 6.5 and then added to either free PA or PA encapsulated nanoreactors. The enzymatic reaction was allowed to proceed for different

periods of time.

The functional insertion of OmpF in nanoreactor membranes was examined by measuring the enzymatic activity of encapsulated HRP. 500 μL TMB (substrate) were mixed with 500 μL PBS and 5 μL H_2O_2. 200 μL of this substrate solution were added to 5 μL HRP encapsulated nanoreactors permeabilized with OmpF in a well of a 96-well plate and the absorbance was measured at $\lambda = 370$ nm for 20 min.

To test the permeability of CF encapsulated polymersomes with and without melittin, the fluorescence at $\lambda_{Ex} = 495$ nm and $\lambda_{Em} = 519$ nm was recorded on a spectrafluorometer FP-8200 from Jasco over 4 hours. 10 μL untreated polymersome suspension was added to 2990 μL PBS in a cuvette and the baseline was monitored. After 20 min, melittin (20 μM) was added and at 3 hours 50 min, 5 μL Triton X-100 (10 % stock solution) were added to solubilize the membrane and obtain 100 % permeability.

5.4 Results and Discussion

5.4.1 Microstructured surface - passive strategy

To find a passive antimicrobial microstructured surface, several materials prepared by the research group of Prof. Dr. Jian Xu from the Chinese Academy of Science in Beijing were tested for their antimicrobial properties. First, polypropylene (PP) and cotton gauze based materials were tested using the JIS test. A drop of *E. coli* inoculum was placed on the respective surface and covered with a parafilm to prevent it from drying out. After overnight incubation at 37°C the surface including the drop and the parafilm piece were added to PBS and sonicated to resuspend all bacteria. CFUs of serial dilutions plated on LB-agar plates were counted the next day (**Figure 5.2A**). As expected, the material modified with AgNPs (B2) shows the best performance and no CFUs could be detected, while on non-modified PP (B0, C0) and polymer crystal modified PP (C1) surfaces the most CFUs were counted. The wettability of the different surfaces was characterized by water contact angle measurements. All surfaces showed a similar hydrophobicity slightly below 150° water contact angle. Only the non-modified cotton gauze was extremely hydrophilic and immediately absorbed the water drop, resulting in a water contact angle of 0° (**Figure 5.2B**).

The second, microstructured surfaces from Professor Xu's group consisted of organosilica microparticles adsorbed on glass or silica surfaces. The diameters of the microparticles were 1 μm, 2 μm, and 5 μm. Upon arrival at the University of Basel, the surfaces were immediately characterized and tested for their passive antimicrobial behavior. SEM analysis (**Figure 5.3**) revealed that there were fewer particles on the glass surface than of the silica, especially in the case of particles with 1 μm in diameter. Silica surfaces appeared to be more robust as more particles stayed adsorbed during the shipping. However, the silica surfaces did change during the shipping as well. There were less homogeneous as when imaged in Beijing before the shipping. Some particles detached as visible on SEM pictures as light rings, where organosilica particles were most likely adsorbed to the surface previously (**Figure 5.4A**). In some areas the surface was covered relatively homogeneously with one layer of particles (**Figure 5.4B**), but in other areas the particles got stacked creating several layers (**Figure 5.4C**). AFM of the silica surface covered with 1 μm sized particles

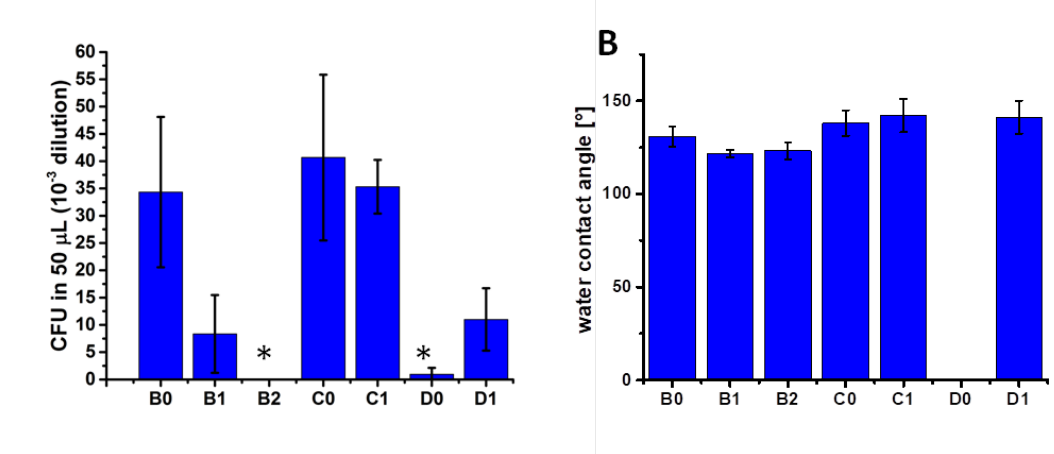

Figure 5.2: A) *E. coli* CFU count on polypropylene (PP) non woven-fabrics modified with polydopamine (B1), polydopamine and AgNPs (B2), polymer crystal (C1) and cotton cause modified with paraffin wax (D1). The corresponding '0' surfaces are the non-modified control samples. The $\star$ indicates statistical significance ($p < 0.05$, n=3) in relation to B0, in accordance to the t-test. B) Water contact angle measurements of the surfaces tested in A.

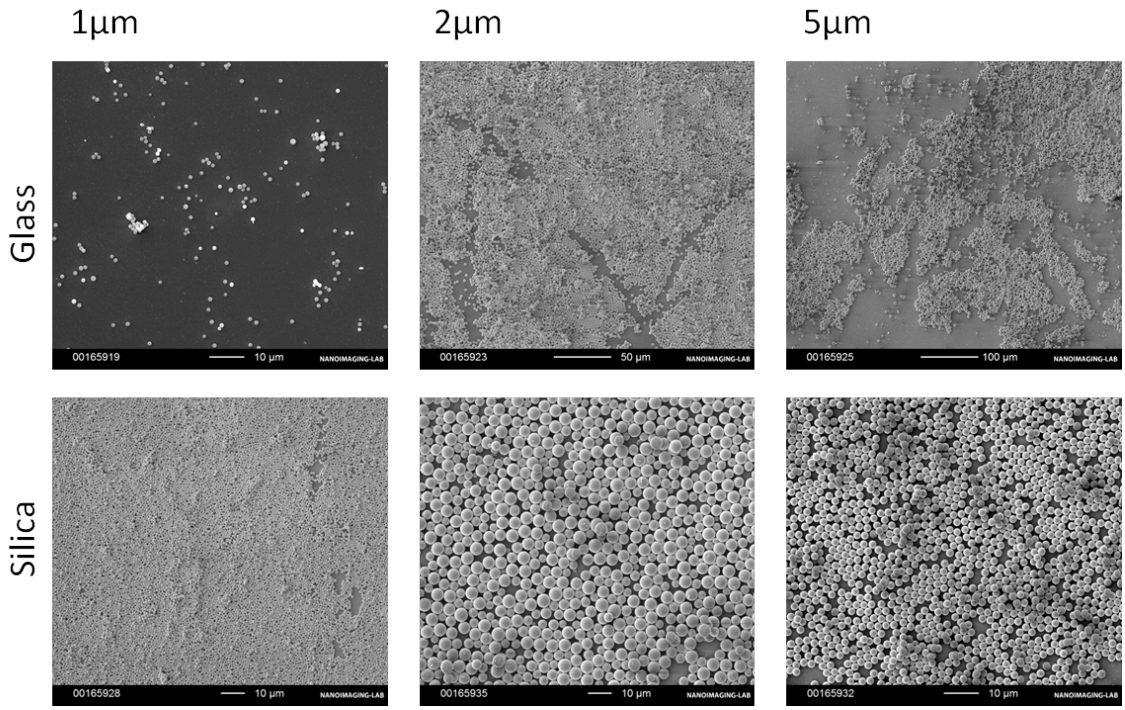

Figure 5.3: SEM of microstructured surfaces: organosilica microparticles (diameters: 1 μm, 2 μm, and 5 μm) adsorbed on glass (upper panels) and on silica (lower panels).

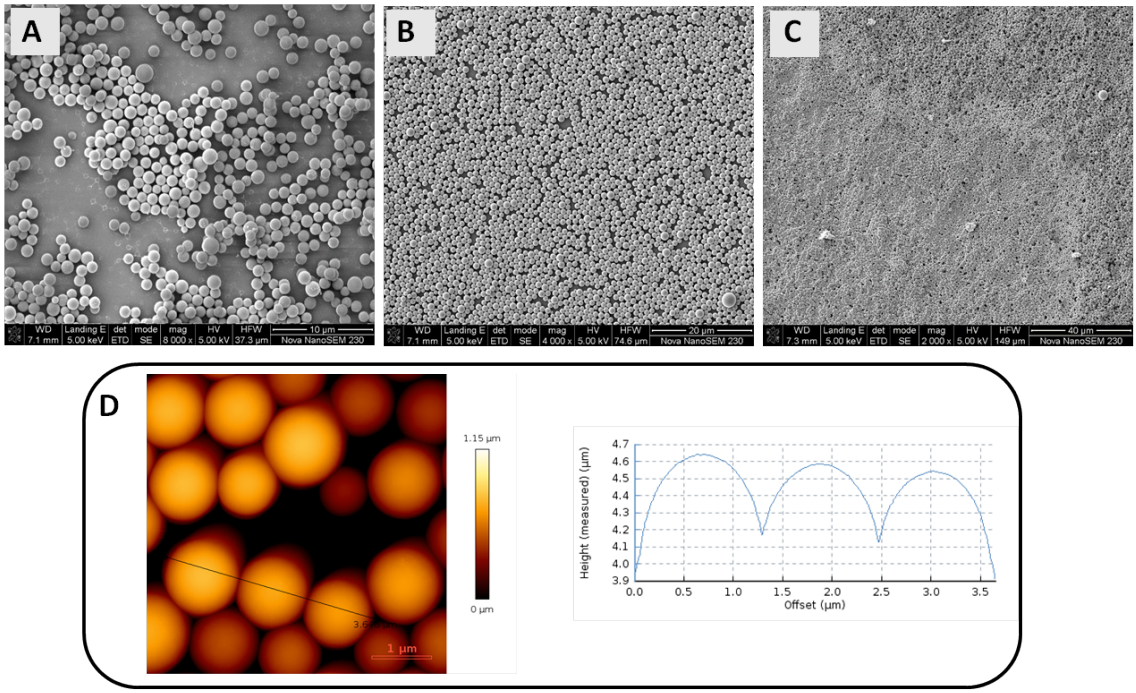

Figure 5.4: A-C) SEM of 1 μm organosilica particles adsorbed to a silica surface at different magnifications. D) AFM image of the height channel of 1 μm organosilica particles adsorbed to silica surface (left panel). The height profile along the black line is shown on the right.

confirmed the size and spherical structure of the particles on the surface (**Figure 5.4D**). Finally, the passive antimicrobial activity was tested by studying bacterial attachment. The microstructured surfaces created with the different sized organosilica microparticles were compared to non-, NH_2-, or DBCO-functionalized silica surfaces or nanostructured surfaces created by the SPAAC immobilization (described in chapter 3) of soft, spherical polymersomes. For testing attachment, the surfaces were immersed in an *E. coli* inoculum and incubated while shaking horizontally for 30 min, 3 h, or 6 h at 37 °C. To quantify bacterial adhesion, the surfaces were transferred to fresh PBS and sonicated to resuspend the attached bacteria. The bacteria suspension was plated on LB-Agar plates, where the CFUs were counted the next day (**Figure 5.5**). At 6 hours of immersion during which the bacteria had time to adhere, the antibacterial properties of the different surfaces varied. DBCO functionalized silica surfaces reduced bacterial attachment compared to non-functionalized silica surfaces. The microstructured surface with 5 μm sized organisilica particles clearly reduced bacterial attachment when compared to all other surfaces at 6 hours. The least significance with $p = 0.07$ is obtained when it was compared to nanostructured surfaces with immobilized polymersomes. On the other hand, the data comparison was enlarged to the shorter immersion times, where the 5 μm sized organisilica particles still showed significantly less bacterial attachment when compared to the amino functionalized silica surface immersed for only 3 hours ($p = 0.04$).

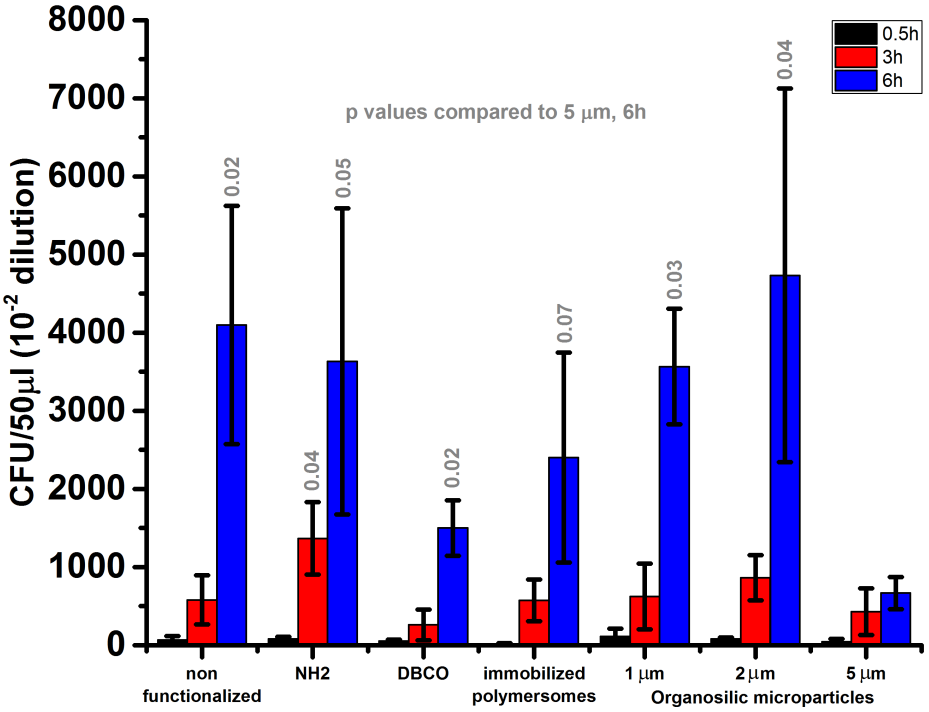

Figure 5.5: Bacterial attachment study. Surfaces were immersed in an *E. coli* inoculum ($5{\cdot}10^7$ CFU mL^{-1}). The surfaces were sonicated in PBS to resuspend surface attached bacteria. This bacteria suspension was collected and plated on LB-agar plates at different dilutions for CFU counting. The black bars represent 0.5 h, the red bars 3 h, and the blue bars 6 h immersion in the *E. coli* inoculum. The p values obtained by the student t-test from comparison to the 5 μm organosilica particle surface are indicated in grey. (n=3)

5.4.2 Cephalexin producing nanoreactors - active strategy

The active strategy was pursued by designing a cephalexin producing nanoreactor based on $PMOXA_6$-*b*-$PDMS_{43}$-*b*-$PMOXA_6$ mixed together with azide-terminated $PMOXA_7$-*b*-$PDMS_{40}$-*b*-$PMOXA_7$ triblock copolymer for future immobilization on the microstructured surface. The antibiotic cephalexin can be enzymatically produced *in situ* by PA. First, a method to detect cephalexin independent of the substrates PGME and 7-ADCA was applied. A colorimetric method to quantify aminopenicillins which contain, apart from the β-lactamring, an amino side chain (**Figure 5.6**, marked in red) was developed by Bundgaard.[297] The reaction involves heating the reaction in an alkaline buffer containing sorbitol and zinc(II)-cations that catalyse the degradation of penicillines. In Bungaard's study ampicillin **(1)** forms with sorbitol the corresponding penicilloyl ester, the α-aminobenzylpenicilloyl ester **(2)**. This ester undergoes intramolecular aminolysis to form a piperazine-2,5-dione derivative **(3)**. Like ampicillin, Cephalexin **(4)** has a β-lactamring with an amino side chain that is required to undergo esterification and subsequent intramolecular aminolysis to form a piperazine-2,5-dione derivative **(6)**. This derivative has

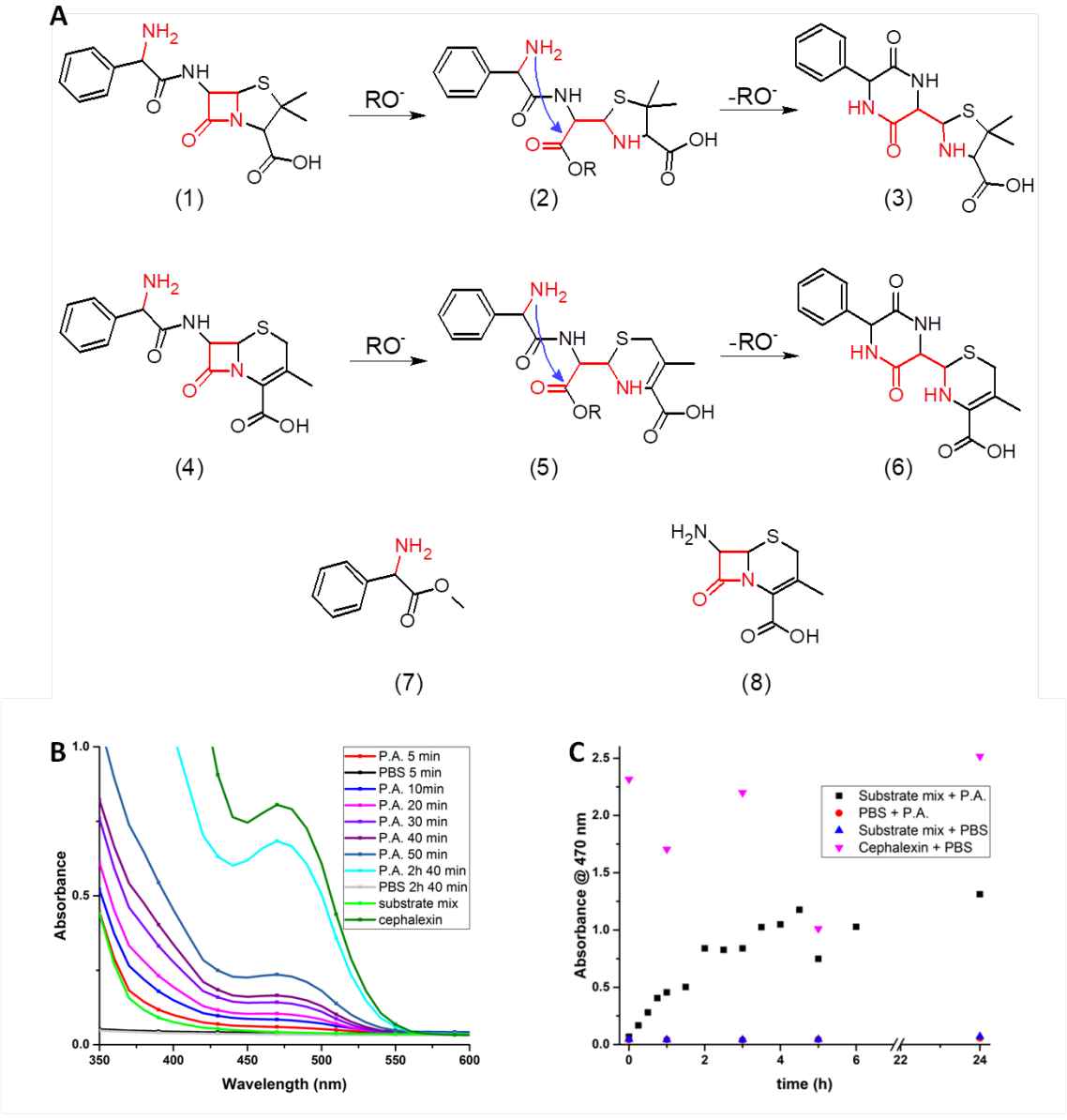

Figure 5.6: A) Scheme of Ampicillin **(1)** and Cephalexin **(4)** reacting with sorbitol (RO^-) to the corresponding esters **(2 and 5)**, which after intramolecular aminolysis form piperazine-2,5-dione derivatives **(3 and 6)**. B and C) Detection of enzymatic cephalexin production by the sorbitol-zinc colorimetric assay. B) Absorbance spectra form 350 nm - 600 nm. The negative controls are PBS alone (black and light grey at different time points) and the substrate mix (PGME **(7)** and 7-ADCA **(8)**) with only PBS (light green). The positive control is cephalexin in PBS (olive). The other recordings represent the substrate mix with PA in PBS with different incubation times. C) Absorbance at 470 nm over the course of 24 hours of the enzymatic cephalexin production (black), PBS mixed with only PA (red) or only the substrate mix without enzyme (blue) as negative controls, and cephalexin alone as positive control (pink).

an absorbance maximum around λ = 470 nm (**Figure 5.6**). When the substrate mix (consisting of PGME and 7-ADCA) was incubated with PA, the reaction with sorbitol and zinc(II)-cations produced a color change to yellow that was accompanied by an absorbance at 470 nm. After 10 min of incubation, a slight increase in absorbance over the negative controls was observed, (**Figure 5.6A**) indicating the PA catalyzed condensation of PGME and 7-ADCA to cephalexin. After about 5 hours, the cephalexin production reached a plateau and only marginally increased from then on (**Figure 5.6B**). However, no colorimetric effect was detected for the negative control where sorbitol and zinc were incubated with the substrate mix. This is due to the molecular separation of the two required moieties: the β-lactamring is only present in 7-ADCA while the amino side chain only in PGME. Similarly, the enzyme PA alone did not produce a color change.

HPLC offers another way to distinguish cephalexin from PGME and 7-ADCA.[286,298] When 5 μg of each compound were injected on the analytical column (chromolith performance RP-18c 100-4.6 mm) with a mobile phase of 85% water, 15% ACN, and 0.1% TFA, cephalexin showed the longest retention time while the educts PGME and 7-ADCA were eluted earlier and close to each other (**Figure 5.7A**). Decreasing the flow rate by half approximately doubled the corresponding retention times and therefore, the separation between the educts and cephalexin increased. Enzymatic cephalexin production was also monitored by HPLC (**Figure 5.7B**). Heating to 80°C, in order to stop the reaction by inactivating the enzyme at specific time points, did not affect the peaks. Again, after 10 min reaction time a small peak for cephalexin was detected, proofing the enzymatic production of cephalexin by PA.

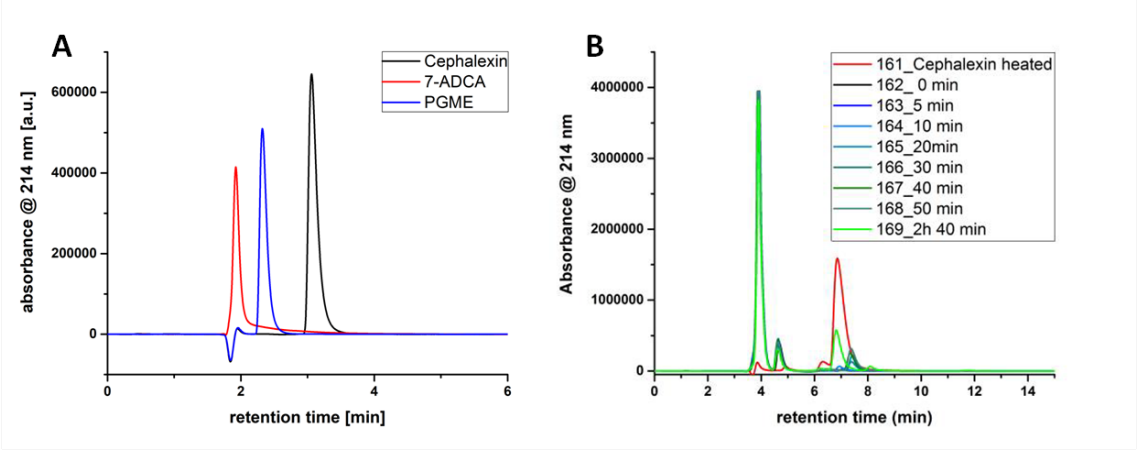

Figure 5.7: A) Injection of 5 μg cephalexin (black), 7-ADCA (red) and PGME (blue). Flow rate: 1 mL min^{-1} B) Reaction mixtures after different reaction times. The reaction was stopped by heating the reaction mixture to 80°C. Cephalexin alone, as a positive control, was injected after heating to 80°C. Flow rate: 0.5 mL min^{-1}

The enzymatic production of cephalexin could be followed by both detection methods. The advantage of HPLC is that besides cephalexin, residual substrates can be individually detected and only little sample volumes are needed. However, HPLC is too time consuming when many samples have to be tested and generates lots of solvent waste. The sorbitol-zinc assay on the other hand requires larger sample volumes but many samples

can be tested in parallel generating less solvent waste. Taking these considerations into account, further analyses were generally done by the sorbitol-zinc assay.

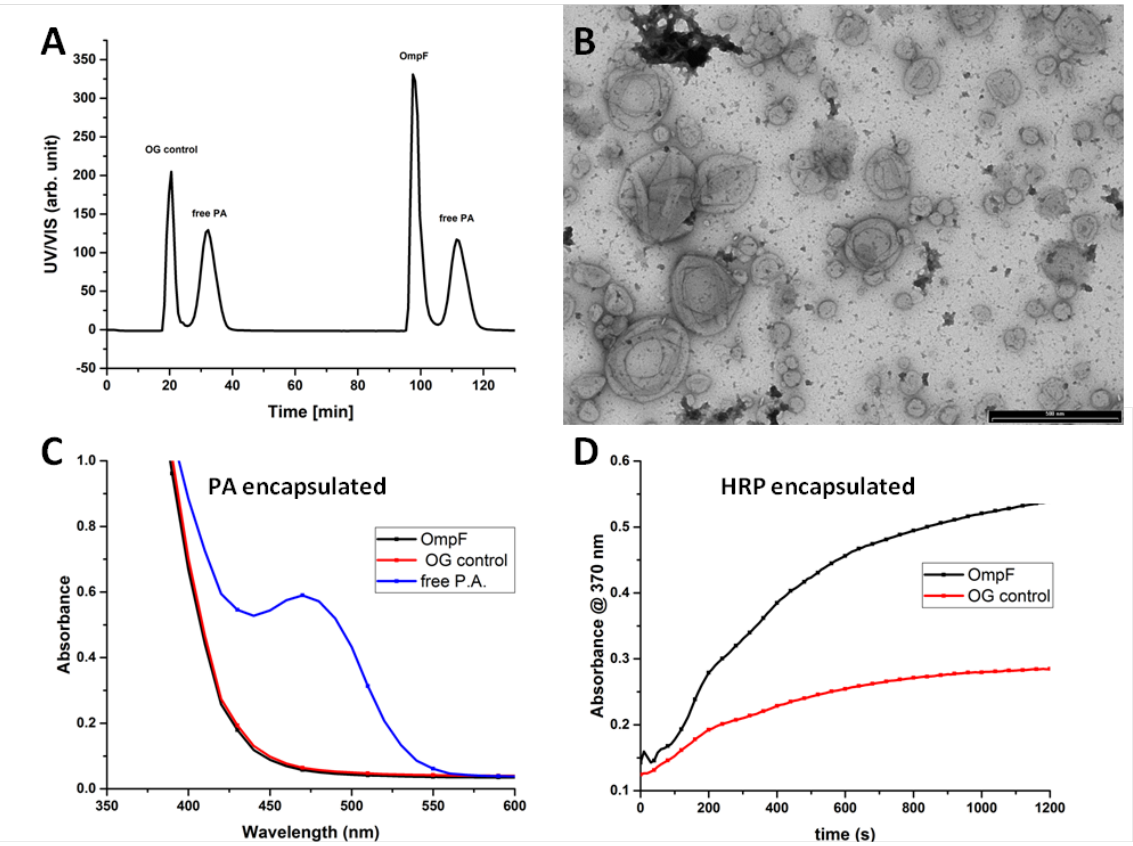

Figure 5.8: A) SEC of PA encapsulated nanoreactors with OmpF (OmpF) and witout OmpF (OG control) to separate them from non-encapsulated PA (free PA). B) TEM of PA encapsulated nanoreactors, scale bar: 500 nm. C) Sorbitol-zinc assay of PA encapsulated nanoreactors with OmpF (black), and without OmpF (OG control) (red), and free PA eluate from SEC (blue). D) HRP activity assay of HRP encapsulated nanoreactors with OmpF (black) and without OmpF (OG control) (red).

As a next step towards the *in situ* production of cephalexin, nanoreactors were self-assembled in the presence of PA by thin film rehydration. To prepare nanoreactors that lend themselves to immobilization by the SPAAC reaction[222] a thin film of $PMOXA_6$-*b*-$PDMS_{43}$-*b*-$PMOXA_6$ mixed with azide terminated $PMOXA_7$-*b*-$PDMS_{40}$-*b*-$PMOXA_7$ polymers were prepared. After film rehydration in PBS in the presence of PA, self-assembled nanoreactors were purified from non-encapsulated PA by extrusion and SEC (**Figure 5.8A**). The nanoreactor membrane enclosing the PA needs to be made permeable to PGME, 7-ADCA and cephalexin. Therefore, OmpF was incorporated. Purified OmpF is solubilized in 3% OG which interferes with the self-assembly of the polymersomes. Thus, the detergent was reduced to a minimum by dialysis against PBS prior to adding the OmpF to the polymer solution used for film formation. Because residual OG could still influence self-assembly, a 3% OG solution was dialysed in parallel against PBS and added as control in corresponding polymersome preparations (OG control). TEM micrographs confirmed the vesicular structure of the nanoreactors and the OG control polymersomes

(**Figure 5.8B**). More force was needed for the extrusion of PA encapsulated nanoreactors compared to the pure polymersomes self-assembled in chapter 3. Because sometimes it was not possible to extrude through 200 nm membranes, samples were mostly extruded through 400 nm.

To study PA encapsulation, the enzyme was labeled with Atto488-NHS and encapsulated in polymersomes and GUVs assembled with 1 mol% azide-terminated polymer (**Figure 5.9**). Due to their size, GUVs can be examined by CLSM. Bodipy, a hydrophobic fluorophore that non-specifically interacts with membranes, was used to visualize the hydrophobic polymer membranes (**Figure 5.9A, middle**). Atto-488 labeled PA was detected in the green channel. Corresponding fluorescence images showed that PA did not specifically interact with the GUV membrane but is evenly distributed throughout the GUV's cavity (**Figure 5.9A, left**). PA encapsulation in polymersomes was quantified by FCS (**Figure 5.9B** and **Table 5.1**). FCS autocorrelation curves of free Atto488-NHS (black curve) compared to Atto-488 labeled PA (blue curve) showed an shift to higher diffusion times for the labeled enzyme. The fitting showed that about half of the dye was attached to the enzyme while the other half was still free in solution. Higher diffusion times indicate that the fluorescent species diffuses across the confocal volume at lower speed and thus, represents a slow moving, i.e. bigger/heavier molecule or particle. Comparing the counts per molecule (CPM) of samples with a comparable count rate (CR) allowed the calculation of the number of dye molecules per PA or the number of encapsulated PA molecules (**Table 5.1**). Corresponding calculations revealed 1-2 dye molecules per labeled PA. As expected, encapsulation of labeled PA in polymersomes resulted in a clear shift to higher diffusion times. This slow diffusing fraction was close to 100%, indicating good purification after encapsulation resulting in very low non-encapsulated labeld PA left in solution. On average, each N_3 exposing polymersomes had encapsulated 30 labeled PA molecules.

	CPM [kHz]	CR [kHz]	τ_D [μs]	Fraction [%]
Atto-488 NHS	0.9 ± 0.2	43 ± 2	64 ± 20	100
Labeled PA	1.3 ± 0.2	27 ± 2	385 ± 243	51
encapsulated labeled PA	38.5 ± 17	27 ± 3	13638 ± 3533	99

Table 5.1: FCS fitting parameters to estimate PA encapsulation efficiency.

To test the activity of PA encapsulated in nanoreactors, the *in situ* production of cephalexin was analyzed by the sorbitol-zinc assay. The free PA fraction collected from SEC purification of the nanoreactors (**Figure 5.8A**) responded to the sorbitol-zinc treatment with a clear color change, demonstrating that the enzyme stayed active during nanoreactor formation and purification (**Figure 5.8C**). The membrane permeabilization by OmpF reconstitution was tested with established HPR nanoreactors that were prepared in parallel to the PA nanoreactors using the same mixture of polymers. While HRP nanoreactors showed increased absorbance, hence activity, over control nanoreactors without OmpF (OG control) after adding the substrates for the HRP reaction (TMB and H_2O_2, **Figure 5.8D**) OmpF permeabilized PA nanoreactors did not show activity. Only when free PA was present, the absorbance peak at $\lambda = 470$ nm occurred. After different preparation methods failed to produce functional PA nanoreactors, other ways to render the mem-

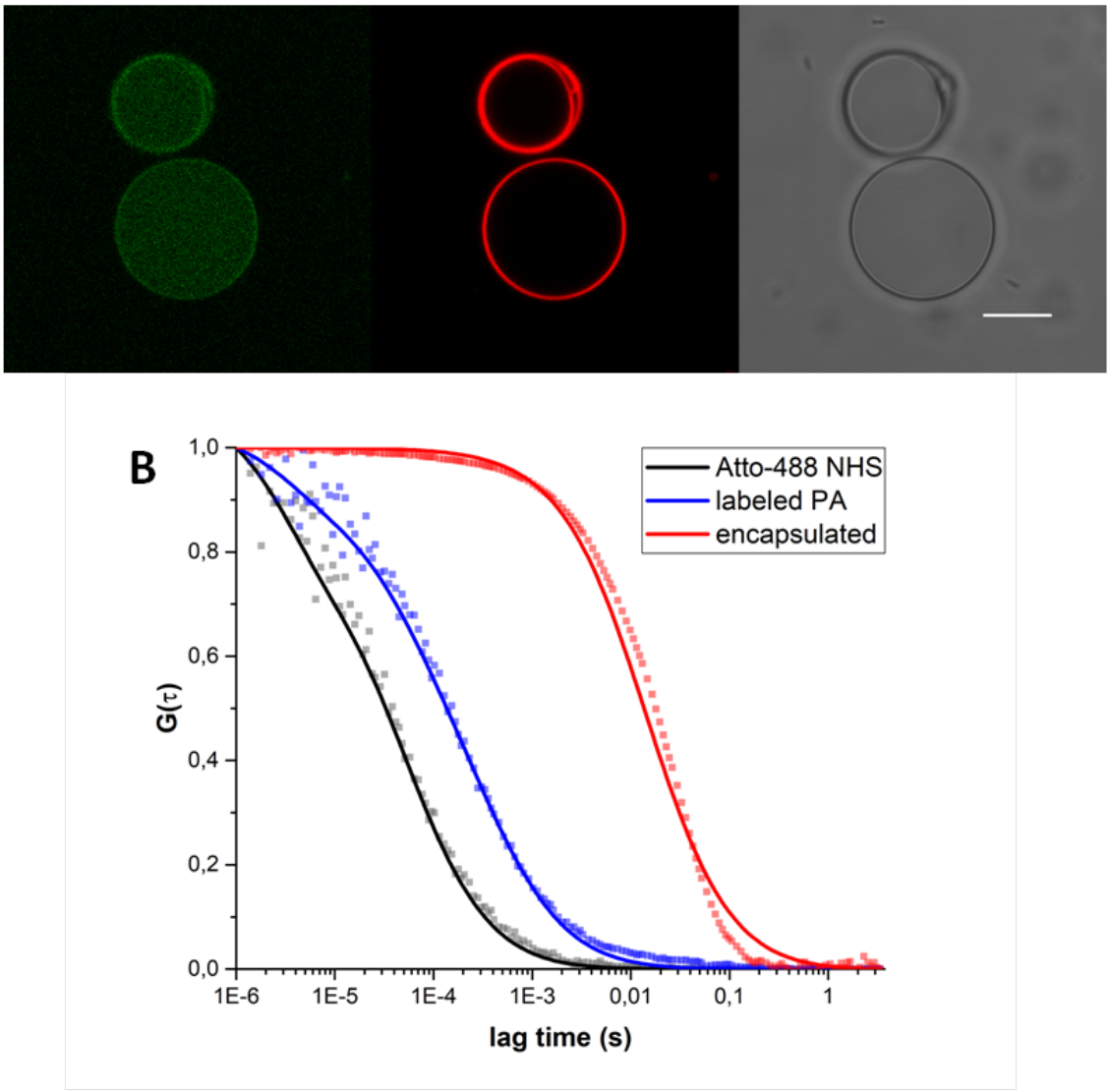

Figure 5.9: A) CLSM of 1 mol% N_3 exposing GUVs with encapsulated Atto488-PA. The membrane was stained with Bodipy. Left: green channel revealing Atto-488-PA, middle: red channel showing Bodipy630/650, right: bright field image B) Normalized FCS autocorrelation curves of free Atto-488-NHS (black), Atto-488 labeled PA (blue), Atto-488-labeled PA encapsulated in polymersomes (red). Raw data are represented by squares while the fitted autocorrelation curves by a solid line.

branes permeable were sought.

Melittin, a peptide present in bee toxin, was tested for its ability to form functional pores in PA encapsulated polymersomes. Because CF has a similar molecular weight to cephalexin, it was chosen as a model molecule to monitor melittin-mediated permeabilization. First, CF encapsulated polymersomes were used to study membrane permeabilization by melittin (**Figure 5.10A**). At high concentrations, encpasulated CF is self quenching, but when diluted (i.e. able to diffuse out of the polymersome) it dequenches and fluorescence occurs.[272] As shown in Figure 5.10A, the addition of melittin to a final concentration of

20 μM nearly instantly permeabilized 90 $\pm$ 4 % of CF encapsulated polymersomes (black lines). Because melittin was dissolved in ethanol, control experiments were performed with the corresponding volume of ethanol added to the polymersomes (red lines). In this case only 5 $\pm$ 4 % of the polymersomes were permeabilized. Hence, the permeabilization is mainly caused by the melittin and not by the ethanol.

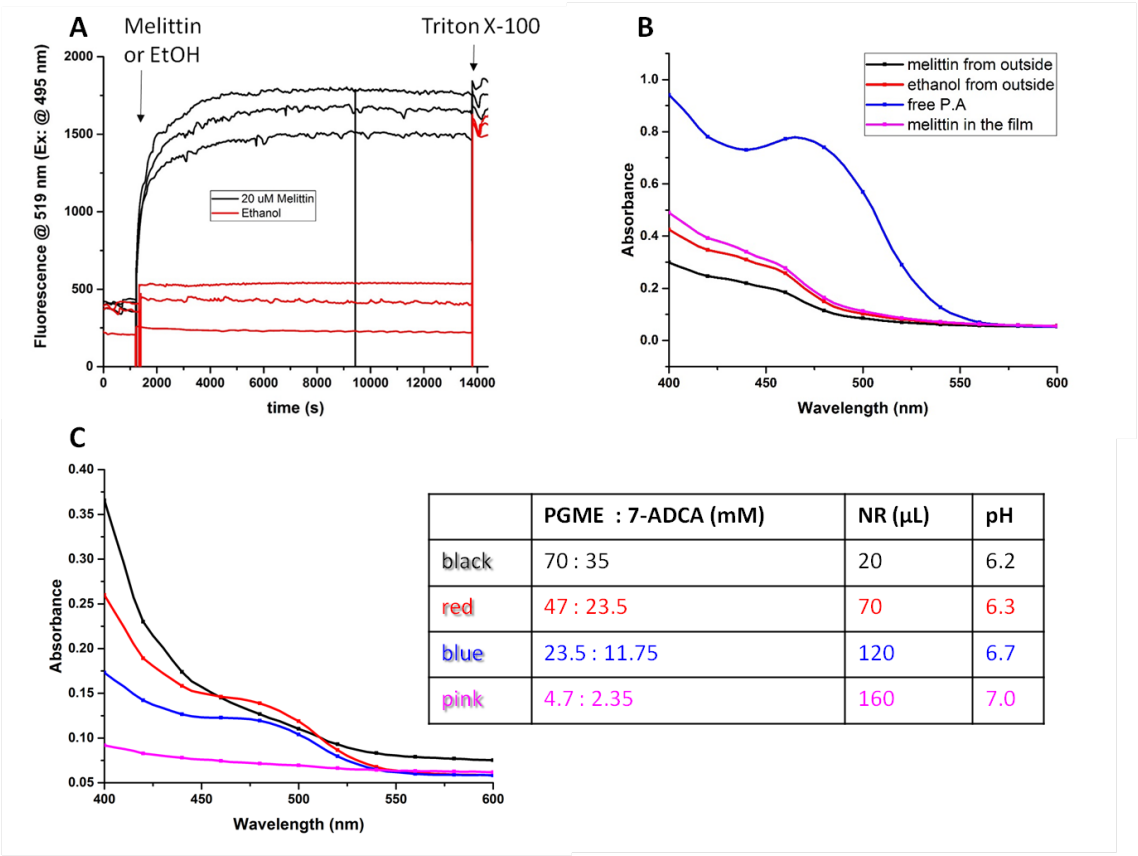

	PGME : 7-ADCA (mM)	NR (µL)	pH
black	70 : 35	20	6.2
red	47 : 23.5	70	6.3
blue	23.5 : 11.75	120	6.7
pink	4.7 : 2.35	160	7.0

Figure 5.10: A) Permeabilization of CF encapsulated polymersomes by melittin. After 20 min of equilibration, melittin (20 μM final concentration, black lines) or the same volume of ethanol (1% final concentration, red lines) was added. After 3 hours and 40 min Triton X-100 is added to completely solubilize the polymersome membranes. B) Sorbitol-zinc activity assay of PA nanoreactors. Only the free PA showed an absorbance peak around 470 nm while nanoreactors to which melittin or ethanol were added from the outside as well as nanoreactors with melittin added during film formation did not. C) Sorbitol-zinc activity assay of Triton X-100 lysed PA nanoreactors. The total reaction volume was constant while the substrate and nanoreactor (NR) concentration was changed.

To further explore melittin as permeablization agent, melittin (black line) or corresponding volumes of ethanol (red line) was added to the outside of the PA encapsulated polymersomes. In addition melittin was also added during film rehydration (pink line) to create melittin pores already during self-assembly (**Figure 5.10B**). In addition, free PA obtained by collecting the PA fraction from SEC purification served as a positive control (blue line). Absorbance at λ = 470 nm indicated that the free PA catalyzed cephalexin production. In contrast, similar to the negative control (EtOH), addition of melittin from the outside

or during film rehydration did not lead to a color change suggesting that there was no cephalexin production by the nanoreactors.

To assess if enough nanoreactors with enough PA are in the mixture, different volumes of nanoreactor solution in which the nanoreactors were completely lysed with 5 μL Triton X-100 were mixed with different volumes of the substrate solution. The total volume was kept constant at 175 μL (**Figure 5.10C**). The presence of only 20 μL of nanoreactors seemed too little to obtain a detectable color change. Similarly, 160 μL nanoreactor with 4.7 μM PGME and 2.35 μM 7-ADCA did not yield a color change, suggesting a too small amount of substrate. However, successful cephalexin production was detected after sorbitol-zinc treatment when 70 - 120 μL lysed nanoreactor solution were incubated with 23.5 - 47 μM PGME and 11.75 - 23.5 μM 7-ADCA.

5.5 Conclusions

The microstructured surface with 5 μm sized organosilica microparticles adsorbed on silica showed the most promising passive antimicrobial behavior. Two independent methods, a fast colorimetric method involving sorbitol and zinc and HPLC, were found to be suitable to detect cephalexin. The fast sorbitol zinc assay is practical to screen many different parameters to design the nanoreactors. Having a working system, the HPLC, which is more time consuming, offers the possibility to quantitatively monitor all substrates simultaneously. PA was encapsulated in polymersomes where it kept its activity. However, for PA encapsulated nanoreactors that were permeabilized by OmpF or melittin cephalexin production could not be detected. The issue could not be found in the OmpF reconstitution or melittin permeabilization. HRP encapsulated nanoreactors self-assembled from the same polymers allowed the diffusion of the corresponding substrates (i.e.: TMB and H_2O_2) through OmpF. CF, even having a slightly higher molecular weight than cephalexin, was able to pass through the membrane of CF encapsulated polymersomes self-assembled from the same polymers upon melittin addition. This led to the conclusion that either the substrates PGME or 7-ADCA or the antibiotic cephalexin, or a combination thereof, could not pass through the OmpF and melittin pore. Therefore, other permeabilization techniques need to be found which allow the passage of cephalexin, PGME, and 7-ADCA through the nanoreactors membrane.

Chapter 6

General conclusions and Outlook

Antibiotic resistance is a term that is gaining attention, visible in the general public by regular newspaper or TV-channel reports. The future outlook does not look bright. Antibiotic overuse favors antibiotic resistance, which is a threat to our achieved medical improvements over the last century. So far easily curable infections can again become life-threatening and surgeries would come with a higher risk due to possible exposure to antibiotic resistant bacteria. The demand and need to find new antibiotics, new ways, and new strategies to fight bacteria infections is indisputable. This global need gave the motivation for this thesis in which possible new ways and strategies were researched. Particularly, the coimmobilization of polymeric nano-assemblies on a solid support as well as the decoration with an antimicrobial peptide was studied and characterized by their physical chemical properties as well as their antibacterial performance. This thesis describes the self-assembly of PMOXA-PDMS-PMOXA block copolymers. A new and easy polymersome-immobilization technique has been developed with the already known SPAAC reaction avoiding possible toxic catalysts. Coimmobilization was obtained by the simultaneous immobilization of polymeric nanostructures by the SPAAC reaction and the established thiol-ene immobilization reaction. Furthermore, patterns were created by micro-contact printing polymersomes onto a solid support. The immobilization was studied by a combination of SEM, AFM, and LSM. A possible next step would be to load different antibiotic agents into the immobilized polymersomes and micelles. The antibiotics would be released when needed by an external trigger (e.g., UV) or internal trigger (e.g, pH, temperature, enzymes) by incorporating a unit sensitive to the trigger in the polymersomes or micelles. Having a nanostructured surface created by the immobilization of the nano-assemblies with multiple loaded antibiotics could help the fight against bacteria through the local release of antibiotic where needed which also might reduce the used amount of antibiotics.

To decorate immobilized micelles with antimicrobial activity, the AMP KYE28 was chosen. The synthesis of the AMP was optimized on a microwave assisted peptide synthesizer and the thiol-maleimide Michael addition, as an additional micelle immobilization technique, was studied. A nanostructured surface was obtained by the immobilzation of micelles. This surface reduced bacteria growth on it and therefore, displayed a passive antimicrobial strategy. The synthesized KYE28 was characterized for its antimicrobial properties (i.e. the MIC and MBC) and represents an active antimicrobial strategy. These two strategies were combined by adding the AMP on the nanostructured surfaces, decorating the immobilized micelles which further reduced bacterial growth on the surface. These

surfaces were thoroughly characterized by a combination of AFM, LSM, XPS, and QCM-D for their physical chemical properties. The lyophilized peptide has been shown to be stable over at least 1.5 years. However, the next step would be to evaluate the long-term stability of the AMP on the surface as well as release properties. Therefore, the surface's performance would need to be evaluated under various conditions (e.g., pH, temperature, ionic strength). Further research could study the micelle decoration with a combination of different AMPs for synergistic antimicrobial or anti-infection properties.

Additional research for the combination of active and passive strategies has been done. The collaborating research group of Prof. Jian Xu developed microstructured surfaces as passive antimicrobial surfaces. The antimicrobial test performed suggested the surface with adsorbed 5 μm sized particles to be most effective. Furthermore, we studied cephalexin producing nanoreactors as the active strategy to create smart antimicrobial surfaces by its immobilization onto the microstructured surface designed by the collaborating research group. The cephalexin producing enzyme PA has been encapsulated into the aqueous lumen of the polymersomes as proven by FCS and LSM studies. High enough PA concentration has been encapsulated for cephalexin production. However OmpF or melittin was not suitable to allow the passage of either the produced cephalexin or the needed educts (i.e., PGME and 7-ADCA) through the membrane. Nevertheless, OmpF and melittin were successfully reconstituted into the polymersome membrane as shown by the active HRP encapsulated nanoreactor or the release of CF from CF encapsulated polymersomes, respectively. As a future step, the nanoreactor would need to be further optimized with other permeabilization techniques to be found.

Overall, the aim of the thesis has been achieved. A passive and active antibacterial strategy have been combined by the immobilization of polymeric micelles with further decoration by the active AMP KYE28. This designed antibacterial surface acts locally. However, a smart antibacterial surface including triggered release and production of antibiotics could not be finished.

A question which has to be answered when developing such surfaces for any biomedical application is about the sterilization: How can these surfaces be sterilized or kept sterile without destroying the polymeric self-assembled structures and maintaining the active module (i.e, enzyme, peptide, antibiotic) intact? As a further step for all surfaces, these questions must be addressed. Sterilization with ethanol is not an option as the polymeric assemblies are not stable in ethanol. UV-irradiation might be a possible sterilization method for certain polymers and active agents. Additional sterilization methods have to be researched and studied.

Surfaces consisting of immobilized soft polymeric nano-assemblies combined with active agents as studied within this thesis are build in a straight forward modular way. This allows high versatility and easy adaption to various bacterial threats through coimmobilization of different antibiotic loaded self-assembled structures or the decoration with several amphiphilic AMPs or other potent peptides. Such surfaces are promising in future applications of wound healing concepts, where the surface supports the would healing locally. Furthermore such a surface could also be developed for contact lenses where its main task is to protect the lens from bacteria colonization and biofilm formation and therefore the eye from infection. Here the surface would be applied preventive with the

aim to never obtain an infection while in the former mentioned wound healing application it would only be applied when there is already a wound that needs protection and support to heal. In both suggested applications the surface acts locally from the outside of the body while being in contact with a humid environment either of the ichor or the tear fluid. Additionally, the surface could also be applied on urinary catheters where the surface is in contact with soft tissue and urine. Here, the surface would be applied on a device which is temporary placed in the body. The surface would further regularly be flushed with urine able to removed the on the surface killed bacteria by flushing them out.

List of abbreviations

6-Cl-HOBt	1-Hydroxy-6-chloro-benzotriazole
7-ADCA	7-aminodesacetoxycephalosporanic acid
ACN	acetonitrile
AFM	atomic force microscopy
AgNP	silver nanoparticle
AMP	antimicrobial peptide
APTES	(3-aminopropyl)triethoxysilane
APTS	aminopropyl trimethoxysilane
ATR-FTIR	Attenuated total reflection-Fourier transformed infrared
ATRP	atom transfer radical polymerization
B. thailandensis	Burkholderia thailandensis
CF	carboxyfluoerescein
CFU	colony forming units
clavA	clavanin A
CLSM	confocal laser scanning microscopy
CMC	critical micelle concentration
CPM	counts per molecule
CR	count rate
CuAAC	copper (I) catalyzed alkyne azide click
CVC	central venous catheter
Đ	dispersity
DAI	device associated infection
DBCO	dibenzocyclooctyne
DCC	dicyclohexylcarbodiimide
DCM	dichloromethane
DF-PEG	dibenzaldehyde-functionalized polyethylene glycol
DIC	N,N'-Diisopropylcarbodiimide
DIEA	diisopropylethylamine
DLS	dynamic light scattering
DMF	N,N-dimethylformamide
DMSA	dimercaptosuccinic acid
DMSO	dimethylsulfoxid
DNA	deoxyribonucleic acid
DOPE	1,2-dioleoyl-sn-glycero-3-phosphoethanolamine
DOPG	1,2-dioleoyl-sn-glycero-3-phosphoglycerol
E. coli	Escherichia coli
EPS	extracellular polymeric substances
FCS	fluorescent correlation spectroscopy

Fmoc	9-fuorenylmethyloxycarbonyl
GlpF	glycerol facilitator
ζ	zeta-potential
GUV	giant unilamellar vesicle
HEMA	2-hydroxyethyl methacrylate
HGF	human-gingival-fibroblasts
HPLC	high-performance liquid chromatography
HRP	horseradish peroxidase
IOP	iron oxide-encapsulating polymersome
JIS	japan industrial standard
LS	light scattering
M. bovis-BCG	M. bovis-attenuated Bacillus Calmette-Guérin
M. marinum	Mycobacterium marinum
M. tuberculosis	Mycobacterium tuberculosis
MBC	minimum bactericidal concentration
MBEC	minimal biofilm eradication concentration
MIC	minimal inhibition concentration
$\mathbf{M}_n$	number average molecular weight
mPEG-PDLLA	methoxypoly(ethelyne glycol)-poly(D)-(L)-lactic acid
MSSA	methicillin-Sensitive S. Aureus
$\mathbf{M}_w$	weight average molecular weight
MWCO	molecular weight cut-off
NP	nanoparticle
OD	optical density
OG	octyl glucopyranoside
OmpF	outer membrane pore F
P	packing parameter
P. gingivalis	Porphyromonas gingivalis
P. mirabilis	Proteus mirabilis
PA	penicillin acylase
PCL	poly(ϵ-caprolactone)
PCL-b-P(Lys-stat-Phe)	poly(ϵ-caprolactone)-block-poly(lysine-stat-phenylalanine)
PDI	polydispersity indice
PDMAEMA	poly(2-dimethylaminoethyl methacralte)
PDMS	polydimethylsiloxane
PDPA	poly[2-(diisopropylamino) ethyl methacrylate]
PEG	polyethylene glycol
PGME	phenylglycine methyl ester
PLLA	poly(L-lactic acid)
PMEO 2 MA-b-PTA	poly[2-(2-methoxyethoxy)ethyl methacrylate]-Poly[2-(tert-butylamino
PMOXA	poly(2-methyl-2-oxazoline)
PMOXA-b-PDMS-b-PMOXA	poly(2-methyloxazoline)-block-poly(dimethylsiloxane-block-poly(2-me
PMPC	poly[2-(methacryloyloxy) ethyl phosphorylcholine]
PMPI	p-maleimidophenyl isocyanate
PP	polypropylene
PSD	particle size distribution
PVA	polyvinyl alcohol
QCM-D	quarz crystal microbalance with dissipation monitoring

RAFT	reversible addition-fragmentation chain transfer
RDH	ribitol dehydrogenase
ROS	reactive oxygen species
R_g	radius of gyration
R-genes	Resistance genes
R_H	hydrodynamic radius
ρ	shape factor
RNA	ribonucleic acid
ROP	ring opening polymerization
rt	room temperature
S. aureus	Staphylococcus aureus
S. epidermidis	Staphylococcus epidermidis
SA-CS-Ti	sulfuric acid treated titanium surface with immobilized chitosan
SA-Ti	sulfuric acid treated titanium surface
SEC	size exclusion chromatography
SEM	scanning electron microscopy
SLS	static light scattering
SPAAC	strain promoted azide alkyne click
SPION	superparamagnetic iron oxide nanoparticle
SRB	sulforhodamine B
TCEP	tris(2-carboxyethyl)phosphine
TEM	transmission electron microscopy
TFA	Trifluoroacetic acid
Ti-6Al-4V	Titanium Alloy (6% Al and 4% V)
TIS	Triisopropylsilane
TMB	3,3',5,5'-tetramethylbenzidin
TpyCP	tetraalkylpyridinium porphyrin
TSB	tryptic soy broth
μCP	micro-contact printing
Un-Ti	untreated titanium surface

References

[1] Rigo, S.; Cai, C.; Gunkel-Grabole, G.; Maurizi, L.; Zhang, X.; Xu, J.; Palivan, C. G. *Advanced Science* **2018**, *5*, 1700892.

[2] Belluati, A.; Craciun, I.; Meyer, C. E.; Rigo, S.; Palivan, C. G. *Current Opinion in Biotechnology* **2019**, *60*, 53–62.

[3] Rigo, S.; Kyropoulou, M.; Schoenenberger, C.-A.; Palivan, C. G. In *Racing for the Surface: Pathogenesis of Implant Infection and Advanced Antimicrobial Strategies*; Li, B., Moriarty, T. F., Webster, T., Xing, M., Eds.; Springer International Publishing: Cham, 2020; pp 385–408.

[4] Chen, Y. E.; Fischbach, M. A.; Belkaid, Y. *Nature* **2018**, *553*, 427.

[5] Sohn, E. *Nature Outlook* **2018**, *563*, 91–93.

[6] Sears, C. L. *Anaerobe* **2005**, *11*, 247 – 251.

[7] Pluznick, J. L. *Frontiers in Endocrinology* **2014**, *5*, 91.

[8] Krajmalnik-Brown, R.; Ilhan, Z. E.; Kang, D. W.; DiBaise, J. K. *Nutrition in Clinical Practice* **2012**, *27*, 201–214.

[9] Hill, J. M.; Clement, C.; Pogue, A. I.; Bhattacharjee, S.; Zhao, Y. H.; Lukiw, W. J. *Frontiers in Aging Neuroscience* **2014**, *6*, Article 127.

[10] Zheng, P. et al. *Molecular Psychiatry* **2016**, *21*, 786–796.

[11] Aminov, R. I. *Frontiers in Microbiology* **2010**, *1*, Article 134.

[12] Antibiotic resistance. `https://www.who.int/news-room/fact-sheets/detail/antibiotic-resistance`.

[13] Arciola, C. R.; Campoccia, D.; Montanaro, L. *Nature Reviews Microbiology* **2018**, *16*, 397–409.

[14] Campoccia, D.; Montanaro, L.; Arciola, C. R. *Biomaterials* **2013**, *34*, 8018 – 8029.

[15] Moriarty, T. F.; Schlegel, U.; Perren, S.; Richards, R. G. *Journal of Materials Science: Materials in Medicine* **2010**, *21*, 1031–1035.

[16] Blanchette, A. K.; Wenke, C. J. *Journal of Bone & Joint Infection* **2018**, *3*, 50–67.

[17] Fawzy, S.; Abdel-Latif, W.; Gamal, R. *Egyptian Journal of Medical Microbiology* **2016**, *25*, 91–100.

[18] Chen, M.; Yu, Q. S.; Sun, H. M. *International Journal of Molecular Sciences* **2013**, *14*, 18488–18501.

[19] Chimutengwende-Gordon, M.; Pendegrass, C.; Bayston, R.; Blunn, G. *Biointerphases* **2014**, *9*, 031010.

[20] De Giglio, E.; Cafagna, D.; Cometa, S.; Allegretta, A.; Pedico, A.; Giannossa, L. C.; Sabbatini, L.; Mattioli-Belmonte, M.; Iatta, R. *Analytical and Bioanalytical Chemistry* **2013**, *405*, 805–816.

[21] Qi, L. H.; Li, H.; Zhang, C. F.; Liang, B. B.; Li, J.; Wang, L. G.; Du, X. Y.; Liu, X. L.; Qiu, S. F.; Song, H. B. *Frontiers in Microbiology* **2016**, *7*, Article 483.

[22] Mukherjee, S.; Bossier, B. L. *Nature Reviews Microbiology* **2019**, *17*, 371–382.

[23] Flemming, H. C.; Wingender, J.; Szewzyk, U.; Steinberg, P.; Rice, S. A.; Kjelleberg, S. *Nature Reviews Microbiology* **2016**, *14*, 563–575.

[24] Flemming, H. C.; Wingender, J. *Nature Reviews Microbiology* **2010**, *8*, 623–633.

[25] Kostakioti, M.; Hadjifrangiskou, M.; Hultgren, S. J. *Cold Spring Harbor Perspectives in Medicine* **2013**, *3*, a010306.

[26] Perez-Diaz, M.; Alvarado-Gomez, E.; Magana-Aquino, M.; Sanchez-Sanchez, R.; Velasquillo, C.; Gonzalez, C.; Ganem-Rondero, A.; Martinez-Castanon, G.; Zavala-Alonso, N.; Martinez-Gutierrez, F. *Materials Science & Engineering C-Materials for Biological Applications* **2016**, *60*, 317–323.

[27] Romling, U.; Balsalobre, C. *Journal of Internal Medicine* **2012**, *272*, 541–561.

[28] Bos, R.; van der Mei, H. C.; Busscher, H. J. *Fems Microbiology Reviews* **1999**, *23*, 179–230.

[29] Lopez, D.; Vlamakis, H.; Kolter, R. *Cold Spring Harbor Perspectives in Biology* **2010**, *2*, 2:a000398.

[30] Saxena, P.; Joshi, Y.; Rawat, K.; Bisht, R. *Indian Journal of Microbiology* **2019**, *59*, 3–12.

[31] Macia, M. D.; Rojo-Molinero, E.; Oliver, A. *Clinical Microbiology and Infection* **2014**, *20*, 981–990.

[32] Francesko, A.; Fernandes, M. M.; Ivanova, K.; Amorim, S.; Reis, R. L.; Pashkuleva, I.; Mendoza, E.; Pfeifer, A.; Heinze, T.; Tzanov, T. *Acta Biomaterialia* **2016**, *33*, 203–212.

[33] Ahmed, N. A.; Petersen, F. C.; Scheie, A. A. *Antimicrobial Agents and Chemotherapy* **2009**, *53*, 4258–4263.

[34] Bedran, T. B. L.; Grignon, L.; Spolidorio, D. P.; Grenier, D. *Plos One* **2014**, *9*, e89059.

[35] Ploux, L.; Ponche, A.; Anselme, K. *Journal of Adhesion Science and Technology* **2010**, *24*, 2165–2201.

[36] Ivanova, E. P.; Hasan, J.; Webb, H. K.; Truong, V. K.; Watson, G. S.; Watson, J. A.; Baulin, V. A.; Pogodin, S.; Wang, J. Y.; Tobin, M. J.; Lobbe, C.; Crawford, R. J. *Small* **2012**, *8*, 2489–2494.

[37] Ivanova, E. P.; Hasan, J.; Webb, H. K.; Gervinskas, G.; Juodkazis, S.; Truong, V. K.; Wu, A. H. F.; Lamb, R. N.; Baulin, V. A.; Watson, G. S.; Watson, J. A.; Mainwaring, D. E.; Crawford, R. J. *Nature Communications* **2013**, *4*, ncomms3838.

[38] Armentano, I.; Arciola, C. R.; Fortunati, E.; Ferrari, D.; Mattioli, S.; Amoroso, C. F.; Rizzo, J.; Kenny, J. M.; Imbriani, M.; Visai, L. *Scientific World Journal* **2014**, Article ID 410423.

[39] Scardino, A. J.; Harvey, E.; De Nys, R. *Biofouling* **2006**, *22*, 55–60.

[40] Meng, J. X.; Zhang, P. C.; Wang, S. T. *Chemistry-an Asian Journal* **2014**, *9*, 2004–2016.

[41] Anselme, K.; Davidson, P.; Popa, A. M.; Giazzon, M.; Liley, M.; Ploux, L. *Acta Biomaterialia* **2010**, *6*, 3824–3846.

[42] Kugler, R.; Bouloussa, O.; Rondelez, F. *Microbiology-Sgm* **2005**, *151*, 1341–1348.

[43] Zimmerli, W.; Sendi, P. *Seminars in Immunopathology* **2011**, *33*, 295–306.

[44] Siedenbiedel, F.; Tiller, J. C. *Polymers* **2012**, *4*, 46–71.

[45] Zhao, B.; van der Mei, H. C.; Subbiahdoss, G.; de Vries, J.; Rustema-Abbing, M.; Kuijer, R.; Busscher, H. J.; Ren, Y. J. *Dental Materials* **2014**, *30*, 716–727.

[46] Papaspyridakos, P.; Mokti, M.; Chen, C. J.; Benic, G. I.; Gallucci, G. O.; Chronopoulos, V. *Clinical Implant Dentistry and Related Research* **2014**, *16*, 705–717.

[47] Pjetursson, B. E.; Thoma, D.; Jung, R.; Zwahlen, M.; Zembic, A. *Clinical Oral Implants Research* **2012**, *23*, 22–38.

[48] Foss, B. L.; Ghimire, N.; Tang, R. G.; Sun, Y. Y.; Deng, Y. *Colloids and Surfaces B-Biointerfaces* **2015**, *134*, 370–376.

[49] Busscher, H. J.; van der Mei, H. C.; Subbiahdoss, G.; Jutte, P. C.; van den Dungen, J. J. A. M.; Zaat, S. A. J.; Schultz, M. J.; Grainger, D. W. *Science Translational Medicine* **2012**, *4*, 153rv10.

[50] Subbiahdoss, G.; Kuijer, R.; Grijpma, d. W.; van der Mei, H. C.; Busscher, H. J. *Acta Biomaterialia* **2009**, *5*, 1399–1404.

[51] We need new antibiotics for Gram-negative, not Gram-positive bacteria. https://reflectionsipc.com/2015/01/12/we-need-new-antibiotics-for-gram-negative-not-gram-positive-bacteria/.

[52] Gram Staining. https://ib.bioninja.com.au/options/untitled/b1-microbiology-organisms/gram-staining.html.

[53] Shakibaie, M.; Forootanfar, H.; Golkari, Y.; Mohammadi-Khorsand, T.; Shakibaie, M. R. *Journal of Trace Elements in Medicine and Biology* **2015**, *29*, 235–241.

[54] Ma, H. Y.; Darmawan, E. T.; Zhang, M.; Zhang, L.; Bryers, J. D. *Journal of Controlled Release* **2013**, *172*, 1035–1044.

[55] Ferraris, S.; Spriano, S. *Materials Science & Engineering C-Materials for Biological Applications* **2016**, *61*, 965–978.

[56] Knetsch, M. L. W.; Koole, L. H. *Polymers* **2011**, *3*, 340–366.

[57] Klasen, H. J. *Burns* **2000**, *26*, 117–130.

[58] Silver, S. *Fems Microbiology Reviews* **2003**, *27*, 341–353.

[59] Park, H. J.; Park, S.; Roh, J.; Kim, S.; Choi, K.; Yi, J.; Kim, Y.; Yoon, J. *Journal of Industrial and Engineering Chemistry* **2013**, *19*, 614–619.

[60] Phoenix, D. A.; Dennison, S. R.; Harris, F. *Antimicrobial Peptides*; 2013; pp 1–37.

[61] Ali, S. M.; Siddiqui, R.; Khan, N. A. *Journal of Pharmacy and Pharmacology* **2018**, *70*, 1287–1300.

[62] Riool, M.; de Breij, A.; de Boer, L.; Kwakman, P. H. S.; Cordfunke, R. A.; Cohen, O.; Malanovic, N.; Emanuel, N.; Lohner, K.; Drijfhout, J. W.; Nibbering, P. H.; Zaat, S. A. J. *Advanced Functional Materials 27*, 1606623.

[63] Holmberg, K. V.; Abdolhosseini, M.; Li, Y. P.; Chen, X.; Gorr, S. U.; Aparicio, C. *Acta Biomaterialia* **2013**, *9*, 8224–8231.

[64] Cado, G. et al. *Advanced Functional Materials* **2013**, *23*, 4801–4809.

[65] Kazemzadeh-Narbat, M.; Lai, B. F. L.; Ding, C. F.; Kizhakkedathu, J. N.; Hancock, R. E. W.; Wang, R. Z. *Biomaterials* **2013**, *34*, 5969–5977.

[66] Fry, D. E. *Surgical Infections* **2018**, *19*, 804–811.

[67] Malmsten, M. *Upsala Journal of Medical Sciences* **2014**, *119*, 199–204.

[68] Yazici, H.; O'Neill, M. B.; Kacar, T.; Wilson, B. R.; Oren, E. E.; Sarikaya, M.; Tamerier, C. *Acs Applied Materials & Interfaces* **2016**, *8*, 5070–5081.

[69] Levy, S. B. *Ciba Foundation Symposium 207 Antibiotic Resistance: Origins, Evolution, Selection and Spread*; John Wiley & Sons, Ltd, 2007; pp 1–14.

[70] Davies, J. E. *Ciba Foundation Symposium 207 Antibiotic Resistance: Origins, Evolution, Selection and Spread*; John Wiley & Sons, Ltd, 2007; pp 15–35.

[71] Davies, J.; Davies, D. *Microbiology and Molecular Biology Reviews* **2010**, *74*, 417–433.

[72] Raposo, G.; Stoorvogel, W. *JCB* **2013**, *200*, 373–383.

[73] Hessvik, N. P.; Llorente, A. *Cellular and Molecular Life Sciences* **2018**, *75*, 193–208.

[74] Cullen, P. J.; Steinberg, F. *Nature Reviews Molecular Cell Biology* **2018**, *19*, 679–696.

[75] Cabukusta, B.; Neefjes, J. *Traffic* **2018**, *19*, 761–769.

[76] Zhang, X.; Tanner, P.; Graff, A.; Palivan, C. G.; Meier, W. *J. Polym. Sci., Part A: Polym. Chem.* **2012**, *50*, 2293–2318.

[77] Traversier, M.; Gaslondes, T.; Milesi, S.; Michel, S.; Delannay, E. *Phytochemistry Reviews* **2018**, *17*, 1179–1210.

[78] Tran, S.; DeGiovanni, P. J.; Piel, B.; Rai, P. *Clinical and Translational Medicine* **2017**, *6*, 6:44.

[79] Abu Lila, A. S.; Ishida, T. *Biological & Pharmaceutical Bulletin* **2017**, *40*, 1–10.

[80] Gunkel-Grabole, G.; Sigg, S.; Lomora, M.; Lorcher, S.; Palivan, C. G.; Meier, W. P. *Biomater. Sci.* **2015**, *3*, 25–40.

[81] Blanazs, A.; Armes, S. P.; Ryan, A. J. *Macromolecular Rapid Communications* **2009**, *30*, 267–277.

[82] Lorcher, S.; Meier, W. *European Polymer Journal* **2017**, *88*, 575–585.

[83] Mai, Y.; Eisenberg, A. *Chem. Soc. Rev.* **2012**, *41*, 5969–5985.

[84] Konishcheva, E. V.; Daubian, D.; Rigo, S.; Meier, W. P. *Chemical Communications* **2019**, *55*, 1148–1151.

[85] Konishcheva, E. V.; Zhumaev, U. E.; Kratt, M.; Oehri, V.; Meier, W. *Macromolecules* **2017**, *50*, 7155–7168.

[86] Konishcheva, E. V.; Zhumaev, U. E.; Meier, W. P. *Macromolecules* **2017**, *50*, 1512–1520.

[87] Itel, F.; Chami, M.; Najer, A.; Lörcher, S.; Wu, D.; Dinu, I. A.; Meier, W. *Macromolecules* **2014**, *47*, 7588–7596.

[88] Itel, F.; Najer, A.; Palivan, C. G.; Meier, W. *Nano Letters* **2015**, *15*, 3871–3878.

[89] Discher, B. M.; Won, Y. Y.; Ege, D. S.; Lee, J. C. M.; Bates, F. S.; Discher, D. E.; Hammer, D. A. *Science* **1999**, *284*, 1143–1146.

[90] Malinova, V.; Nallani, M.; Meier, W. P.; Sinner, E. K. *Febs Letters* **2012**, *586*, 2146–2156.

[91] Discher, D. E.; Ahmed, F. *Annu. Rev. Biomed. Eng.* **2006**, *8*, 323–341.

[92] Discher, D. E.; Eisenberg, A. *Science* **2002**, *297*, 967–973.

[93] Najer, A.; Wu, D. L.; Nussbaumer, M. G.; Schwertz, G.; Schwab, A.; Witschel, M. C.; Schafer, A.; Diederich, F.; Rottmann, M.; Palivan, C. G.; Beck, H. P.; Meier, W. *Nanoscale* **2016**, *8*, 14858–14869.

[94] Penczek, S.; Pretula, J.; Lewinski, P. *Polymers* **2017**, *98*, 646.

[95] Ratcliffe, L. P. D.; Bentley, K. J.; Wehr, R.; Warren, N. J.; Saunders, B. R.; Armes, S. P. *Polym. Chem.* **2017**, *8*, 5962–5971.

[96] Moad, G. *Polymer Chemistry* **2017**, *8*, 177–219.

[97] Palmiero, U. C.; Sponchioni, M.; Manfredini, N.; Maraldi, M.; Moscatelli, D. *Polymer Chemistry* **2018**, *9*, 4084–4099.

[98] Dinu, I. A.; Duskey, J. T.; Car, A.; Palivan, C. G.; Meier, W. *Polym. Chem.* **2016**, *7*, 3451–3464.

[99] Matyjaszewski, K.; Xia, J. *Chem. Rev.* **2001**, *101*, 2921–2990.

[100] Fantin, M.; Lorandi, F.; Gennaro, A.; Isse, A. A.; Matyjaszewski, K. *Synthesis* **2017**, *49*, 3311–3322.

[101] Gaitzsch, J.; Welsch, P. C.; Folini, J.; Schoenenberger, C. A.; Anderson, J. C.; Meier, W. P. *European Polymer Journal* **2018**, *101*, 113–119.

[102] Chojnowski, J.; Cypryk, M.; Fortuniak, W.; Ścibiorek, M.; Rózga-Wijas, K. *Macromolecules* **2003**, *36*, 3890–3897.

[103] Ninago, M. D.; Satti, A. J.; Ressia, J. A.; Ciolino, A. E.; Villar, M. A.; Vallés, E. M. *Journal of Polymer Science Part A: Polymer Chemistry* **2009**, *47*, 4774–4783.

[104] Zhang, X. Y.; Zhang, P. Y. *Current Nanoscience* **2017**, *13*, 124–129.

[105] Konishcheva, E.; Daubian, D.; Gaitzsch, J.; Meier, W. *Helvetica Chimica Acta* **2018**, *101*, e1700287.

[106] Bai, L.; Tan, L.; Chen, L.; Liu, S.; Wang, Y. *J. Mater. Chem. B* **2014**, *2*, 7785–7794.

[107] Konradi, R.; Pidhatika, B.; Mühlebach, A.; Textor, M. *Langmuir* **2008**, *24*, 613–616.

[108] Aoshima, S.; Kanaoka, S. *Chem. Rev.* **2009**, *109*, 5245–5287.

[109] Najer, A.; Wu, D.; Vasquez, D.; Palivan, C. G.; Meier, W. *Nanomedicine* **2013**, *8*, 425–447.

[110] Jahn, A.; Vreeland, W. N.; Gaitan, M.; Locascio, L. E. *Journal of the American Chemical Society* **2004**, *126*, 2674–2675.

[111] Supramaniam, P.; Ces, O.; Salehi-Reyhani, A. *Micromachines* **2019**, *10*, 299.

[112] Lanzilotto, A.; Kyropoulou, M.; Constable, E. C.; Housecroft, C. E.; Meier, W. P.; Palivan, C. G. *Journal of Biological Inorganic Chemistry* **2018**, *23*, 109–122.

[113] Kita-Tokarczyk, K.; Grumelard, J.; Haefele, T.; Meier, W. *Polymer* **2005**, *46*, 3540 – 3563.

[114] LoPresti, C.; Lomas, H.; Massignani, M.; Smart, T.; Battaglia, G. *Journal of Materials Chemistry* **2009**, *19*, 3576–3590.

[115] Smart, T.; Lomas, H.; Massignani, M.; Flores-Merino, M. V.; Perez, L. R.; Battaglia, G. *Nano Today* **2008**, *3*, 38–46.

[116] Palivan, C. G.; Goers, R.; Najer, A.; Zhang, X. Y.; Car, A.; Meier, W. *Chemical Society Reviews* **2016**, *45*, 377–411.

[117] Nardin, C.; Widmer, J.; Winterhalter, M.; Meier, W. *Eur. Phys. J. E* **2001**, *4*, 403–410.

[118] Broz, P.; Benito, A. M.; Saw, C.; Burger, P.; Heider, H.; Pfisterer, M.; Marsch, S.; Meier, W.; Hunziker, P. *J. Control. Release* **2005**, *102*, 475–488.

[119] Onaca, O.; Enea, R.; Hughes, D. W.; Meier, W. *Macromolecular Bioscience* **2009**, *9*, 129–139.

[120] Zhang, C.; Zhu, Y. Q.; Zhou, C. C.; Yuan, W. Z.; Du, J. Z. *Polymer Chemistry* **2013**, *4*, 255–259.

[121] Wang, M. Z.; Zhou, C. C.; Chen, J.; Xiao, Y. F.; Du, J. Z. *Bioconjugate Chemistry* **2015**, *26*, 725–734.

[122] Belluati, A.; Craciun, I.; Liu, J.; Palivan, C. G. *Biomacromolecules* **2018**, *19*, 4023–4033.

[123] Antonietti, M.; Förster, S. *Adv. Mater.* **2003**, *15*, 1323–1333.

[124] Tanner, P.; Onaca, O.; Balasubramanian, V.; Meier, W.; Palivan, C. G. *Chem. Eur. J.* **2011**, *17*, 4552–4560.

[125] Kumar, M.; Grzelakowski, M.; Zilles, J.; Clark, M.; Meier, W. *Proc. Natl. Acad. Sci. USA* **2007**, *104*, 20719–20724.

[126] Thamboo, S.; Najer, A.; Belluati, A.; von Planta, C.; Wu, D.; Craciun, I.; Meier, W.; Palivan, C. G. *Advanced Functional Materials* **2019**, *29*, 1904267.

[127] Axthelm, F.; Casse, O.; Koppenol, W. H.; Nauser, T.; Meier, W.; Palivan, C. G. *J. Phys. Chem. B* **2008**, *112*, 8211–8217.

[128] Kuiper, S. M.; Nallani, M.; Vriezema, D. M.; Cornelissen, J. J. L. M.; van Hest, J. C. M.; Nolte, R. J. M.; Rowan, A. E. *Org. Biomol. Chem.* **2008**, *6*, 4315–4318.

[129] Spulber, M.; Najer, A.; Winkelbach, K.; Glaied, O.; Waser, M.; Pieles, U.; Meier, W.; Bruns, N. *J. Am. Chem. Soc.* **2013**, *135*, 9204–9212.

[130] Cheng, Z.; Tsourkas, A. *Langmuir* **2008**, *24*, 8169–8173.

[131] Palivan, C. G.; Vebert, C.; Asthelm, F.; Meier, W. *Nanotechnology in Biology and Medicine*; CRC Press LLC, 2007; Chapter 32, pp 32/1–32/26.

[132] Garni, M.; Thamboo, S.; Schoenenberger, C. A.; Palivan, C. G. *Biochimica Et Biophysica Acta-Biomembranes* **2017**, *1859*, 619–638.

[133] Schmitt, C.; Lippert, A. H.; Bonakdar, N.; Sandoghdar, V.; Voll, L. M. *Frontiers in Bioengineering and Biotechnology* **2016**, *4*, Article 19.

[134] Lomora, M.; Itel, F.; Dinu, I. A.; Palivan, C. G. *Phys. Chem. Chem. Phys.* **2015**, *17*, 15538–15546.

[135] Lomora, M.; Garni, M.; Itel, F.; Tanner, P.; Spulber, M.; Palivan, C. G. *Biomaterials* **2015**, *53*, 406 – 414.

[136] Tangorra, R. R.; Operamolla, A.; Milano, F.; Omar, O. H.; Henrard, J.; Comparelli, R.; Italiano, F.; Agostiano, A.; De Leo, V.; Marotta, R.; Falqui, A.; Farinola, G. M.; Trotta, M. **2015**, *14*, 1844–1852.

[137] Goers, R.; Thoma, J.; Ritzmann, N.; Di Silvestro, A.; Alter, C.; Gunkel-Grabole, G.; Fotiadis, D.; Muller, D. J.; Meier, W. *Communications Chemistry* **2018**, *1*, s42004–018–0037–8.

[138] Koebnik, R.; Locher, K. P.; Van Gelder, P. *Mol. Microbio.* **2000**, *37*, 239–253.

[139] Klermund, L.; Poschenrieder, S. T.; Castiglione, K. *Acs Catalysis* **2017**, *7*, 3900–3904.

[140] Lomora, M.; Dinu, I. A.; Itel, F.; Rigo, S.; Spulber, M.; Palivan, C. G. *Macromolecular Rapid Communications* **2015**, *36*, 1929–1934.

[141] Edlinger, C.; Einfalt, T.; Spulber, M.; Car, A.; Meier, W.; Palivan, C. G. *Nano Letters* **2017**, *17*, 5790–5798.

[142] Grafe, D.; Gaitzsch, J.; Appelhans, D.; Voit, B. *Nanoscale* **2014**, *6*, 10752–10761.

[143] Kern, H. B.; Srinivasan, S.; Convertine, A. J.; Hockenbery, D.; Press, O. W.; Stayton, P. S. *Molecular Pharmaceutics* **2017**, *14*, 1450–1459.

[144] Wayakanon, K.; Thornhill, M. H.; Douglas, C. W. I.; Lewis, A. L.; Warren, N. J.; Pinnock, A.; Armes, S. P.; Battaglia, G.; Murdoch, C. *Faseb Journal* **2013**, *27*, 4455–4465.

[145] Rizzello, L. et al. *bioRxiv* **2017**, 119297.

[146] Lane, D. D.; Su, F. Y.; Chiu, D. Y.; Srinivasan, S.; Wilson, J. T.; Ratner, D. M.; Stayton, P. S.; Convertine, A. J. *Polymer Chemistry* **2015**, *6*, 1255–1266.

[147] Hong, Y. X.; Xi, Y. J.; Zhang, J. X.; Wang, D. D.; Zhang, H. L.; Yan, N.; He, S. S.; Du, J. Z. *Journal of Materials Chemistry B* **2018**, *6*, 6311–6321.

[148] Kurtjak, M.; Aničić, N.; Vukomanovicć, M. In *Antibacterial Agents*; Kumavath, R. N., Ed.; IntechOpen: Rijeka, 2017; Chapter 3.

[149] Lu, H.; Fan, L.; Liu, Q. M.; Wei, J. R.; Ren, T. B.; Du, J. Z. *Polymer Chemistry* **2012**, *3*, 2217–2227.

[150] Geilich, B. M.; van de Ven, A. L.; Singleton, G. L.; Sepulveda, L. J.; Sridhar, S.; Webster, T. J. *Nanoscale* **2015**, *7*, 3511–3519.

[151] Geilich, B. M.; Gelfat, I.; Sridhar, S.; van de Ven, A. L.; Webster, T. J. *Biomaterials* **2017**, *119*, 78–85.

[152] Langowska, K.; Palivan, C. G.; Meier, W. *Chemical Communications* **2013**, *49*, 128–130.

[153] Wick, W. E. *Applied Microbiology* **1967**, *15*, 765–769.

[154] Spratt, B. G. *Proceedings of the National Academy of Sciences of the United States of America* **1967**, *72*, 2999–3003.

[155] Biswaro, L. S.; Sousa, M. G. D.; Rezende, T. M. B.; Dias, S. C.; Franco, O. L. *Frontiers in Microbiology* **2018**, *9*, Article 855.

[156] Wang, C. H.; Feng, S. L.; Qie, J. K.; Wei, X. L.; Yan, H. S.; Liu, K. L. *International Journal of Pharmaceutics* **2019**, *554*, 284–291.

[157] Braun, K.; Pochert, A.; Linden, M.; Davoudi, M.; Schmidtchen, A.; Nordstrom, R.; Malmsten, M. *Journal of Colloid and Interface Science* **2016**, *475*, 161–170.

[158] Gontsarik, M.; Yaghmur, A.; Ren, Q.; Maniura-Weber, K.; Salentinig, S. *Acs Applied Materials & Interfaces* **2019**, *11*, 2821–2829.

[159] Nordstrom, R.; Nystrom, L.; Andren, O. C. J.; Malkoch, M.; Umerska, A.; Davoudi, M.; Schmidtchen, A.; Malmsten, M. *Journal of Colloid and Interface Science* **2018**, *513*, 141–150.

[160] Nordstrom, R.; Nystrom, L.; Ilyas, H.; Atreya, H. S.; Borro, B. C.; Bhunia, A.; Malmsten, M. *Colloids and Surfaces a-Physicochemical and Engineering Aspects* **2019**, *565*, 8–15.

[161] Kumar, P.; Pletzer, D.; Haney, E. F.; Rahanjam, N.; Cheng, J. T. J.; Yue, M.; Aljehani, W.; Hancock, R. E. W.; Kizhakkedathu, J. N.; Straus, S. K. *Acs Infectious Diseases* **2019**, *5*, 443–453.

[162] Jafari, M.; Doustdar, F.; Mehrnejad, F. *Journal of Chemical Information and Modeling* **2019**, *59*, 550–563.

[163] Zhao, N. et al. *Advanced Materials* **2014**, *26*, 6994–7017.

[164] Baum, C.; Meyer, W.; Stelzer, R.; Fleischer, L. G.; Siebers, D. *Marine Biology* **2002**, *140*, 653–657.

[165] Wen, L.; Weaver, J. C.; Lauder, G. V. *Journal of Experimental Biology* **2014**, *217*, 1656–1666.

[166] Guenther, J.; De Nys, R. *Biofouling* **2007**, *23*, 419–429.

[167] Scardino, A.; De Nys, R.; Ison, O.; O'Connor, W.; Steinberg, P. *Biofouling* **2003**, *19*, 221–230.

[168] Cao, X. Y.; Pettitt, M. E.; Wode, F.; Sancet, M. P. A.; Fu, J. H.; Ji, J. A.; Callow, M. E.; Callow, J. A.; Rosenhahn, A.; Grunze, M. *Advanced Functional Materials* **2010**, *20*, 1984–1993.

[169] Magin, C. M.; Long, C. J.; Cooper, S. P.; Ista, L. K.; Lopez, G. P.; Brennan, A. B. *Biofouling* **2010**, *26*, 719–727.

[170] Bhadury, P.; Wright, P. C. *Planta* **2004**, *216*, 561–578.

[171] Glinel, K.; Thebault, P.; Humblot, V.; Pradier, C. M.; Jouenne, T. *Acta Biomaterialia* **2012**, *8*, 1670–1684.

[172] Muller, W. E. G.; Wang, X. H.; Proksch, P.; Perry, C. C.; Osinga, R.; Garderes, J.; Schroder, H. C. *Marine Biotechnology* **2013**, *15*, 375–398.

[173] Long, C. J.; Schumacher, J. F.; Robinson, P. A. C.; Finlay, J. A.; Callow, M. E.; Callow, J. A.; Brennan, A. B. *Biofouling* **2010**, *26*, 411–419.

[174] Carman, M. L.; Estes, T. G.; Feinberg, A. W.; Schumacher, J. F.; Wilkerson, W.; Wilson, L. H.; Callow, M. E.; Callow, J. A.; Brennan, A. B. *Biofouling* **2006**, *22*, 11–21.

[175] Efimenko, K.; Finlay, J.; Callow, M. E.; Callow, J. A.; Genzer, J. *Acs Applied Materials & Interfaces* **2009**, *1*, 1031–1040.

[176] Saeki, D.; Tanimoto, T.; Matsuyama, H. *Colloids and Surfaces A: Physicochemical and Engineering Aspects* **2014**, *443*, 171 – 176.

[177] Gunkel, G.; Weinhart, M.; Becherer, T.; Haag, R.; Huck, W. T. S. *Biomacromolecules* **2011**, *12*, 4169–4172.

[178] Gunkel, G.; Huck, W. T. S. *Journal of the American Chemical Society* **2013**, *135*, 7047–7052.

[179] Chapman, J.; Hellio, C.; Sullivan, T.; Brown, R.; Russell, S.; Kiterringham, E.; Le Nor, L.; Regan, F. *International Biodeterioration & Biodegradation* **2014**, *86*, 6–13.

[180] Fisher, L. E.; Yang, Y.; Yuen, M. F.; Zhang, W. J.; Nobbs, A. H.; Su, B. *Biointerphases* **2016**, *11*, 011014.

[181] Hasan, J.; Raj, S.; Yadav, L.; Chatterjee, K. *Rsc Advances* **2015**, *5*, 44953–44959.

[182] Hasan, J.; Crawford, R. J.; Lvanova, E. P. *Trends in Biotechnology* **2013**, *31*, 31–40.

[183] Gillett, A.; Waugh, D.; Lawrence, J.; Swainson, M.; Dixon, R. *Journal of Laser Applications* **2016**, *28*, 022503.

[184] Freschauf, L. R.; McLane, J.; Sharma, H.; Khine, M. *Plos One* **2012**, *7*, e40987.

[185] Vasudevan, R.; Kennedy, A. J.; Merritt, M.; Crocker, F. H.; Baney, R. H. *Colloids and Surfaces B-Biointerfaces* **2014**, *117*, 225–232.

[186] Ng, V. W. L.; Chan, J. M. W.; Sardon, H.; Ono, R. J.; Garcia, J. M.; Yang, Y. Y.; Hedrick, J. L. *Advanced Drug Delivery Reviews* **2014**, *78*, 46–62.

[187] Wang, B. L.; Liu, H. H.; Zhang, B. J.; Han, Y. M.; Shen, C. H.; Lin, Q. K.; Chen, H. *Colloids and Surfaces B-Biointerfaces* **2016**, *141*, 483–490.

[188] Zhu, C.; Zhang, W. W.; Fang, S. Y.; Kong, R.; Zou, G.; Bao, N. R.; Zhao, J. N.; Shang, X. F. *Journal of Materials Science* **2018**, *53*, 5891–5908.

[189] Cao, P.; Yuan, C. Q.; Xiao, J. F.; He, X. Y.; Bai, X. Q. *Surface and Interface Analysis* **2018**, *50*, 516–521.

[190] Rai, A.; Pinto, S.; Evangelista, M. B.; Gil, H.; Kallip, S.; Ferreira, M. G. S.; Ferreira, L. *Acta Biomaterialia* **2016**, *33*, 64–77.

[191] Zaccaria, S.; van Gaal, R. C.; Riool, M.; Zaat, S. A. J.; Dankers, P. Y. W. *Journal of Polymer Science Part a-Polymer Chemistry* **2018**, *56*, 1926–1934.

[192] Zhan, J. Z.; Wang, L.; Zhu, Y. C.; Gao, H. C.; Chen, Y. H.; Chen, J. J.; Jia, Y. G.; He, J. C.; Fang, Z.; Zhu, Y.; Mao, C. B.; Ren, L.; Wang, Y. J. *Acs Applied Materials & Interfaces* **2018**, *10*, 35830–35837.

[193] Nystrom, L.; Stromstedt, A. A.; Schmidtchen, A.; Malmsten, M. *Biomacromolecules* **2018**, *19*, 3456–3466.

[194] Nystrom, L.; Al-Rammahi, N.; Haffner, S. M.; Stromstedt, A. A.; Browning, K. L.; Malmsten, M. *Biomacromolecules* **2018**, *19*, 4691–4702.

[195] Onaizi, S. A.; Leong, S. S. J. *Biotechnology Advances* **2011**, *29*, 67–74.

[196] Cui, J. W.; Ju, Y.; Liang, K.; Ejima, H.; Lorcher, S.; Gause, K. T.; Richardson, J. J.; Caruso, F. *Soft Matter* **2014**, *10*, 2656–2663.

[197] de Breij, A.; Riool, M.; Kwakman, P. H. S.; de Boer, L.; Cordfunke, R. A.; Drijfhout, J. W.; Cohen, O.; Emanuel, N.; Zaat, S. A. J.; Nibbering, P. H.; Moriarty, T. F. *Journal of Controlled Release* **2016**, *222*, 1–8.

[198] Xu, L. L.; He, C.; Hui, L. W.; Xie, Y. T.; Li, J. M.; He, W. D.; Yang, L. H. *Acs Applied Materials & Interfaces* **2015**, *7*, 27602–27607.

[199] Costa, F.; Carvalho, I. F.; Montelaro, R. C.; Gomes, P.; Martins, M. C. L. *Acta Biomaterialia* **2011**, *7*, 1431–1440.

[200] Gallucci, M. N.; Fraire, J. C.; Maillard, A. P. V. F.; Paez, P. L.; Martinez, I. M. A.; Miner, E. V. P.; Coronado, E. A.; Dalmasso, P. R. *Materials Letters* **2017**, *197*, 98–101.

[201] Hu, R.; Li, G. Z.; Jiang, Y. J.; Zhang, Y.; Zou, J. J.; Wang, L.; Zhang, X. W. *Langmuir* **2013**, *29*, 3773–3779.

[202] Franci, G.; Falanga, A.; Galdiero, S.; Palomba, L.; Rai, M.; Morelli, G.; Galdiero, M. *Molecules* **2015**, *20*, 8856–8874.

[203] Qin, H.; Cao, H. L.; Zhao, Y. C.; Zhu, C.; Cheng, T.; Wang, Q. J.; Peng, X. C.; Cheng, M. Q.; Wang, J. X.; Jin, G. D.; Jiang, Y.; Zhang, X. L.; Liu, X. Y.; Chu, P. K. *Biomaterials* **2014**, *35*, 9114–9125.

[204] Brunetto, P. S.; Slenters, T. V.; Fromm, K. M. *Materials* **2011**, *4*, 355–367.

[205] Huang, H.; Lai, W. J.; Cui, M. H.; Liang, L.; Lin, Y. C.; Fang, Q. J.; Liu, Y.; Xie, L. M. *Scientific Reports* **2016**, *6*, srep25518.

[206] Langowska, K.; Kowal, J.; Palivan, C. G.; Meier, W. *J. Mater. Chem. B* **2014**, *2*, 4684–4693.

[207] Grumezescu, V.; Socol, G.; Grumezescu, A. M.; Holban, A. M.; Ficai, A.; Trusca, R.; Bleotu, C.; Balaure, P. C.; Cristescu, R.; Chifiriuc, M. C. *Applied Surface Science* **2014**, *302*, 262–267.

[208] Grzelakowski, M.; Onaca, O.; Rigler, P.; Kumar, M.; Meier, W. *Small* **2009**, *5*, 2545–2548.

[209] Berthaud, A.; Quemeneur, F.; Deforet, M.; Bassereau, P.; Brochard-Wyart, F.; Mangenot, S. *Soft Matter* **2016**, *12*, 1601–1609.

[210] De Vries, W. C.; Tesch, M.; Studer, A.; Ravoo, B. J. *Acs Applied Materials & Interfaces* **2017**, *9*, 41760–41766.

[211] Wu, D.; Rigo, S.; Di Leone, S.; Belluati, A.; Constable, E. C.; Housecroft, C. E.; Palivan, C. G. *Nanoscale* **2020**, *12*, 1551–1562.

[212] Battaglia, G.; LoPresti, C.; Massignani, M.; Warren, N. J.; Madsen, J.; Forster, S.; Vasilev, C.; Hobbs, J. K.; Armes, S. P.; Chirasatitsin, S.; Engler, A. J. *Small* **2011**, *7*, 2010–2015.

[213] Iyisan, B.; Janke, A.; Reichenbach, P.; Eng, L. M.; Appelhans, D.; Voit, B. *Acs Applied Materials & Interfaces* **2016**, *8*, 15788–15801.

[214] Li, F.; Ketelaar, T.; Stuart, M. A. C.; Sudholter, E. J. R.; Leermakers, F. A. M.; Marcelis, A. T. M. *Langmuir* **2008**, *24*, 76–82.

[215] Chen, Q.; de Groot, G. W.; Schonherr, H.; Vancso, G. J. *European Polymer Journal* **2011**, *47*, 130–138.

[216] Choi, J. M.; Yoon, B.; Choi, K.; Seol, M. L.; Kim, J. M.; Choi, Y. K. *Macromolecular Chemistry and Physics* **2012**, *213*, 610–616.

[217] Domes, S.; Filiz, V.; Nitsche, J.; Fromsdorf, A.; Forster, S. *Langmuir* **2010**, *26*, 6927–6931.

[218] Gunkel-Grabole, G.; Palivan, C.; Meier, W. *Macromolecular Materials and Engineering* **2017**, *302*, 1600363.

[219] Rein, C.; Nissen, S.; Grzelakowski, M.; Meldal, M. *Journal of Polymer Science Part a-Polymer Chemistry* **2016**, *54*, 2032–2039.

[220] Lutz, J. F. *Angewandte Chemie-International Edition* **2008**, *47*, 2182–2184.

[221] Agard, N. J.; Prescher, J. A.; Bertozzi, C. R. *Journal of the American Chemical Society* **2005**, *127*, 11196–11196.

[222] Rigo, S.; Gunkel-Grabole, G.; Meier, W.; Palivan, C. G. *Langmuir* **2019**, *35*, 4557–4565.

[223] Rigo, S.; Hürlimann, D.; Marot, L.; Malmsten, M.; Meier, W.; Palivan, C. G. *ACS Applied Bio Materials* **2020**, *3*, 1533–1543.

[224] Kiene, K.; Schenk, S. H.; Porta, F.; Ernst, A.; Witzigmann, D.; Grossen, P.; Huwyler, J. *European Journal of Pharmaceutics and Biopharmaceutics* **2017**, *119*, 322–332.

[225] Xiong, M.-H.; Bao, Y.; Yang, X.-Z.; Zhu, Y.-H.; Wang, J. *Advanced Drug Delivery Reviews* **2014**, *78*, 63 – 76.

[226] Craciun, I.; Denes, A. S.; Gunkel-Grabole, G.; Belluati, A.; Palivan, C. G. *Helvetica Chimica Acta* **2018**, *101*, e1700290.

[227] Zhang, X. Y.; Lomora, M.; Einfalt, T.; Meier, W.; Klein, N.; Schneider, D.; Palivan, C. G. *Biomaterials* **2016**, *89*, 79–88.

[228] Fang, B.; Jiang, Y.; Nusslein, K.; Rotello, V. M.; Santore, M. M. *Colloids and Surfaces B-Biointerfaces* **2015**, *125*, 255–263.

[229] Taheri, S.; Baier, G.; Majewski, P.; Barton, M.; Forch, R.; Landfester, K.; Vasilev, K. *Nanotechnology* **2014**, *25*, 305102.

[230] Ribeiro, K. L.; Frias, I. A. M.; Franco, O. L.; Dias, S. C.; Sousa-Junior, A. A.; Silva, O. N.; Bakuzis, A. F.; Oliveira, M. D. L.; Andrade, C. A. S. *Colloids and Surfaces B-Biointerfaces* **2018**, *169*, 72–81.

[231] Demling, A.; Elter, C.; Heidenblut, T.; Bach, F. W.; Hahn, A.; Schwestka-Polly, R.; Stiesch, M.; Heuer, W. *European Journal of Orthodontics* **2010**, *32*, 414–418.

[232] Hosman, A. H.; Bulstra, S. K.; Sjollema, J.; Van der Mei, H. C.; Busscher, H. J.; Neut, D. *Journal of Orhopaedic Research* **2012**, *30*, 341–347.

[233] Leslie, D. C. et al. *Nature Biotechnology* **2014**, *32*, 1134–1140.

[234] Yoon, H. Y.; Shin, M. L.; Shim, M. K.; Lee, S.; Na, J. H.; Koo, H.; Lee, H.; Kim, J. H.; Lee, K. Y.; Kim, K.; Kwon, I. C. *Molecular Pharmaceutics* **2017**, *14*, 1558–1570.

[235] Eeftens, J. M.; van der Torre, J.; Burnham, D. R.; Dekker, C. *BMC Biophysics 8*, 8:9.

[236] Negwer, I.; Hirsch, M.; Kaloyanova, S.; Brown, T.; Peneva, K.; Butt, H. J.; Koynov, K.; Helm, M. *ChemBioChem communications* **2017**, *18*, 1814–1818.

[237] Takei, Y.; Murata, A.; Yamagishi, K.; Arai, S.; Nakamura, H.; Inoue, T.; Takeoka, S. *Chemical Communications* **2013**, *49*, 7313–7315.

[238] Bak, M.; Jolck, R. I.; Eliasen, R.; Andresen, T. L. *Bioconjugate Chemistry* **2016**, *27*, 1673–1680.

[239] Blenke, E. O.; Klaasse, G.; Merten, H.; Pluckthun, A.; Mastrobattista, E. *Journal of Controlled Release* **2015**, *202*, 14–20.

[240] Wang, C. F.; Sarparanta, M. P.; Makila, E. M.; Hyvonen, M. L. K.; Laakkonen, P. M.; Salonen, J. J.; Hirvonen, J. T.; Airaksinen, A. J.; Santos, H. A. *Biomaterials* **2015**, *48*, 108–118.

[241] Kotagiri, N.; Li, Z. Y.; Xu, X. X.; Mondal, S.; Nehorai, A.; Achilefu, S. *Bioconjugate Chemistry* **2014**, *25*, 1272–1281.

[242] Gobbo, P.; Mossman, Z.; Nazemi, A.; Niaux, A.; Biesinger, M. C.; Gillies, E. R.; Workentin, M. S. *Journal of Materials Chemistry B* **2014**, *2*, 1764–1769.

[243] Jewett, J. C.; Bertozzi, C. R. *Chemical Society Reviews* **2010**, *39*, 1272–1279.

[244] Chang, P. V.; Prescher, J. A.; Sletten, E. M.; Baskin, J. M.; Miller, I. A.; Agard, N. J.; Lo, A.; Bertozzi, C. R. *Proceedings of the National Academy of Sciences of the United States of America* **2010**, *107*, 1821–1826.

[245] Li, G. Z.; Randev, R. K.; Soeriyadi, A. H.; Rees, G.; Boyer, C.; Tong, Z.; Davis, T. P.; Becer, C. R.; Haddleton, D. M. *Polymer Chemistry* **2010**, *1*, 1196–1204.

[246] Mahajan, N.; Lu, R. B.; Wu, S. T.; Fang, J. Y. *Langmuir* **2005**, *21*, 3132–3135.

[247] Hammond, P. T.; Whitesides, G. M. *Macromolecules* **1995**, *28*, 7569–7571.

[248] Yu, S.; Kim, J. M.; Ahn, H. *Journal of Nanoscience and Nanotechnology* **2011**, *11*, 6034–6038.

[249] Santhanam, V.; Andres, R. P. *Nano Letters* **2004**, *4*, 41–44.

[250] Platnich, C. M.; Banerjee, A.; Kollath, V. O.; Karan, K.; Trudel, S. *Canadian Journal of Chemistry* **2015**, *96*, 190–195.

[251] Xin, Z. Q.; Liu, Y.; Li, X.; Liu, S. L.; Fang, Y.; Deng, Y. Q.; Bao, C.; Li, L. H. *Materials Research Express* **2017**, *4*, 015021.

[252] Rigler, P.; Meier, W. *J. Am. Chem. Soc.* **2006**, *128*, 367–373.

[253] Hesse, M.; Heier, H.; Zeeh, B. *Spektroskopische Methoden in der organischen Chemie*, 6th ed.; Thieme, 1979.

[254] Wu, S. Z.; Zhang, B. T.; Liu, Y.; Suo, X. K.; Li, H. *Biointerphases* **2018**, *13*, 060801.

[255] Rodriguez-Hernandez, J. *Polymers against Microorganisms: On the Race to Efficient Antimicrobial Materials*; Springer International Publishing: Cham, 2017; Chapter 6, pp 125–154.

[256] Zhou, Z.; Calabrese, D. R.; Taylor, W.; Finlay, J. A.; Callow, M. E.; Callow, J. A.; Fischer, D.; Kramer, E. J.; Ober, C. K. *Biofouling* **2014**, *30*, 589–604.

[257] Wang, B. L.; Liu, H. H.; Wang, Z. F.; Shi, S.; Nan, K. H.; Xu, Q. W.; Ye, Z.; Chen, H. *Journal of Materials Chemistry B* **2017**, *5*, 1498–1506.

[258] Hadjesfandiari, N.; Yu, K.; Mei, Y.; Kizhakkedathu, J. N. *Journal of Materials Chemistry B* **2014**, *2*, 4968–4978.

[259] Pasupuleti, M.; Schmidtchen, A.; Malmsten, M. *Critical Reviews in Biotechnology* **2012**, *32*, 143–171.

[260] Singh, S.; Papareddy, P.; Kalle, M.; Schmidtchen, A.; Malmsten, M. *Biochimica Et Biophysica Acta-Biomembranes* **2013**, *1828*, 2709–2719.

[261] Kalle, M.; Papareddy, P.; Kasetty, G.; van der Plas, M. J. A.; Morgelin, M.; Malmsten, M.; Schmidtchen, A. *Plos One 9*, e102577.

[262] Singh, S.; Papareddy, P.; Morgelin, M.; Schmidtchen, A.; Malmsten, M. *Biomacromolecules* **2014**, *15*, 1337–1345.

[263] Pulido, D.; Nogues, M. V.; Boix, E.; Torrent, M. *Journal of Innate Immunity* **2012**, *4*, 327–336.

[264] Wiegand, I.; Hilpert, K.; Hancock, R. E. W. *Nature Protocols* **2008**, *3*, 163–175.

[265] Doniach, S.; Sunjic, M. *Journal of Physics Part C Solid State Physics* **1970**, *3*, 285–291.

[266] Shirley, D. A. *Physical Review B* **1972**, 4709 – 4714.

[267] Hesse, R.; Chasse, T.; Szargan, R. *Fresenius Journal of Analytical Chemistry* **1999**, *365*, 48–54.

[268] Scofield, J. H. *Journal of Electron Spectroscopy and Related Phenomena* **1976**, *8*, 129–137.

[269] Kucharikova, S. et al. *Journal of Antimicrobial Chemotherapy* **2016**, *71*, 936–945.

[270] Schindelin, J. et al. *Nature Methods* **2012**, *9*, 676–682.

[271] Schmidtchen, A.; Ringstad, L.; Kasetty, G.; Mizuno, H.; Rutland, M. W.; Malmsten, M. *Biochimica Et Biophysica Acta-Biomembranes* **2011**, *1808*, 1081–1091.

[272] Chen, R. F.; Knutson, J. R. *Anal. Biochem.* **1988**, *172*, 61–77.

[273] Ulman, A. *Chemical Reviews* **1996**, *96*, 1533–1554.

[274] Behrendt, R.; White, P.; Offer, J. *Journal of Peptide Science* **2016**, *22*, 4–27.

[275] Nyström, L.; Nordström, R.; Bramhill, J.; Saunders, B. R.; Álvarez Asencio, R.; Rutland, M. W.; Malmsten, M. *Biomacromolecules* **2016**, *17*, 669–678.

[276] Luan, Y. F.; Li, D.; Wei, T.; Wang, M. M. M.; Tang, Z. C.; Brash, J. L.; Chen, H. *Anal. Chem.* **2017**, *89*, 4184–4191.

[277] Stevens, J. S.; de Luca, A. C.; Pelendritis, M.; Terenghi, G.; Downes, S.; Schroeder, S. L. M. *Surface and Interface Analysis* **2013**, *45*, 1238–1246.

[278] Wang, K. F.; Nagarajan, R.; Camesano, T. A. *Colloid Surface B* **2014**, *116*, 472–481.

[279] Mechler, S. A. K. B. M. S. F. M. L. L., A.; Praporski *Biophys. J.* **2007**, *93*, 3907–3916.

[280] Sjollema, J.; Zaat, S. A. J.; Fontaine, V.; Ramstedt, M.; Luginbuehl, R.; Thevissen, K.; Li, J. Y.; van der Mei, H. C.; Busscher, H. J. *Acta Biomaterialia* **2018**, *70*, 12–24.

[281] Ilyas, H.; Kim, J.; Lee, D.; Malmsten, M.; Bhunia, A. *Journal of Biological Chemistry* **2019**, *294*, 14615–14633.

[282] Zerweck, J.; Strandberg, E.; Kukharenko, O.; Reichert, J.; Burck, J.; Wadhwani, P.; Ulrich, A. S. *Scientific Reports 7*, 13153.

[283] Beattie, M.; Taylor, J. *Journal of Clinical Nursing* **2011**, *20*, 2098–2108.

[284] Tishkov, V. I.; Savin, S. S.; Yasnaya, A. S. *Acta Naturae* **2010**, *2*, 47–61.

[285] Avinash, V. S.; Pundle, A. V.; Ramasamy, S.; Suresh, C. G. *Critical Reviews in Biotechnology* **2016**, *36*, 303–316.

[286] Li, D.; Zhang, Y.-W.; Cheng, S.; Gao, Q.; Wei, D. *Food Technology and Biotechnology* **2008**, *46*, 461–466.

[287] Duggleby, H. J.; Tolley, S. P.; Hill, C. P.; Dodson, E. J.; Dodson, G.; Moody, P. C. E. *Nature* **1995**, *373*, 264–268.

[288] Pages, J. M.; James, C. E.; Winterhalter, M. *Nature Reviews Microbiology* **2008**, *6*, 893–903.

[289] Danelon, C.; Nestorovich, E. M.; Winterhalter, M.; Ceccarelli, M.; Bezrukov, S. M. *Biophysical Journal* **2006**, *90*, 1617–1627.

[290] Ziervogel, B. K.; Roux, B. *Structure* **2013**, *21*, 76–87.

[291] Bredin, J.; Simonet, V.; Iyer, R.; Delcour, A. H.; Pages, J. M. *Biochemical Journal* **2003**, *376*, 245–252.

[292] Mahendran, K. R.; Kreir, M.; Weingart, H.; Fertig, N.; Winterhalter, M. *Journal of Biomolecular Screening* **2010**, *15*, 302–307.

[293] Chen, J.; Guan, S. M.; Sun, W.; Fu, H. *Neuroscience Bulletin* **2016**, *32*, 265–272.

[294] Matsuzaki, K.; Yoneyama, S.; Miyajima, K. *Biophysical Journal* **1997**, *73*, 831–838.

[295] Burton, M. G.; Huang, Q. M.; Hossain, M. A.; Wade, J. D.; Palombo, E. A.; Gee, M. L.; Clayton, A. H. A. *Langmuir 32*, 6496–6505.

[296] Fennouri, A.; Mayer, S. F.; Schroeder, T. B. H.; Mayer, M. *Biochimica Et Biophysica Acta-Biomembranes* **2017**, *1859*, 2051–2057.

[297] Bundgaard, H.; Larsen, C. *Journal of Pharmaceutical and Biomedical Analysis* **1983**, *1*, 29 – 37.

[298] Vilt, M. E.; Ho, W. S. W. *Industrial & Engineering Chemistry Research* **2010**, *49*, 12022–12030.

Acknowledgments

I big thank you to everyone who has been directly or indirectly involved in the research I conducted within the scope of this thesis.

First of all I want to kindly thank my supervisor Prof. Dr. Cornelia G. Palivan for giving me the opportunity to perform such an interesting PhD research in her group. Next, I want to thank Prof. Dr. Wolfgang Meier to be my PhD co-supervisor. I am also honored, that Prof. Dr. Marcus Textor accepted to be the coreferee of my PhD thesis.

Furthermore, I want to thank all former and present group members for the nice work atmosphere, helpful discussions, and encouragements. Many thanks go to Dr. Samuel Lörcher for synthesizing the block copolymers, introducing me to TEM measurements and many fruitful discussions. Many thanks also go to Andrea Belluati for expressing OmpF. I want to thank Dr. Gesine Gunkel-Grabole for her guidance, support, proofreading manuscripts, and many helpful discussions. I am very grateful to Dr. Cora-Ann Schoenenberger for proofreading my manuscripts, helpful discussions, support, and guidance. A big thank you also goes to Dimitri Hürlimann who worked with me in the beginning as a student doing one of his block courses on my project and then doing his master thesis studying the antimicrobial peptide decorated micelles. I wish him all the best for his own PhD research now. Susanne Erpel and Markus Dürrenberger from the Nano Imaging lab, University of Basel are acknowledged for SEM imaging and help with TEM. Dr. Laurent Marot from the department of physics, University of Basel is acknowledged for XPS experiments. For administrative support I thank Maya Greuter, Daniela Tischhauser, Beatrice Erismann, Markus Hauri, and Dr. Michael Devereux. I want to thank the PCC team, for the nice time and perfect organization of many social and research activities.

I am grateful to Prof. Dr. Martin Malmsten for the guidance and organization during my scientific exchange in Uppsala, Sweden and the introduction to antimicrobial peptides. Furthermore, I thank all his group members for the nice atmosphere I encountered as a guest in their laboratories.

I am very grateful to Dr. Jason Duskey for his support, critical discussions, proofreading many manuscripts and good time throughout my whole research career. A big thank you goes to Dr. Sagana Thamboo, for the nice and supportive time during our whole University studies together, from Bachelor to PhD in this group. I would like to thank all my friends and family for their support and encouragement.

Finally I want to thank my sisters Elvira and Aurora and my parents Irene and Renzo for their never-ending support and love.